Journal Pre-proofs

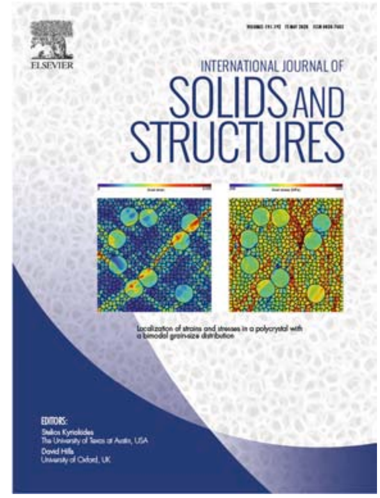

Micromechanical modelling of the longitudinal compressive and tensile failure of unidirectional composites: The effect of fibre misalignment introduced via a stochastic process

L.F. Varandas, G. Catalanotti, A.R. Melro, R.P. Tavares, B.G. Falzon

PII: S0020-7683(20)30299-7
DOI: https://doi.org/10.1016/j.ijsolstr.2020.07.022
Reference: SAS 10807

To appear in: *International Journal of Solids and Structures*

Received Date: 30 April 2020
Revised Date: 16 July 2020
Accepted Date: 31 July 2020

Please cite this article as: L.F. Varandas, G. Catalanotti, A.R. Melro, R.P. Tavares, B.G. Falzon, Micromechanical modelling of the longitudinal compressive and tensile failure of unidirectional composites: The effect of fibre misalignment introduced via a stochastic process, *International Journal of Solids and Structures* (2020), doi: https://doi.org/10.1016/j.ijsolstr.2020.07.022

Micromechanical modelling of the longitudinal compressive and tensile failure of unidirectional composites: The effect of fibre misalignment introduced via a stochastic process

L.F. Varandas[a], G. Catalanotti[a,*], A.R. Melro[b], R.P. Tavares[c,d], B.G. Falzon[a]

[a] Advanced Composites Research Group (ACRG), School of Mechanical and Aerospace Engineering, Queen's University Belfast, Belfast BT9 5AH, UK
[b] Bristol Composites Institute (ACCIS), University of Bristol, Bristol BS8 1TR, UK
[c] DEMec, Faculdade de Engenharia, Universidade do Porto, Rua Dr. Roberto Frias, 4200-465, Porto, Portugal
[d] INEGI, Rua Dr. Roberto Frias, 400, 4200-465 Porto, Portugal

Abstract

Initial fibre misalignment is recognised to be one of the precursors leading to longitudinal compressive failure in fibre-reinforced composites. Thus, to properly model their mechanical behaviour, an accurate spatial representation of the fibrous reinforcements must be assured. This work presents a three-dimensional micromechanical framework that is capable of analysing in detail the longitudinal tensile and compressive failure mechanisms which are inherent in unidirectional composites. This is achieved through the incorporation of initial fibre waviness via a combination of a stochastic process and an optimisation procedure. A robust micro-scale framework is developed by assigning, to both constituents and their interface, proper thermodynamically consistent damage models. Several microstructures having different degrees of misalignment are modelled and a clear trend is observed for the longitudinal compressive load case, i.e. by increasing initial fibre misalignment, the overall performance of the material decreases. In contrast, the models subjected to longitudinal tension exhibit a similar overall response, despite the misalignment. However, local mechanisms seem to change with the degree of friction and fibre misalignment, but these smaller-scale mechanisms do not play a decisive role on the overall longitudinal tensile performance of the material.

Keywords: Composite materials, Fibre misalignment, Fracture, Micromechanics, Stochastic

1. Introduction

As a direct consequence of increasing computational power, in the last decade, computational micromechanics has emerged as an accurate and reliable numerical tool to evaluate both linear and non-linear geometrical and material behaviour of heterogenous materials. Unlike analytical/semi-analytical methods, the several complex dissipative phenomena, including local plastic deformation and degradation of the matrix constituent, fibre-matrix interface debonding, and fibre fracture, are accounted for and their interaction can be evaluated.

Compressive failure of composite materials caused by fibre kinking is classified as a complex, multi-staged phenomenon, due to the interacting mechanisms and instabilities present at peak load, which span over several length-scales of the material (Argon, 1972, Budiansky, 1983, Budiansky, Fleck, 1993, 1994, Moran et al., 1995, Jumahat et al., 2010, Costa et al., 2020). There is compelling evidence that this mode of failure is mostly driven by not only the initial misalignment of the fibres, but also by the shear yield strength of the matrix (Moran et al., 1995, Bažant et al., 1999, Vogler et al., 2001, Gutkin et al., 2010b, Pinho et al., 2012). The material is loaded elastically until the first appearance of non-linearity, which is due to the initial rotation of the fibres, permitted by the plastic response of the matrix. This is also known as "incipient kinking" (Moran et al., 1995). Due to this rotation and to the formation of microcracks in the resin, the peak load (instability) is reached, forming an initial kink-band. The progressive shearing/bending stresses in the material causes its continuous degradation, until this fibre rotation is halted, through a process referred as fibre lock-up, which eventually leads to the steady-state broadening of the kink-band, causing a constant stress plateau under compression, referred as the residual compressive strength of the material (Moran et al., 1995, Zobeiry et al., 2015, Dalli et al., 2020). Kink-bands are characterised by an angle, β_{kb}, with respect to the through-thickness direction (normal to the load), a certain width, w_{kb}, having the fibres rotated from an angle, φ_{kb}, to the global longitudinal direction. Figure 1 shows a micrograph of a formed kink-band in an UD cross-ply laminate, as well as a schematic representation of a longitudinal compressive stress-strain curve, highlighting the main load level stages.

[Figure 1 about here.]

Several computational micromechanical models have been reported, in an attempt to model longitudinal compressive failure in UD composite materials by fibre kinking. Initial insights were provided using two-dimensional (2D) models, namely on the types of failure mechanisms associated with compressive failure (Gutkin et al., 2010a), the interaction between fibre kinking and fibre-matrix interface debonding (Prabhakar, Waas, 2013), and on the estimation of the kink-band angle and compressive strength of the material (Kyriakides et al., 1995, Vogler et al., 2001). The limitations of 2D models were addressed by Hsu et al. (1998), where a bigger degree of discrepancy between 2D and three-dimensional (3D) models was observed in the post-peak regime. Fortunately, modern computational resources have enabled the generation of 3D high-fidelity numerical models. Yerramalli, Waas (2004) conducted 3D Finite Element (FE) analyses to show the importance of fibre bending stiffness on the overall compressive strength of the material, as well as the presence of a complex triaxial stress state in the matrix region. Later, Bai et al. (2015), incorporating a more robust elasto-plastic damage model for the resin (Melro et al., 2013a), subjected different Representative Volume Elements (RVEs) to several loading conditions, i.e. transverse on- and off-axis compression, and pure longitudinal compression. They were able to obtain some preliminary results concerning kink-band widths and fibre rotation angles, concluding that the interplay between the shear stresses, presented in the matrix material, and microbuckling, caused by the initial, idealised fibre misalignment, provides a sound explanation to the fibre kinking failure mode. Bishara et al. (2017) conducted simpler micromechanical simulations, considering a single array of fibres, in order to assess the influence of the artificial imperfection type on the resulting kinking mechanism, the effective determination of the kink-band angle, and the effect of different fibre strengths on the kink-band angle. Recent studies using a sinusoidal swept single fibre model, subjected to Periodic Boundary Conditions (PBCs), were undertaken (Naya et al., 2017, Herráez et al., 2018, 2020) to give more insight into the effect of the initial fibre misalignment angle on the kink-band width and fibre rotation angles, by comparing the results with well known analytical models. As remarked by Hill (1963), an RVE is a medium which characterises the microstructure of the material, being statistically representative of the mixture of constituents. It has a dimension that contains a sufficient number of inclusions/reinforcements, making a single fibre model non-representative of the actual material. Moreover, the application of such PBCs force the kink-band angle to be zero, i.e. $\beta_{kb} = 0$. Finally, the use of the maximum homogenised stress, obtained by using First Order Homogenisation Techniques (FOHT), may not be a proper way to measure the actual strength of the material, since, as strain localisation occurs, the separation of scales (Hashin, 1983) is intrinsically violated, making the solution dependent on both BCs applied and size of the considered medium. For a concise review on the analytical, semi-analytical, and numerical methodologies which treat longitudinal compressive failure in fibre-reinforced composites, addressing both phenomenology and failure mechanisms involved, the reader is referred to Daum et al. (2019).

Modelling fibre-dominated damage, in UD composites, is a complex task due to the acting damage mechanisms which arise when submitted to a longitudinal tensile loading scenario. There are several important factors when modelling the longitudinal tensile behaviour of a composite, namely: i) capture the formation of fibre break clusters, which later leads to the unstable final failure of the material (Scott et al., 2011, 2012, Thionnet et al., 2014); ii) capture the stochastic nature of the tensile strength of carbon fibres (Lamon, 2007, Tanaka et al., 2014, Torres et al., 2017); iii) capture the complete ineffective and debond length of a broken fibre; and iv) treat fibre fracture as a dynamic event, where the internal strain energy released by the reinforcements is converted into kinetic energy (Swolfs et al., 2015a, Tavares et al., 2019b). Figure 2 shows a computed tomography (CT) image of a cross-ply laminate, which failed under longitudinal tension, highlighting the pulled-out 0° fibres and the corresponding perpendicular fracture plane (Laffan et al., 2010), and a synchrotron radiation computed tomography (SRCT) image of disperse and co-planar clusters of broken fibres (Swolfs et al., 2015a).

[Figure 2 about here.]

There are several models which are available in literature that are capable of estimating the longitudinal tensile strength of UD carbon fibre-reinforced composite materials, hybridised or not, being able to tackle most (if not all) of the aforementioned features governing longitudinal tensile failure (Swolfs et al., 2015c,b, 2016, Tavares et al., 2016, 2017, St-Pierre et al., 2017, Guerrero et al., 2018, Tavares et al., 2019b). These often rely on simpler micromechanical models, where fibre fracture is taken into account using maximum stress criteria. In contrast, the work of Tavares et al. (2016) reports the usage and implementation of thermodynamically consistent damage models, providing enough detail to capture the micro-scale failure mechanisms which govern longitudinal tensile failure.

Most of the aforementioned micromechanical models make reference to an implicitly assumed, constant in space, initial fibre misalignment, making such predictions unsuitable for real case scenarios, since to empirically quantify fibre misalignment, a statistically representative parameter is needed. Variable, spatially distributed fibre waviness, has long been recognised as an important consideration, and investigations into the stochastic properties of its magnitude and distribution have been reported (Hillig, 1994, Clarke et al., 1995, Creighton et al., 2001, Requena et al., 2009, Sutcliffe et al., 2012, Pain, Drinkwater, 2013, Mizukami et al., 2016, Wilhelmsson, Asp, 2018). Recently, Sebaey et al. (2019) developed an integrated approach to statistically represent fibre misalignment at the scale of the constituents, where the deviations in fibre angles and corresponding footprints are first determined using CT scans, and then the data is statistically fitted following a von Mises distribution, characterised by the corresponding concentration parameter. A post-study conducted by Catalanotti, Sebaey (2019) involved the proposal of a semi-stochastic algorithm where initial fibre misalignment is taken into account by combining the stochastic process and an optimisation procedure.

Here, a 3D FE micromechanical framework is built to analyse in detail, the longitudinal failure of composite materials. To describe the non-linear behaviour of the constituents and their interface, appropriate constitutive material models are implemented along with an algorithm for the generation of high-fidelity RVEs, accounting for a stochastic-based fibre misalignment. To the authors' knowledge, this is the first time that a numerical micromechanical framework is built together, to investigate the effect of a stochastic-based initial fibre waviness on the longitudinal failure of unidirectional carbon fibre-reinforced composite materials. Additional analyses are undertaken to investigate the effect of considering frictional cohesive surfaces on the damage tolerance of the composite.

2. Computational framework

The developed 3D FE micromechanical framework is composed of detailed micromechanical representations of the material, henceforth described as RVEs, having different degrees of fibre misalignment and the same fibre volume fraction, ω_f. For brevity, only pertinent aspects of the RVE generation and the constitutive material models used, are presented, where several important considerations are discussed.

2.1. Generation of the RVEs

The generation of the RVEs involves the measurement of the angle between the projection of the tangent vector of the fibres and a given direction (Catalanotti, Sebaey, 2019). Figure 3 shows the three spatial descriptors, which the algorithm makes use of, that characterise fibre misalignment, where x, y, and z represent the longitudinal, transverse, and through-thickness directions of a typical UD lamina, respectively, and $\vec{i}$, $\vec{j}$, and $\vec{k}$ the unit vectors in each corresponding direction.

[Figure 3 about here.]

The three spatial descriptors, shown in Figure 3, are the three misalignment angles, which are defined as: ϕ_{yx}, the angle between $\vec{i}$ and the projection of the tangent vector to the fibre, $\vec{\nu}$, onto the O_{xz} plane; ϕ_{zx}, the angle between $\vec{i}$ and the projection of the tangent vector to the fibre, $\vec{\nu}$, onto the O_{xy} plane; and α_{xy}, the angle between $\vec{j}$ and the the projection of the tangent vector to the fibre, $\vec{\nu}$, onto the O_{yz} plane (Catalanotti, Sebaey, 2019). Both in-plane and out-of-plane misalignment angles, ϕ_{yx} and ϕ_{zx}, respectively, are of importance when conducting RVE-based numerical simulations, and may be experimentally characterised using appropriate experimental techniques (Sutcliffe et al., 2012, Sebaey et al., 2019). However, there is no relevance on characterising the remaining misalignment angle, α_{xy}, since, in principle, it does not have any practical importance when submitting the RVEs to the stress states mentioned in this work.

For introducing the waviness of the fibres via a stochastic process, the fibres are modelled as Bézier curves, whose initial control points are determined by using a 2D fibre distribution algorithm (Catalanotti, 2016). These control points can then be moved in a random fashion, for a desired number of times, in a plane perpendicular to $\vec{i}$, creating the 3D geometrical variability, i.e. fibre waviness. Periodicity of the virtual microstructure is also achieved by computing the proper distance between the control points of different fibres and assuring continuity between the first and last control point of the same fibre, when translated in the longitudinal direction by the length of the RVE (Catalanotti, Sebaey, 2019). The radial coordinates are chosen in order to ensure that the distribution of the misalignment angles match the empirical/theoretical ones (Sebaey et al., 2019). It was assumed the distribution follows the general von Mises distribution, whose probability density function (pdf) reads:

$$\mathrm{g}(\phi, \mu, \kappa) = \frac{1}{2\pi I_0(\kappa)} \mathrm{e}^{\kappa \cos(\phi) - \mu}, \tag{1}$$

where ϕ is equal either to the in-plane or out-of-plane misalignment angle, μ is the mean direction, κ is the concentration parameter, and I_0 is the modified Bessel function of the first kind and order 0. Since the mean direction represents the longitudinal (x-direction) direction of the composite, μ is assumed to be equal to 0, and therefore the concentration parameter, κ, is the only variable which characterises the distribution. By minimising the standard errors (likelihood and probability), it is possible to achieve a remarkable match between the experimental/theoretical and numerical distributions. Figure 4 shows an example of the pdf of theoretical and numerical distributions, the Q-Q plot, and the associated front and isometric views of a generated RVE with $\kappa = 2000$.

[Figure 4 about here.]

For modelling perfectly aligned fibres, κ is equal to ∞, and for modelling very wavy fibres, κ takes a small value, e.g. $\kappa = 500$. For a complete description of the algorithm used to generate 3D RVEs incorporating fibre waviness, the reader is referred to Catalanotti, Sebaey (2019).

2.2. Constitutive material models

2.2.1. Carbon fibres

The carbon fibres are modelled as transversely isotropic and considered to behave linear-elastically up to failure. Degradation of the stiffnesses of the material is defined by implementing a thermodynamically consistent isotropic damage model, which is only activated by the longitudinal stress component. The damage activation function is given as:

$$F_f^d = \phi_f^d - r_f = \frac{\tilde{\sigma}_{11}}{X_f^t} - r_f, \tag{2}$$

where ϕ_f^d is the loading function, $\tilde{\sigma}_{11}$ is the undamaged longitudinal applied stress, X_f^t is the longitudinal tensile strength of the fibre, and r_f is an internal variable related to the damage evolution law of the fibre, d_f. As discussed by several authors (Swolfs et al., 2015c,b, Tavares et al., 2016, Swolfs et al., 2016, Tavares et al., 2017), the tensile strength of the carbon fibres has an intrinsic stochastic nature, mostly due to the flaws which are present on the surface of the fibres (Lamon, 2007, Tanaka et al., 2014, Torres et al., 2017), which needs to be taken into account. Here, these are accounted for through the Weibull distribution (Weibull, 1951):

$$P(\sigma) = 1 - \exp\left[-\left(\frac{L}{L_0}\right)\left(\frac{\sigma}{\sigma_0}\right)^{m_0}\right], \tag{3}$$

where P represents the failure probability at the applied stress σ, σ_0 and m_0 are the Weibull strength and parameter, respectively, and L_0 and L are the reference and gauge length, respectively. Modifying equation (3) and generating a random scalar in the interval $]0,1[$, $\mathscr{X}$, that represents the failure probability, the tensile strength can be estimated following:

$$X_f^t = \sigma_0 \left[-\frac{L_0}{L} \ln(1-\mathscr{X})\right]^{1/m_0}. \tag{4}$$

The Weibull distribution is probably the most used statistical distribution for fibre strength. However, it has been shown that it is not the best suited for carbon and glass fibres (Gulino, Phoenix, 1991, Beyerlein, Phoenix, 1996, Curtin, 2000), leading to an overprediction in both tensile strength and failure strain (Tavares et al., 2017). The correct definition of the proper fibre tensile strength distribution is out of the scope of the current work, thus the Weibull distribution is used due to its simplicity in implementation.

To avoid damage localisation and to control the energy dissipated in the fracture process, Bažant and Oh's *crack band model* (Bažant, Oh, 1983) is implemented to regularise the computed dissipated energy:

$$\Psi_f = \int_1^\infty \frac{\partial \mathscr{G}_f}{\partial d_f}\frac{\partial d_f}{\partial r_f} \mathrm{d}r_f = \frac{\mathcal{G}_{Ic}^f}{l_f^e}, \tag{5}$$

where $\mathscr{G}_f$ is the complementary free energy density of the fibrous material, $\mathcal{G}_{Ic}^f$ is the mode I fracture toughness of the fibres, and l_f^e represents the characteristic element length.

The damage evolution law for the fibres is given by:

$$d_f = 1 - \frac{e^{A_f(1-r_f)}}{r_f}, \tag{6}$$

where A_f is a mesh regularisation parameter which conveys the numerical model with mesh size independency (Bažant, Oh, 1983) and must be computed for each finite element by solving equation (5).

The mechanical properties of the AS4 fibres considered here are shown in Table 1 and were taken from Soden et al. (1998), Bai et al. (2015), Herráez et al. (2016), Tavares et al. (2016).

[Table 1 about here.]

For more details on the damage model, the reader is referred to Tavares et al. (2016).

2.2.2. Epoxy matrix

Previous studies (Ghorbel, 2008) have shown that both the Drucker-Prager and Mohr-Coulomb constitutive material models are not able to properly model the representative behaviour of an epoxy resin, namely under the presence of triaxial stress states. A more representative elasto-plastic material model, proposed by Melro et al. (2013a), is used here to simulate the behaviour of the matrix constituent.

The model assumes that the matrix behaves in a linear-elastic fashion until the following paraboloidal yield criterion, originally proposed by Tschoegl (1971), is met:

$$\Phi(\boldsymbol{\sigma}, \varepsilon_e^p) = 6J_2 + 2(\sigma_{Y_c}^m - \sigma_{Y_t}^m)I_1 - 2\sigma_{Y_c}^m \sigma_{Y_t}^m, \tag{7}$$

where $\sigma_{Y_t}^m$ and $\sigma_{Y_c}^m$ are the absolute values of the tensile and compressive yield strengths, $I_1 = \mathrm{tr}(\boldsymbol{\sigma})$ is the first invariant of the stress tensor and $J_2 = \frac{1}{2}\boldsymbol{s} : \boldsymbol{s}$ is the second deviatoric stress tensor ($\boldsymbol{s}$) invariant. In order to correctly define the plastic deformation under the presence of a hydrostatic pressure, a non-associative flow rule is defined. Both tensile and compressive yield strengths depend on the equivalent plastic strain, ε_e^p:

$$\varepsilon_e^p = \sqrt{\frac{1}{1 + 2{\nu_m^p}^2} \varepsilon^p : \varepsilon^p}, \tag{8}$$

where ν_m^p is the plastic Poisson's ratio of the matrix.

The yield surface presented in equation (7) depends only on the tensile ($\sigma_{Y_t}^m$) and compressive ($\sigma_{Y_c}^m$) yield strengths which are both affected by hardening:

$$\sigma_{Y_t}^m = \sigma_{Y_t}^m(\varepsilon_e^p), \qquad \sigma_{Y_c}^m = \sigma_{Y_c}^m(\varepsilon_e^p). \tag{9}$$

Figure 5 shows the hardening curves used in the plasticity model in both tension and compression.

[Figure 5 about here.]

Damage is defined by using a model developed within the framework of thermodynamically admissible processes. Initiation of damage is computed with the following failure criterion (Melro et al., 2013a):

$$F_m^d = \phi_m^d - r_m = \frac{3\tilde{J}_2}{X_m^c X_m^t} + \frac{\tilde{I}_1(X_m^c - X_m^t)}{X_m^c X_m^t} - r_m, \tag{10}$$

where ϕ_m^d is the loading function, X_m^c and X_m^t represent the compressive and tensile strengths of the material, respectively, and r_m is an internal variable related to the matrix damage variable. Both invariants ($\tilde{J}_2$ and $\tilde{I}_1$) are determined using the effective stress tensor, i.e. the stress tensor calculated using the undamaged stiffness tensor. The damage variable is given by:

$$d_m = 1 - \frac{e^{A_m(3-\sqrt{7+2r_m^2})}}{\sqrt{7+2r_m^2} - 2}, \tag{11}$$

where A_m is a parameter that must be computed for each element of the finite element mesh of the matrix material. To avoid mesh size dependency problems, Bažant and Oh's *crack band model* (Bažant, Oh, 1983) was also implemented, making use of the mode I fracture toughness of the epoxy, $\mathcal{G}_{Ic}^m$ and corresponding characteristic element length, l_m^e, to regularise the computed dissipated energy (Bažant, Oh, 1983):

$$\Psi_m = \int_1^\infty \frac{\partial \mathscr{G}_m}{\partial d_m} \frac{\partial d_m}{\partial r_m} \mathrm{d}r_m = \frac{\mathcal{G}_{Ic}^m}{l_m^e}, \tag{12}$$

where $\mathscr{G}_m$ is the complementary free energy density of the matrix material.

Table 2 shows the mechanical properties used to model the epoxy. For more information regarding the constitutive material model, the reader is referred to Melro et al. (2013a).

[Table 2 about here.]

This material constitutive model has exhibited promising results when modelling the behaviour of epoxy resins under a variety of loading conditions (Melro et al., 2013b, Arteiro et al., 2014, 2015, Tavares et al., 2016, Varandas et al., 2017, 2019, Sun et al., 2019b, Arteiro et al., 2019, Chen et al., 2019, Meer van der et al., 2019, Dalli et al., 2019, Varandas et al., 2020a,b, Dalli et al., 2020).

2.2.3. Fibre-matrix interface

Due to the intricate mesh required for these RVEs, the interfaces between fibres and matrix were modelled using cohesive surfaces, rather than cohesive elements, as it does not require mesh compatibility between the two constituents. A Mohr-Coulomb friction condition has also been considered for post-failure of the cohesive bond between the two constituents. Once the cohesive stiffness starts degrading, friction starts contributing to the shear stresses. This feature will capture the pull-out resistance between fibre and matrix caused mostly by the rough failure surface on the fibre, after interfacial failure, and it is governed by the friction coefficient, μ_τ.

Initiation of fibre-matrix interface damage is predicted using a stress-based quadratic failure criterion (Lin Ye, 1988):

$$\phi_{int}^{d} = \left(\frac{\langle \tau_3 \rangle}{\tau_3^0}\right)^2 + \left(\frac{\tau_2}{\tau_2^0}\right)^2 + \left(\frac{\tau_1}{\tau_1^0}\right)^2, \tag{13}$$

where τ_1, τ_2, and τ_3 represent the components of traction and τ_1^0, τ_2^0, and τ_3^0 are the corresponding interface strengths. A bi-linear traction-separation behaviour is assumed, and the fibre-matrix interface damage variable is computed as (Aba, 2018):

$$d_{int} = \frac{\delta_{int}^{f}(\delta_{int}^{\max} - \delta_{int}^{0})}{\delta_{int}^{\max}(\delta_{int}^{f} - \delta_{int}^{0})}, \tag{14}$$

where, $\delta_{int}^{f} = 2\mathcal{G}_c^{int}/\tau_{\text{eff}}^0$, with $\mathcal{G}_c^{int}$ as the mixed-mode fracture toughness (Benzeggagh, Kenane, 1996) and τ_{eff}^0 as the effective traction at damage initiation. $\delta_{int}^{\max}$ refers to the maximum value of the effective displacement attained during loading history and δ_{int}^0 is the displacement at damage initiation. Table 3 shows the properties used to model the interfaces.

[Table 3 about here.]

2.3. Finite element modelling

Several RVEs having different concentration parameters, κ, are considered (see equation (1)). As remarked by Hill (1963), an important aspect in RVE-based modelling, is the size of the RVE and boundary conditions (BCs) imposed. The applied BCs should affect the overall mechanical performance of the material, namely during softening, existing an interplay between the BCs and size of the RVE (Triantafyllidis, Bardenhagen, 1996, Gitman et al., 2007, Galli et al., 2008). Since Periodic Boundary Conditions (PBCs) yield an enormous computational cost, as well as, in longitudinal compression, they constrain the kink-band angle *a priori* (Gutkin et al., 2010a), standard BCs are used, where direct constraints are applied to the boundaries of the RVEs. Moreover, by considering a sufficiently large FE model, edge and face effects can be neglected (Kanit et al., 2003, Stroeven et al., 2004, Gitman et al., 2006, Sun et al., 2019b). With reference to Figure 6, the following BCs are applied for each loading condition (Hsu et al., 1998, Vogler et al., 2001, Tavares et al., 2016, Bishara et al., 2017):

- Longitudinal compression - The longitudinal (x-direction) and through-thickness (z-direction) axial displacements of face 1 are fixed. *Tie Constraints* are applied between Face 3 and Face 4. A longitudinal (x-direction) compressive velocity-type BC is applied to face 2. Faces 5 and 6 are free to deform.
- Longitudinal tension - The longitudinal axial (x-direction) displacements are fixed on Face 1 and a longitudinal (x-direction) tensile velocity-type BC is applied to Face 2. All other faces are free to deform to account for Poisson's contraction.

The dimension of the RVEs in the longitudinal direction (x-direction) is denoted by L_x, and the in-plane dimensions (y- and z-directions) by H (see Figure 3).

[Figure 6 about here.]

The micromechanical simulations were conducted using the FE solver Abaqus®/Explicit (Aba, 2018). Damaged elements having $d_f > 0.9999 \vee d_m > 0.9999$ (see equations (6) and (11)) were removed throughout the numerical simulations to prevent excessive element distortion. The models ran on one node (20 CPUs @ 3.4 GHz of Intel® Haswell®) having 512 GB of RAM. The *Variable Mass Scaling* capability of Abaqus®/Explicit (Aba, 2018) was used in order to reduce computational cost, by scaling all masses of the elements, to ensure that they all have the same time increment. With that being said, due to the peak load instability and to its kinetic nature, load stages beyond peak load, such as kink-band broadening, could not be captured using the present framework.

Due to its complex geometry, the epoxy matrix material is modelled using C3D4, three-dimensional linear tetrahedrons. The fibres are modelled using C3D8R, reduced integration, linear hexahedrons, combined with C3D6R, reduced integration, linear triangular prisms. The orientation of each element is computed by: (i) obtaining the coordinates of the respective centroid of the ith element, $\boldsymbol{C}_i=\{x_i, y_i, z_i\}^T$; (ii) finding the nearest point of the middle line of the associated fibre, i.e. of the associated Bézier curve, to the centroid $\boldsymbol{C}_i$, with coordinates $\boldsymbol{C}_f=\{x_f, y_f, z_f\}^T$; and (iii) calculating the unit vector which is tangent to the curve in $\boldsymbol{C}_f$, i.e. $\hat{\boldsymbol{f}}$, and assign it to the orientation of the ith element. Figure 7 shows the longitudinal direction (1-direction) of each element, in a highly misaligned fibre.

[Figure 7 about here.]

3. Numerical results

3.1. Longitudinal compression

This section aims to evaluate the longitudinal compressive failure through fibre kinking. Different RVEs, having random microstructures with several degrees of misalignment were generated following equation (1), with $\kappa = 1500$, $\kappa = 2000$, $\kappa = 3000$, $\kappa = 4000$, $\kappa = 6000$, $\kappa = 8000$, and $\kappa = \infty$. Figure 8 shows the pdf distribution of the misalignment angles for each von Mises concentration parameter considered in this section. Certain outputs related to compressive failure are analysed in detail, making several quantitative and qualitative parallelisms with experimental observations. Moreover, the effect of fibre-matrix interfacial friction is also analysed. It must be noted that it is not feasible to compare these numerical results with analytical/semi-analytical models which estimate the compressive strength of the material, since most of these assume a constant in space initial fibre misalignment angle.

[Figure 8 about here.]

The following two sections present preliminary results assessing the influence of the RVE size and mesh density on the peak stress of the material, as well as global and local features exhibited on a material loaded in longitudinal compression.

3.1.1. Effect of RVE size

Several analyses were conducted to evaluate the influence of the size of the RVE and its mesh size on the overall mechanical performance of the material. Firstly, RVEs with a refined mesh and different dimensions were virtually tested. By considering a constant aspect ratio of the RVE (ratio between the length and in-plane dimensions of the RVE, $A_r = L_x/H$), i.e. $A_r = 4$, the in-plane dimensions considered were 5, 10, 15, 20, 25, and 30 times the radius of a single fibre. Figure 9 and Table 4 show the normalised numerical predictions, with respect to the peak stress associated with the largest RVE. Only one simulation was conducted per size, for $\kappa = 4000$.

[Figure 9 about here.]

[Table 4 about here.]

The results show that when increasing the size of the RVE, the peak load increases as well. Since the smallest RVEs could not accommodate the formation of a kink-band, the material failed prematurely mainly due to interfacial debonding. The results are considered geometrical independent for RVEs with $H \geqslant 25R_f$, where the peak load represented $\approx 99\%$ of the RVE having the largest dimensions. From the concluded above, in-plane dimensions and total length of the RVE of approximately $H = 75$ μm and $L_x = 300$ μm, respectively, are chosen for the forthcoming numerical simulations.

3.1.2. Influence of mesh density

To ensure mesh independent results, FE meshes of different densities were considered, for an FE model with $\kappa = 4000$, and pertinent results are presented in Figure 10 and Table 5.

[Figure 10 about here.]

[Table 5 about here.]

Mesh independence was achieved with models containing over 7 million elements. Therefore, a mesh density with an average value of $R_f/5$ was considered for the forthcoming simulations.

3.1.3. Global mechanical response

Figure 11 shows the numerical results associated with an RVE with $\kappa = 3000$, where a representative stress-strain curve is shown (see Figure 11a) and corresponding contour plots of the equivalent plastic strain of the epoxy matrix (see Figure 11b), associated with three different stages of the non-linear process: (A) initiation of plasticity; (B) just before peak load instability, where the kink-band is almost formed; and (C1) and (C2) complete formation of the kink-band and initiation of the dynamic process.

[Figure 11 about here.]

To assess the effect of the initial fibre misalignment on the longitudinal mechanical performance of the material, it is presented in Figure 12a the representative stress-strain curves for different concentration parameters, κ, all normalised with respect to the results associated with $\kappa = \infty$. Moreover, in Figure 12b and Table 6, the results associated with the effect of the initial fibre misalignment on both overall longitudinal compressive Young's modulus and strength of the material are shown.

[Figure 12 about here.]

[Table 6 about here.]

The normalised stress vs. applied strain curves are presented in Figure 12a (where σ_{11} and ε_{11} represent the longitudinal stress and strain, respectively, and $\sigma_{11_\infty}^{cu}$ represents the compressive peak stress associated with the RVE with $\kappa = \infty$), which shows that both compressive Young's modulus, E_{11}^c, and peak stress, σ_{11}^{cu}, depend on the initial fibre misalignment angle distribution, quantified by κ. As κ increases (less misalignment), both mechanical properties increase. The RVEs having the highest misalignment ($\kappa = 1500$) yielded a peak stress of $\approx 32\%$ that of the idealised RVE having perfectly aligned fibres ($\kappa = \infty$). The decrease in peak stress is explained by the higher initial micro-buckling introduced in several regions of the fibres along the length of the RVEs, causing an earlier degradation of the epoxy matrix and fibre-matrix interface, thus promoting an earlier kinking of the reinforcement. Moreover, for this material system, the quantitative results show that the variation in peak stress with the distribution of the misalignment angles fits better with a rational type of fit ($\sigma_{11}^{cu}(\kappa^{-1}) = (p_1\kappa^{-1} + p_2)/(\kappa^{-1} + q_1)$, where $p_1 = 667.30$, $p_2 = 1.00$ and $q_1 = 1.95 \times 10^{-4}$), and the corresponding coefficient of determination is approximately $R^2_{\text{rat}} = 0.991$. The compressive Young's modulus can be assumed to vary in a linear fashion ($E_{11}^c(\kappa^{-1}) = n_1\kappa^{-1} + n_2$, where $n_1 = -2.05 \times 10^4$ and $n_2 = 125.40$), where the corresponding coefficient of determination is approximately $R^2_{\text{lin}} = 0.994$, as shown in Figure 12b.

Comparing the results with the experimental values of the longitudinal compressive strength of several composite material systems, having similar fibre volume fractions, such as AS4/8552 ($X^c \approx 1530$ MPa), IM7/8552 ($X^c \approx 1689$ MPa), and IM10/8552 ($X^c \approx 1793$ MPa) (Hexcel, 2016a) or IMA/M21 ($X^c \approx 1500$ MPa), AS7/M21 ($X^c \approx 1560$ MPa), and IM7/M21 ($X^c \approx 1790$ MPa) (Hexcel, 2016b), it is evident that only the RVEs having fibres with a more realistic initial fibre misalignment angle distribution (Sebaey et al. (2019), found for an IM7/8552 and an IM7/PEEK UD material systems, a von Mises concentration parameter of $\kappa = 1582.91$ and $\kappa = 2069.72$, respectively) yielded reasonable longitudinal compressive strengths. In contrast, as shown in Figure 13, the idealised RVE incorporating perfectly aligned fibres ($\kappa = \infty$), did not form a kink-band, due to the unrealistic spatial representation of the fibres, but a sort of crushing scenario, in which the RVE failed at higher applied strains in a region near to the boundaries of the RVE, overpredicting the mechanical performance of the material.

[Figure 13 about here.]

By considering the non-uniform variation of the fibre waviness along the RVE, when this waviness was relatively high, a local failure in the highest misaligned region was observed prior to ultimate failure. Figure 14 shows the contour plots of the equivalent plastic strain (equation (8)), at different stages of the damage process, associated with an RVE with $\kappa = 1500$. The first appearance of non-linearity was in a region where the fibres were highly misaligned, leading to local damage propagation, and for a higher applied strain, catastrophic failure of the material.

[Figure 14 about here.]

Interestingly, some RVEs exhibited a wedge-shaped kink-band, as shown in Figure 15. This was also seen experimentally (Sun et al., 2019a, Wang et al., 2019), where, during compressive loading, localised areas of the material having smaller degrees of misalignment formed fibre kink-bands which act together to move a "wedge" of material upwards, thus leading to a different kink-band shape.

[Figure 15 about here.]

Even if fibre-matrix interfacial friction is expected to mostly affect the post-peak response, the effect of friction on the mechanical performance of the material, up to peak load, was studied. Two RVEs having different concentration parameters, i.e. $\kappa = 2000$ and $\kappa = 8000$ were analysed considering a frictionless ($\mu_\tau = 0$) interface. Figure 16a shows the longitudinal compressive reaction force vs. the applied displacement for the two RVEs having different interfacial friction coefficients. The difference in peak load is larger for the RVE having the highest degree of misalignment, exhibiting a difference in approximately 5%, where the less misaligned RVE did not show any substantial decrease in peak load, i.e. less than 0.01%. This is due to the amount of frictional energy that is dissipated during damage propagation (see Figure 16b). As shown, the amount of energy dissipated by friction is much greater for the case of the RVE with $\kappa = 2000$, in comparison to the RVE with $\kappa = 8000$. The RVEs with a frictionless interface still exhibit a level of energy dissipation, since the general contact algorithm implements friction with self-contact.

[Figure 16 about here.]

3.1.4. Kink-band width and fibre rotation angle

The developed kink-band is characterised by certain features, namely its width, angle, and fibre rotation within the kink-band. There is strong empirical evidence which shows that for most thermoset-based composites, when the kink-band is formed (before softening), the fibres within the band rotate by an angle of $15° \leqslant \varphi_{kb}^{\mathrm{exp}} \leqslant 30°$ (Soutis et al., 1993, Moran et al., 1995, Vogler, Kyriakides, 2001, Gutkin et al., 2010b). In contrast, the values measured for both kink-band angle and width have been more disperse, i.e. $5° \leqslant \beta_{kb}^{\mathrm{exp}} \leqslant 30°$ (Kyriakides et al., 1995, Vogler et al., 2001, Lee, Soutis, 2007) and $25\ \mu\mathrm{m} \leqslant w_{kb}^{\mathrm{exp}} \leqslant 80\ \mu\mathrm{m}$ (Jelf, Fleck, 1992, Jumahat et al., 2010, Laffan et al., 2012, Zobeiry et al., 2015), respectively. The kink-band width, w_{kb}, is shown to increase with increasing radii of the fibrous reinforcements, i.e. $w_{kb} \propto R_f$ (Fleck et al., 1995, Budiansky et al., 1998), being approximately equal to 20 times the fibre radii (Soutis et al., 1993). The kink-band angle, β_{kb}, is not explored in this work, since, even if the applied BCs allow for its qualitative representation (in Figure 14d: $\beta_{kb} \approx 13°$), for its proper evaluation, for different κ, a thicker RVE is needed.

The kink-band width, w_{kb}, was computed as the distance between the two extreme points of the kink-band, which have the highest stress, as soon as the kink-band is formed, as suggested by Pimenta et al. (2009). The fibre rotation angle, φ_{kb}, was measured as the angle that the kink-band forms with a horizontal line. Figure 17 shows the local longitudinal stress along the kink-band for three different RVEs, having different degrees of misalignment, where both the kink-band width and fibre rotation angle are highlighted. Table 7 shows the estimated quantitative results of the kink-band width and fibre rotation angle, for different concentration parameters, κ. Moreover, the evolution of both w_{kb} and φ_{kb} were quantified for the case presented in Figure 11 - (A): $w_{kb} \approx 36$ μm and $\varphi_{kb} \approx 6°$; (B): $w_{kb} \approx 40$ μm and $\varphi_{kb} \approx 12°$; and (C1 ≡C2): $w_{kb} \approx 49$ μm and $\varphi_{kb} \approx 23°$.

[Figure 17 about here.]

[Table 7 about here.]

From the aforementioned results, the kink-band width was found to be independent of the initial fibre misalignment distribution. Looking at different fibre radii, a previous preliminary study conducted by the authors, presented by Catalanotti et al. (2020), showed that, for larger fibre radii and same material system, larger kink-band widths were estimated, i.e. $w_{kb} \approx 80$ μm. The fibre rotation angles seem to gradually decrease with κ, where smaller degrees of misalignment, at peak load, promote slightly smaller overall fibre rotation angles.

Despite the initial individual misalignment that each fibre presents when the kink-band is developed, all tend to have the same orientation inside the kink-band. This can be verified in Figure 18, where different fibres within the same RVE, having different initial misalignment distributions, just after peak load, exhibit similar orientation angles in the kink-band.

[Figure 18 about here.]

3.2. Longitudinal tension

To accurately capture the behaviour of composite materials in longitudinal tension, the RVEs must be large enough to capture both co-planar and disperse fibre break clusters. RVEs having an in-plane dimension of $H \approx 175$ μm and a longitudinal dimension of $L_x \approx 500$ μm, were generated. Due to the high computational cost that these FE models yield, and based on previous micromechanical simulations (Tavares et al., 2016, 2017), the aforementioned dimensions were deemed sufficient. These RVEs encompass approximately 600 fibres. For this stress state, RVEs having four different degrees of misalignment were considered: $\kappa = 4000$, $\kappa = 6000$, $\kappa = 8000$, and $\kappa = \infty$ (see equation (1) and Figure 8) and only one simulation was performed per configuration. The in-plane dimensions of each finite element are approximately 0.8 μm, whereas their longitudinal dimension is approximately $l_x^e = L_x/150 = 4$ μm. As mentioned by several authors (Watson, Smith, 1985, Gulino, Phoenix, 1991, Tavares et al., 2017), the Weibull distribution may lead to overestimations of the fibre strength at short gauge lengths, however, a refined discretisation of the microstructure for such long RVEs is needed. Since the objective of this work is to analyse the effect of fibre misalignment on the behaviour of the material, a Weibull distribution was deemed to be sufficiently accurate to represent the stochastic distribution of the tensile strength of the fibres. Moreover, even if there are several methods to determine clusters of broken fibres (Sibson, 1973, Murtagh, Contreras, 2012), here it is chosen to evaluate the formation of fibre break clusters in a qualitative way.

3.2.1. Global response and formation of fibre break clusters

The longitudinal stress-strain curves for the four different RVEs are shown in Figure 19. For a better understanding of the in-plane fibre break clustering process, three different points (associated with $\kappa = \infty$), corresponding to different applied strains, are highlighted, as well as the corresponding contour plots of the fibre (equation (6)) and matrix (equation (11)) damage, in the critical section of the RVE: 1) initial broken fibres, as well as damage in the surrounding matrix; 2) development of a critical cluster, causing; 3) the catastrophic failure of the material.

[Figure 19 about here.]

The overall longitudinal tensile mechanical response of the material is not substantially affected by the initial fibre misalignment. Even if the Young's modulus slightly decreases with decreasing κ (from $E_{11} \approx 125$ GPa to $E_{11} \approx 121$ GPa), the peak stresses are all very similar. With increasing strain, the number of broken fibres increase, leading to the formation of small clusters of broken fibres. Despite the misalignment, the same cluster-type formation was observed for all RVEs, where the maximum number of fibre fractures was qualitatively the same.

The majority of fibres did not fail in the same plane, leading to the formation of disperse clusters, where the locations of fibre breaks are observed in multiple locations along the length of the RVE (see Figure 20).

[Figure 20 about here.]

3.2.2. Local damage mechanisms

Certain local mechanisms such as the ineffective length, debond length, stress profile along a fibre, and the effect of fibre-matrix interfacial friction and misalignment, are analysed in this section. These local mechanisms are assessed with no *prior* cracks in the matrix, since they play an important role in the stress recovery of the broken fibre and consequently in the debond length (Swolfs et al., 2015b). Moreover, there are several parameters which locally affect the tensile damage process, such as, distribution of the microstructure, material properties of the matrix constituent, and strain-rate (Zeng et al., 1997, Heuvel van den et al., 2000, Zhao, Takeda, 2000, Hobbiebrunken et al., 2007, Foreman et al., 2009, Swolfs et al., 2015b, Tavares et al., 2017), where most of which were analysed by Tavares et al. (2019a) using the Spring Element Model (SEM).

The ineffective length is a measure of the stress recovery length of the fibre and can be defined as twice the length at which the broken fibre is able to carry 90% of the applied stress (Rosen, 1964). To analyse this effect, fibres which were far from the boundaries of the RVEs were chosen to give a more detailed evaluation of the local damage mechanisms. Figures 21a and Figures 21b show the contour plots of the longitudinal stress and cohesive interfacial damage along the length of a single fibre inside an RVE with $\kappa = \infty$, for different friction coefficients and same applied strain, just after fibre breakage. Fibre breakage was promoted at its centre, by artificially decreasing the local tensile strength of the central elements to 4050 MPa.

[Figure 21 about here.]

By increasing the friction coefficient, both ineffective and debond length are reduced, leading to a higher stress recovery profile of the fibre, slowing down the damage process. Moreover, Figure 21c shows the numerical predictions of the volumetrically homogenised longitudinal stress along the single fibre, for different friction coefficients. After fibre fracture, different interfacial friction coefficients lead to slightly different stress profiles, where for the same longitudinal position, a greater homogenised stress can be observed, leading to an ineffective length of ≈ 68 μm and ≈ 55 μm, for a frictionless interface and for one considering $\mu_\tau = 0.70$, respectively.

To locally assess the effect of fibre waviness, two different fibres positioned far from the boundaries of the RVE, having qualitatively a different degree of misalignment, were chosen inside an RVE with $\kappa = 4000$. In Figures 22a and 22b, the contour plots of the fibre-matrix interface damage and longitudinal stress, for the two different fibres are shown, and Figure 22c shows the volumetrically homogenised longitudinal stress of each cross-section, along each fibre, having qualitatively different degrees of misalignment for central elements having two different failure strains ($\varepsilon_f^0 = 0.6\%$ in red and $\varepsilon_f^0 = 1.1\%$ in blue). The friction coefficient was kept constant and equal to $\mu_\tau = 0.52$.

[Figure 22 about here.]

For both analysed failure strains, the ineffective length increases with initial fibre misalignment. The difference between the ineffective length of a fibre having a small and a high degree of misalignment, was approximately 10 μm, for both failure strains. Additionally, it was noted that the debonded length increases with increasing failure strain. The changes in the local damage mechanisms, due to initial fibre waviness, may alter the development of fibre break clustering, as they change the local stress redistribution to neighbouring fibres, after fibre breakage. However, the overall behaviour of the composite is not directly connected to the local effects acting on a single fibre, but a bigger collection of fibres, possibly making these individual damage mechanisms, which act in a particular region of a single fibre, negligible when comparing to the longitudinal tensile strength distribution.

4. Conclusions

The importance of representing the realistic 3D microstructure of UD composite materials was addressed in this work, namely when the material is submitted to a longitudinal (fibre-direction) stress state. A computational finite element micromechanics framework was built, using a recent methodology to generate the initial fibre misalignment via a combination of a stochastic process and an optimisation procedure (Catalanotti, Sebaey, 2019). RVEs having different degrees of misalignment were then generated to simulate the longitudinal compressive and tensile failure, and analyse the associated intrinsic damage mechanisms.

Different results associated with the compressive failure of the material by fibre kinking were obtained using the present framework. It was observed that by decreasing the degree of misalignment of the RVEs (increasing κ), both Young's modulus and peak stress increased, where these results have shown to have a best fit using linear and rational functions, respectively. The RVEs having a more realistic κ (experimentally obtained by Sebaey et al. (2019)), yielded peak stresses comparable to empirical compressive strengths of different material systems (Hexcel, 2016a,b). Moreover, the present framework enabled the analysis of the kink-band width and of the fibre rotation inside the kink-band. The kink-band width was found to be independent of initial fibre waviness, in contrast, the fibre rotation angle was sensitive to it, where bigger degrees of initial misalignment lead to higher fibre rotation angles. Additionally, despite having different initial misalignment, after peak load, fibres which belong to the same RVE, exhibited similar orientation angles, in the kink-band region. Finally, friction seems to play a role for lower concentration parameters (higher misalignment), in which the energy dissipated by friction was higher.

The failure mechanisms associated with a longitudinal tensile loading were also evaluated. By generating RVEs with different fibre misalignments, the overall performance of the material remained unaltered, i.e. the peak stress remained the same and the Young's modulus changed slightly. Moreover, the RVEs exhibited similar damage patterns, leading to a similar type of fibre break clustering. More detailed analyses were undertaken to assess the effect of friction and degree of misalignment on the local load carrying capacity of the broken fibres. Friction was shown to decrease the ineffective length of the fibres, whereas misalignment increased the ineffective length, possibly leading to a faster progression of damage, changing the stress redistribution to neighbouring fibres. However, these local phenomena do not seem to dictate the final failure of the material, making the variation of the longitudinal tensile strength of the reinforcements the most influential parameter on the final failure of the material.

Idealised representations of the microstructure cannot properly represent fibre kinking. In contrast, a more realistic spatial distribution (Catalanotti, Sebaey, 2019) guarantees a correct representation of the damage mechanisms associated with longitudinal compressive failure of UD materials. Despite the magnitude of the initial fibre misalignment, the longitudinal tensile behaviour and failure mechanisms were all very similar. There are certain limitations which were not assessed here. Fibre compressive and/or shear failure was not considered, due to a lack of strength characterisation testing of neat fibres, which can lead to an overestimation of the local and overall performance of the material for small degrees of fibre misalignment. Finally, there is a need for developing analytical/semi-analytical models which are able to take into account the stochastic variability of the initial waviness of the reinforcements, thus yielding representative estimations of the parameters associated with compressive failure by fibre kinking.

This study has shown that micromechanics can be treated as a reliable computational tool to analyse certain geometric and material variabilities which cannot be assessed using ply- or laminate-level analyses. Further studies can encompass the investigation of the effect of initial fibre waviness on the transverse tensile and compressive response, in- and out-of-plane shear loading scenarios, as well as other biaxial and triaxial loading conditions.

Data availability

Datasets related to this article can be found at http://dx.doi.org/10.17632/4kbd2fr4yf.2, an open-source online data repository hosted at Mendeley Data.

Acknowledgements

The authors gratefully acknowledge the financial support of the project ICONIC – Improving the crashworthiness of composite transportation structures. ICONIC has received funding from the European Union's Horizon 2020 research and innovation programme under the Marie Skłodowska-Curie grant agreement No 721256. The content reflects only the author's view and the Agency is not responsible for any use that may be made of the information it contains.

References

Abaqus Documentation. Providence, RI, USA, 2018.

Argon A.S. Fracture of Composites // Treatise on Materials Science & Technology. 1972. 79–114.

Arteiro A., Catalanotti G., Melro A. R., Linde P., Camanho P. P. Micro-mechanical analysis of the in situ effect in polymer composite laminates // Composite Structures. 2014. 116, 1. 827–840.

Arteiro A., Catalanotti G., Melro A. R., Linde P., Camanho P. P. Micro-mechanical analysis of the effect of ply thickness on the transverse compressive strength of polymer composites // Composites Part A: Applied Science and Manufacturing. 2015. 79. 127–137.

Arteiro Albertino, Catalanotti Giuseppe, Reinoso José, Linde Peter, Camanho Pedro P. Simulation of the Mechanical Response of Thin-Ply Composites: From Computational Micro-Mechanics to Structural Analysis // Archives of Computational Methods in Engineering. nov 2019. 26, 5. 1445–1487.

Bai Xiaoming, Bessa Miguel A., Melro António R., Camanho Pedro P., Guo Licheng, Liu Wing K. High-fidelity micro-scale modeling of the thermo-visco-plastic behavior of carbon fiber polymer matrix composites // Composite Structures. 2015. 134. 132–141.

Bažant Z. P., Kim Jang-jay H., Daniel Isaac M., Becq-Giraudon Emilie, Zi G. Size effect on compression strength of fiber composites failing by kink band propagation // International Journal of Fracture. 1999. 07, 1984. 103–141.

Bažant Z. P., Oh B. H. Crack band theory for fracture of concrete // Materials and Structures. 1983. 16. 155–177.

Benzeggagh M. L., Kenane M. Measurement of mixed-mode delamination fracture toughness of unidirectional glass/epoxy composites with mixed-mode bending apparatus // Composites Science and Technology. 1996. 56, 4. 439–449.

Beyerlein Irene J., Phoenix S.Leigh. Statistics for the strength and size effects of microcomposites with four carbon fibers in epoxy resin // Composites Science and Technology. jan 1996. 56, 1. 75–92.

Bishara M., Rolfes R., Allix O. Revealing complex aspects of compressive failure of polymer composites Part I: Fiber kinking at microscale // Composite Structures. jun 2017. 169. 105–115.

Budiansky B., Fleck N.A. Compressive failure of fibre composites // Journal of the Mechanics and Physics of Solids. jan 1993. 41, 1. 183–211.

Budiansky B., Fleck N.A., Amazigo J.C. On kink-band propagation in fiber composites // Journal of the Mechanics and Physics of Solids. sep 1998. 46, 9. 1637–1653.

Budiansky Bernard. Micromechanics // Computers & Structures. jan 1983. 16, 1-4. 3–12.

Budiansky Bernard, Fleck Norman A. Compressive Kinking of Fiber Composites: A Topical Review // Applied Mechanics Reviews. jun 1994. 47, 6S. S246–S250.

Catalanotti G. On the generation of RVE-based models of composites reinforced with long fibres or spherical particles // Composite Structures. 2016. 138. 84–95.

Catalanotti G., Sebaey T.A. An algorithm for the generation of three-dimensional statistically Representative Volume Elements of unidirectional fibre-reinforced plastics: Focusing on the fibres waviness // Composite Structures. nov 2019. 227. 111272.

Catalanotti G., Varandas L.F., Melro A.R., Sebaey T.A., Bessa M.A., Falzon B.G. Modelling the longitudinal failure of fibre-reinforced composites at micro-scale // Multi-Scale Continuum Mechanics Modelling of Fibre-Reinforced Polymer Composites. 2020. Chapter 12. Submitted.

Chen Zhangxing, Tang Haibin, Shao Yimin, Sun Qingping, Zhou Guowei, Li Yang, Xu Hongyi, Zeng Danielle, Su Xuming. Failure of chopped carbon fiber Sheet Molding Compound (SMC) composites under uniaxial tensile loading: Computational prediction and experimental analysis // Composites Part A: Applied Science and Manufacturing. mar 2019. 118. 117–130.

Clarke A.R., Archenhold G., Davidson N.C. A novel technique for determining the 3D spatial distribution of glass fibres in polymer composites // Composites Science and Technology. jan 1995. 55, 1. 75–91.

Costa Sérgio, Fagerström Martin, Olsson Robin. Development and validation of a finite deformation fibre kinking model for crushing of composites // Composites Science and Technology. may 2020. 108236.

Creighton C.J, Sutcliffe M.P.F, Clyne T.W. A multiple field image analysis procedure for characterisation of fibre alignment in composites // Composites Part A: Applied Science and Manufacturing. feb 2001. 32, 2. 221–229.

Curtin W. A. Tensile Strength of Fiber-Reinforced Composites: III. Beyond the Traditional Weibull Model for Fiber Strengths // Journal of Composite Materials. aug 2000. 34, 15. 1301–1332.

Dalli D., Catalanotti G., Varandas L.F., Falzon B.G., Foster S. Mode I intralaminar fracture toughness of 2D woven carbon fibre reinforced composites: A comparison of stable and unstable crack propagation techniques // Engineering Fracture Mechanics. jun 2019. 214. 427–448.

Dalli D., Catalanotti G., Varandas L.F., Falzon B.G., Foster S. Compressive intralaminar fracture toughness and residual strength of 2D Woven carbon fibre reinforced composites: New developments on using the size effect method // Theoretical and Applied Fracture Mechanics. jan 2020. 102487.

Daum B., Feld N., Allix O., Rolfes R. A review of computational modelling approaches to compressive failure in laminates // Composites Science and Technology. sep 2019. 181. 107663.

Fleck N. A., Deng L., Budiansky B. Prediction of Kink Width in Compressed Fiber Composites // Journal of Applied Mechanics. jun 1995. 62, 2. 329–337.

Foreman J. P., Behzadi S., Tsampas S. A., Porter D., Curtis P. T., Jones F. R. Rate dependent multiscale modelling of fibre reinforced composites // Plastics, Rubber and Composites. may 2009. 38, 2-4. 67–71.

Galli M., Botsis J., Janczak-Rusch J. An elastoplastic three-dimensional homogenization model for particle reinforced composites // Computational Materials Science. 2008. 41, 3. 312–321.

Ghorbel Elhem. A viscoplastic constitutive model for polymeric materials // International Journal of Plasticity. nov 2008. 24, 11. 2032–2058.

Gitman I. M., Askes H., Sluys L. J. Representative volume: Existence and size determination // Engineering Fracture Mechanics. 2007. 74, 16. 2518–2534.

Gitman I. M., Gitman M. B., Askes H. Quantification of stochastically stable representative volumes for random heterogeneous materials // Archive of Applied Mechanics. jan 2006. 75, 2-3. 79–92.

Guerrero J.M., Mayugo J.A., Costa J., Turon A. A 3D Progressive Failure Model for predicting pseudo-ductility in hybrid unidirectional composite materials under fibre tensile loading // Composites Part A: Applied Science and Manufacturing. apr 2018. 107. 579–591.

Gulino R., Phoenix S. L. Weibull strength statistics for graphite fibres measured from the break progression in a model graphite/glass/epoxy microcomposite // Journal of Materials Science. 1991. 26, 11. 3107–3118.

Gutkin R., Pinho S. T., Robinson P., Curtis P. T. Micro-mechanical modelling of shear-driven fibre compressive failure and of fibre kinking for failure envelope generation in CFRP laminates // Composites Science and Technology. 2010a. 70, 8. 1214–1222.

Gutkin R., Pinho S. T., Robinson P., Curtis P. T. On the transition from shear-driven fibre compressive failure to fibre kinking in notched CFRP laminates under longitudinal compression // Composites Science and Technology. 2010b. 70, 8. 1223–1231.

Hashin Z. Analysis of Composite Materials - A Survey // Journal of Applied Mechanics. sep 1983. 50, 3. 481–505.

Herráez M., Bergan A.C., Lopes C.S., González C. Computational micromechanics model for the analysis of fiber kinking in unidirectional fiber-reinforced polymers // Mechanics of Materials. mar 2020. 142. 103299.

Herráez M., Fernández A., Lopes C. S., González C. Strength and toughness of structural fibres for composite material reinforcement // Philosophical Transactions of the Royal Society A: Mathematical, Physical and Engineering Sciences. 2016. 374, 2071.

Herráez Miguel, Bergan Andrew C., González Carlos. Modeling fiber kinking at the microscale and mesoscale. // Technical report, NASA/TP2018220105. 2018. October.

Heuvel P. W. J. van den, Peijs T., Young R. J. Failure phenomena in two-dimensional multi-fibre micro-composites. Part 4: a Raman spectroscopic study on the influence of the matrix yield stress on stress concentrations // Composites Part A: Applied Science and Manufacturing. feb 2000. 31, 2. 165–171.

Hexcel . HexPly® 8552 Matrix, Epoxy matrix (180° C/356° F curing) // https://www.hexcel.com/user_area/content_media/raw/HexPly_8552_eu_DataSheet.pdf. 2016a.

Hexcel . HexPly® M21 Matrix, Epoxy matrix (180° C/356° F curing) // https://www.hexcel.com/user_area/content_media/raw/HexPly_M21_global_DataSheet.pdf. 2016b.

Hill R. Elastic properties of reinforced solids: Some theoretical principles // Journal of the Mechanics and Physics of Solids. sep 1963. 11, 5. 357–372.

Hillig W. B. Effect of fibre misalignment on the fracture behaviour of fibre-reinforced composites // Journal of Materials Science. 1994. 29, 2. 419–423.

Hobbiebrunken Thomas, Fiedler Bodo, Hojo Masaki, Tanaka Mototsugu. Experimental determination of the true epoxy resin strength using micro-scaled specimens // Composites Part A: Applied Science and Manufacturing. mar 2007. 38, 3. 814–818.

Hsu S.-Y., Vogler T. J., Kyriakides S. Compressive Strength Predictions for Fiber Composites // Journal of Applied Mechanics. mar 1998. 65, 1. 7–16.

Jelf P.M., Fleck N.A. Compression Failure Mechanisms in Unidirectional Composites // Journal of Composite Materials. dec 1992. 26, 18. 2706–2726.

Jumahat A., Soutis C., Jones F. R., Hodzic A. Fracture mechanisms and failure analysis of carbon fibre / toughened epoxy composites subjected to compressive loading // Composite Structures. 2010. 92, 2. 295–305.

Kanit T., Forest S., Galliet I., Mounoury V., Jeulin D. Determination of the size of the representative volume element for random composites: statistical and numerical approach // International Journal of Solids and Structures. jun 2003. 40, 13-14. 3647–3679.

Kyriakides S., Arseculeratne R., Perry E.J., Liechti K.M. On the compressive failure of fiber reinforced composites // International Journal of Solids and Structures. mar 1995. 32, 6-7. 689–738.

Laffan M.J., Pinho S.T., Robinson P., Iannucci L. Measurement of the in situ ply fracture toughness associated with mode I fibre tensile failure in FRP. Part II: Size and lay-up effects // Composites Science and Technology. apr 2010. 70, 4. 614–621.

Laffan M.J., Pinho S.T., Robinson P., Iannucci L., McMillan A.J. Measurement of the fracture toughness associated with the longitudinal fibre compressive failure mode of laminated composites // Composites Part A: Applied Science and Manufacturing. nov 2012. 43, 11. 1930–1938.

Lamon Jacques. Mécanique de la rupture fragile et de l'endommagement : Approches statistiques et probabilistes. Paris: Hermès Science Publications, 2007. Hermes-Lav.

Lee J., Soutis C. A study on the compressive strength of thick carbon fibreepoxy laminates // Composites Science and Technology. aug 2007. 67, 10. 2015–2026.

Lin Ye . Role of matrix resin in delamination onset and growth in composite laminates // Composites Science and Technology. 1988. 33, 4. 257–277.

Meer Frans P. van der, Raijmaekers Sibrand, Rocha Iuri B.C.M. Interpreting the single fiber fragmentation test with numerical simulations // Composites Part A: Applied Science and Manufacturing. mar 2019. 118. 259–266.

Melro A. R., Camanho P. P., Andrade Pires F. M., Pinho S. T. Micromechanical analysis of polymer composites reinforced by unidirectional fibres: Part I-Constitutive modelling // International Journal of Solids and Structures. 2013a. 50, 11-12. 1897–1905.

Melro A. R., Camanho P. P., Andrade Pires F. M., Pinho S. T. Micromechanical analysis of polymer composites reinforced by unidirectional fibres: Part II-Micromechanical analyses // International Journal of Solids and Structures. 2013b. 50, 11-12. 1906–1915.

Mizukami Koichi, Mizutani Yoshihiro, Todoroki Akira, Suzuki Yoshiro. Detection of in-plane and out-of-plane fiber waviness in unidirectional carbon fiber reinforced composites using eddy current testing // Composites Part B: Engineering. feb 2016. 86. 84–94.

Moran P. M., Liu X. H., Shih C. F. Kink band formation and band broadening in fiber composites under compressive loading // Acta Metallurgica et Materialia. 1995. 43, 8. 2943–2958.

Murtagh Fionn, Contreras Pedro. Algorithms for hierarchical clustering: an overview // Wiley Interdisciplinary Reviews: Data Mining and Knowledge Discovery. jan 2012. 2, 1. 86–97.

Naya F., Herráez M., Lopes C. S., González C., Van der Veen S., Pons F. Computational micromechanics of fiber kinking in unidirectional FRP under different environmental conditions // Composites Science and Technology. 2017. 144. 26–35.

Pain Damien, Drinkwater Bruce W. Detection of Fibre Waviness Using Ultrasonic Array Scattering Data // Journal of Nondestructive Evaluation. sep 2013. 32, 3. 215–227.

Pimenta S., Gutkin R., Pinho S.T., Robinson P. A micromechanical model for kink-band formation: Part IIAnalytical modelling // Composites Science and Technology. jun 2009. 69, 7-8. 956–964.

Pinho S. T., Gutkin R., Pimenta S., De Carvalho N. V., Robinson P. On longitudinal compressive failure of carbon-fibre-reinforced polymer: from unidirectional to woven, and from virgin to recycled // Philosophical Transactions of the Royal Society A: Mathematical, Physical and Engineering Sciences. apr 2012. 370, 1965. 1871–1895.

Prabhakar Pavana, Waas Anthony M. Interaction between kinking and splitting in the compressive failure of unidirectional fiber reinforced laminated composites // Composite Structures. 2013. 98. 85–92.

Requena Guillermo, Fiedler Georg, Seiser Bernhard, Degischer Peter, Di Michiel Marco, Buslaps Thomas. 3D-Quantification of the distribution of continuous fibres in unidirectionally reinforced composites // Composites Part A: Applied Science and Manufacturing. feb 2009. 40, 2. 152–163.

Rosen B. W. Tensile failure of fibrous composites // AIAA Journal. nov 1964. 2, 11. 1985–1991.

Scott A. E., Mavrogordato M., Wright P., Sinclair I., Spearing S. M. In situ fibre fracture measurement in carbonepoxy laminates using high resolution computed tomography // Composites Science and Technology. aug 2011. 71, 12. 1471–1477.

Scott A. E., Sinclair I., Spearing S. M., Thionnet A., Bunsell A. R. Damage accumulation in a carbon/epoxy composite: Comparison between a multiscale model and computed tomography experimental results // Composites Part A: Applied Science and Manufacturing. sep 2012. 43, 9. 1514–1522.

Sebaey T. A., Catalanotti G., Dowd N. P. O. A microscale integrated approach to measure and model fi bre misalignment in fi bre-reinforced composites // Composites Science and Technology. 2019. 183, June. 107793.

Sibson R. SLINK: An optimally efficient algorithm for the single-link cluster method // The Computer Journal. jan 1973. 16, 1. 30–34.

Soden P., Hinton M. J., Kaddour A. S. Lamina properties, lay-up configurations and loading conditions for a range of fibre-reinforced composite laminates // Composites Science and Technology. jul 1998. 58, 7. 1011–1022.

Soutis C., Curtis P. T., Fleck N. A. Compressive Failure of Notched Carbon Fibre Composites // Proceedings of the Royal Society A: Mathematical, Physical and Engineering Sciences. feb 1993. 440, 1909. 241–256.

St-Pierre Luc, Martorell Ned J., Pinho Silvestre T. Stress redistribution around clusters of broken fibres in a composite // Composite Structures. may 2017. 168. 226–233.

Stroeven M., Askes H., Sluys L.J. Numerical determination of representative volumes for granular materials // Computer Methods in Applied Mechanics and Engineering. jul 2004. 193, 30-32. 3221–3238.

Sun Qingping, Zhou Guowei, Guo Haiding, Meng Zhaoxu, Chen Zhangxing, Liu Haolong, Kang Hongtae, Su Xuming. Failure mechanisms of cross-ply carbon fiber reinforced polymer laminates under longitudinal compression with experimental and computational analyses // Composites Part B: Engineering. jun 2019a. 167. 147–160.

Sun Qingping, Zhou Guowei, Meng Zhaoxu, Guo Haiding, Chen Zhangxing, Liu Haolong, Kang Hongtae, Keten Sinan, Su Xuming. Failure criteria of unidirectional carbon fiber reinforced polymer composites informed by a computational micromechanics model // Composites Science and Technology. mar 2019b. 172. 81–95.

Sutcliffe M. P. F., Lemanski S. L., Scott A. E. Measurement of fibre waviness in industrial composite components // Composites Science and Technology. 2012. 72, 16. 2016–2023.

Swolfs Y., Morton H., Scott A. E., Gorbatikh L., Reed P. A. S., Sinclair I., Spearing S. M., Verpoest I. Synchrotron radiation computed tomography for experimental validation of a tensile strength model for unidirectional fibre-reinforced composites // Composites Part A: Applied Science and Manufacturing. oct 2015a. 77. 106–113.

Swolfs Yentl, McMeeking Robert M., Verpoest Ignaas, Gorbatikh Larissa. Matrix cracks around fibre breaks and their effect on stress redistribution and failure development in unidirectional composites // Composites Science and Technology. 2015b. 108. 16–22.

Swolfs Yentl, McMeeking Robert M., Verpoest Ignaas, Gorbatikh Larissa. The effect of fibre dispersion on initial failure strain and cluster development in unidirectional carbon/glass hybrid composites // Composites Part A: Applied Science and Manufacturing. 2015c. 69. 279–287.

Swolfs Yentl, Verpoest Ignaas, Gorbatikh Larissa. Maximising the hybrid effect in unidirectional hybrid composites // Materials & Design. mar 2016. 93. 39–45.

Tanaka Fumihiko, Okabe Tomonaga, Okuda Haruki, Kinloch Ian A., Young Robert J. Factors controlling the strength of carbon fibres in tension // Composites Part A: Applied Science and Manufacturing. 2014. 57. 88–94.

Tavares Rodrigo P., Guerrero Jose M., Otero Fermin, Turon Albert, Mayugo Joan A., Costa Josep, Camanho Pedro P. Effects of local stress fields around broken fibres on the longitudinal failure of composite materials // International Journal of Solids and Structures. jan 2019a. 156-157. 294–305.

Tavares Rodrigo P., Melro António R., Bessa Miguel A., Turon Albert, Liu Wing K., Camanho Pedro P. Mechanics of hybrid polymer composites: analytical and computational study // Computational Mechanics. 2016. 57, 3. 405–421.

Tavares Rodrigo P., Otero Fermin, Baiges Joan, Turon Albert, Camanho Pedro P. A dynamic spring element model for the prediction of longitudinal failure of polymer composites // Computational Materials Science. 2019b. 160, January. 42–52.

Tavares Rodrigo P., Otero Fermin, Turon Albert, Camanho Pedro P. Effective simulation of the mechanics of longitudinal tensile failure of unidirectional polymer composites // International Journal of Fracture. 2017. 208, 1. 269–285.

Thionnet A., Chou H.Y., Bunsell A. Fibre break processes in unidirectional composites // Composites Part A: Applied Science and Manufacturing. oct 2014. 65. 148–160.

Torres J. P., Vandi L. J., Veidt M., Heitzmann M. T. The mechanical properties of natural fibre composite laminates: A statistical study // Composites Part A: Applied Science and Manufacturing. 2017. 98, March. 99–104.

Triantafyllidis N., Bardenhagen S. The influence of scale size on the stability of periodic solids and the role of associated higher order gradient continuum models // Journal of the Mechanics and Physics of Solids. nov 1996. 44, 11. 1891–1928.

Tschoegl N. W. Failure surfaces in principal stress space // Journal of polymer science Part C: Polymer symposia. 1971. 32, 1. 239–267.

Varandas L.F., Arteiro A., Bessa M.A., Melro A.R., Catalanotti G. The effect of through-thickness compressive stress on mode II interlaminar crack propagation: A computational micromechanics approach // Composite Structures. 2017. 182, September. 326–334.

Varandas L.F., Arteiro A., Catalanotti G., Falzon B.G. Micromechanical analysis of interlaminar crack propagation between angled plies in mode I tests // Composite Structures. 2019. 220, December 2018. 827–841.

Varandas L.F., Catalanotti G., Arteiro A., Melro A.R., Falzon B.G. Micromechanical modelling of interlaminar damage propagation and migration // Multi-Scale Continuum Mechanics Modelling of Fibre-Reinforced Polymer Composites. 2020a. Chapter 11. Submitted.

Varandas Luís F., Catalanotti Giuseppe, Melro António R., Falzon Brian G. On the importance of nesting considerations for accurate computational damage modelling in 2D woven composite materials // Computational Materials Science. feb 2020b. 172. 109323.

Vogler T. J., Hsu S. Y., Kyriakides S. On the initiation and growth of kink bands in fiber composites. Part II: Analysis // International Journal of Solids and Structures. 2001. 38, 15. 2653–2682.

Vogler T. J., Kyriakides S. On the initiation and growth of kink bands in fiber composites: Part I. experiments // International Journal of Solids and Structures. 2001. 38, 15. 2639–2651.

Wang Ying, Chai Yuan, Soutis Costas, Withers Philip J. Evolution of kink bands in a notched unidirectional carbon fibre-epoxy composite under four-point bending // Composites Science and Technology. mar 2019. 172. 143–152.

Watson A. S., Smith R. L. An examination of statistical theories for fibrous materials in the light of experimental data // Journal of Materials Science. sep 1985. 20, 9. 3260–3270.

Weibull Waloddi. A statistical distribution function of wide applicability // Journal of applied mechanics. 1951. 103. 293–297.

Wilhelmsson D., Asp L.E. A high resolution method for characterisation of fibre misalignment angles in composites // Composites Science and Technology. sep 2018. 165. 214–221.

Yerramalli Chandra S., Waas Anthony M. The effect of fiber diameter on the compressive strength of composites - A 3D finite element based study // CMES - Computer Modeling in Engineering and Sciences. 2004. 6, 1. 1–16.

Zeng Qing-Dun, Wang Zhi-Li, Ling Ling. A study of the influence of interfacial damage on stress concentrations in unidirectional composites // Composites Science and Technology. jan 1997. 57, 1. 129–135.

Zhao F.M, Takeda N. Effect of interfacial adhesion and statistical fiber strength on tensile strength of unidirectional glass fiber/epoxy composites. Part I: experiment results // Composites Part A: Applied Science and Manufacturing. nov 2000. 31, 11. 1203–1214.

Zobeiry N., Vaziri R., Poursartip A. Characterization of strain-softening behavior and failure mechanisms of composites under tension and compression // Composites Part A: Applied Science and Manufacturing. 2015. 68. 29–41.

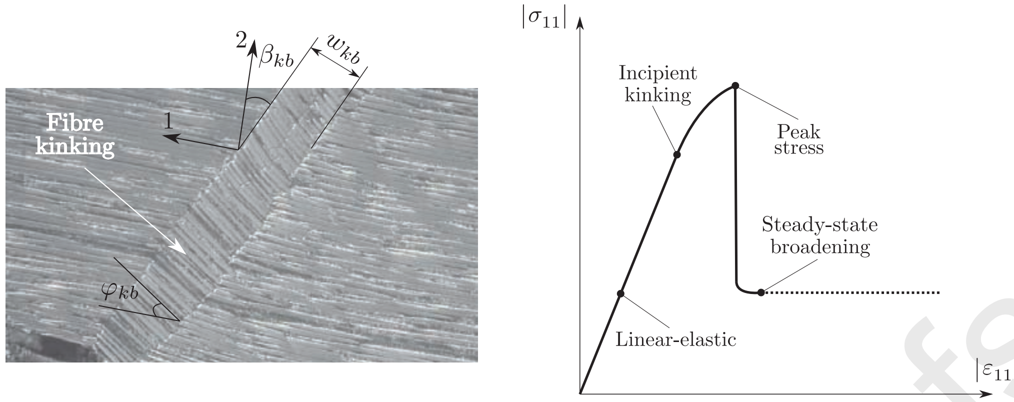

(a) (b)

Figure 1: (a) Micrograph of a developed kink-band, highlighting its width, w_{kb}, angle, β_{kb}, and the fibre rotation angle, φ_{kb}, from Jumahat et al. (2010) (with permission); (b) schematic representation of the longitudinal compressive response of an UD composite material, highlighting the different loading stages.

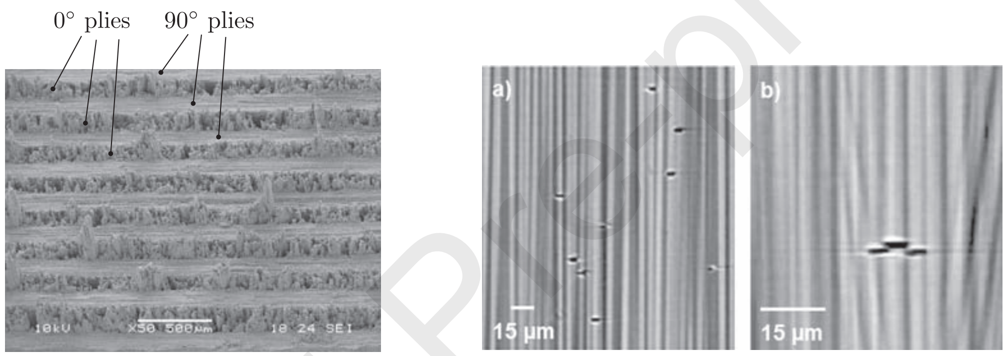

(a) (b)

Figure 2: (a) CT image of a fracture surface of a cross-ply laminate, from Laffan et al. (2010) (with permission) and (b) SRCT image of disperse (left) and co-planar (right) fibre break clusters, from Swolfs et al. (2015a) (with permission).

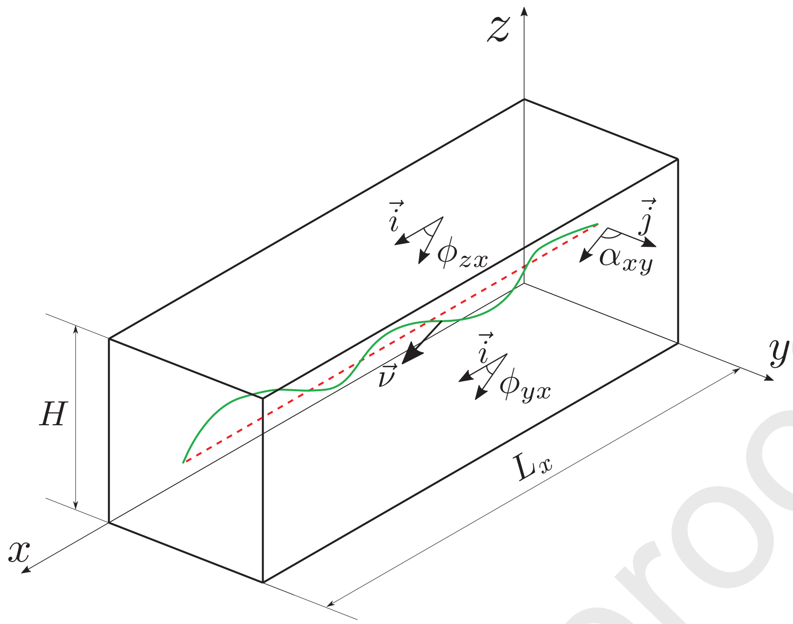

Figure 3: Spatial descriptors that characterise 3D fibre waviness (the green line portraits a representative fibre).

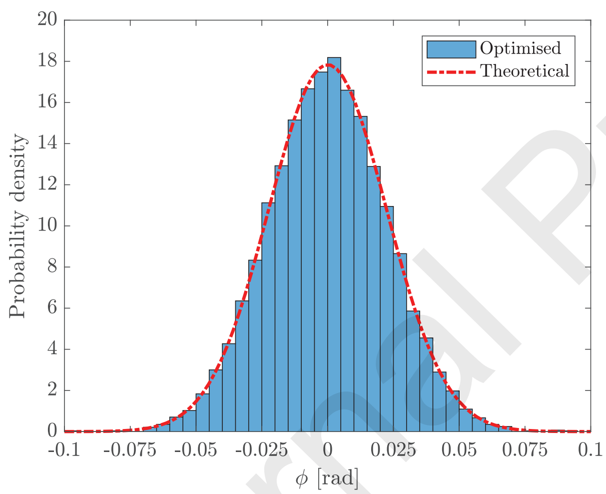

(a) pdf of the distribution.

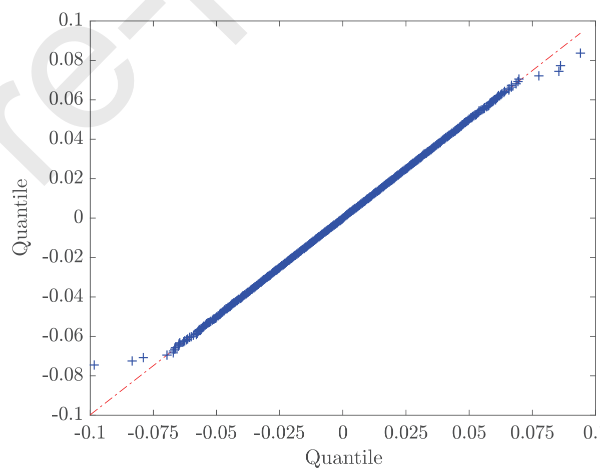

(b) Q-Q plot.

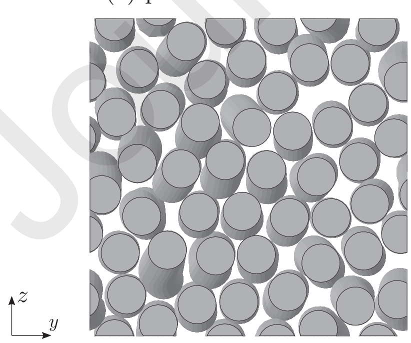

(c) Front view of the fibres.

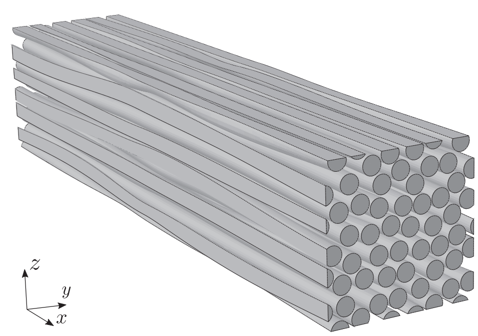

(d) Isometric view of the fibres.

Figure 4: Results associated with a 3D fibre distribution with $\kappa = 2000$.

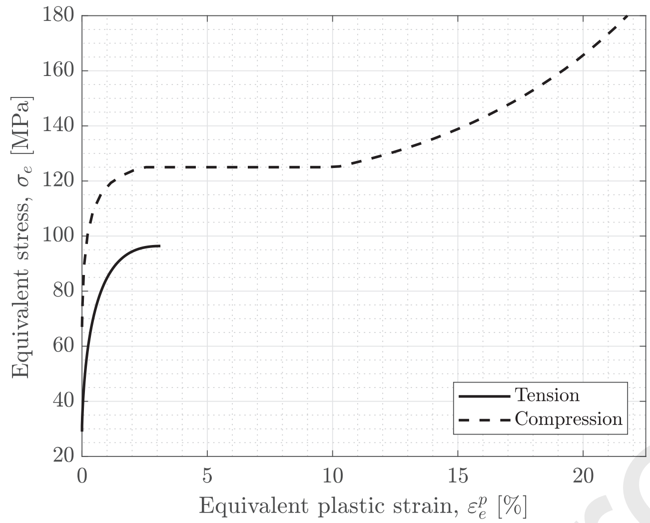

Figure 5: Hardening curves used in the epoxy matrix plasticity model (Melro et al., 2013b, Arteiro et al., 2014, 2015).

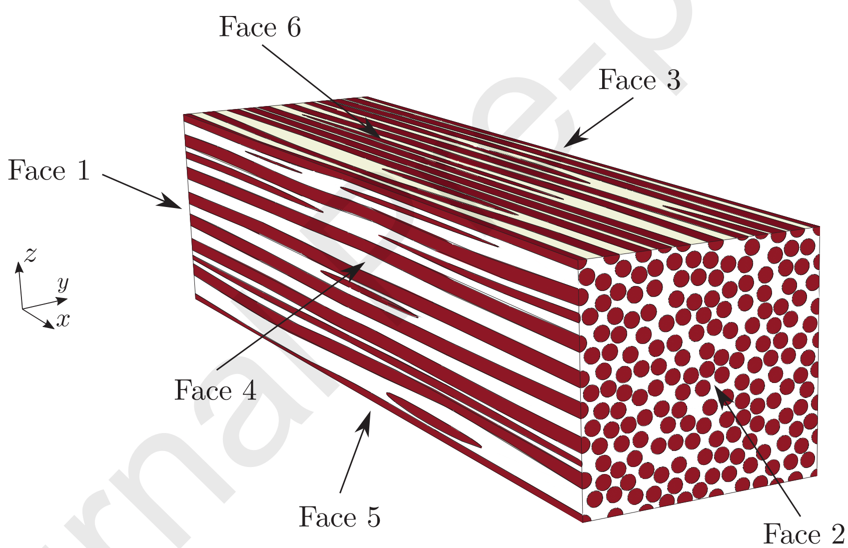

Figure 6: Representation of a misaligned micromechanical RVE, highlighting its different faces. White - epoxy matrix; red - carbon fibres.

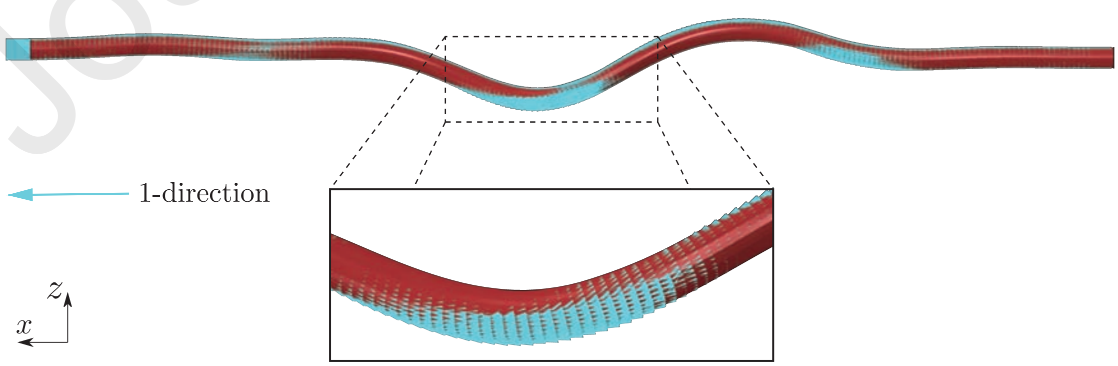

Figure 7: Representation of the main, 1-direction, of each element of a highly misaligned fibre.

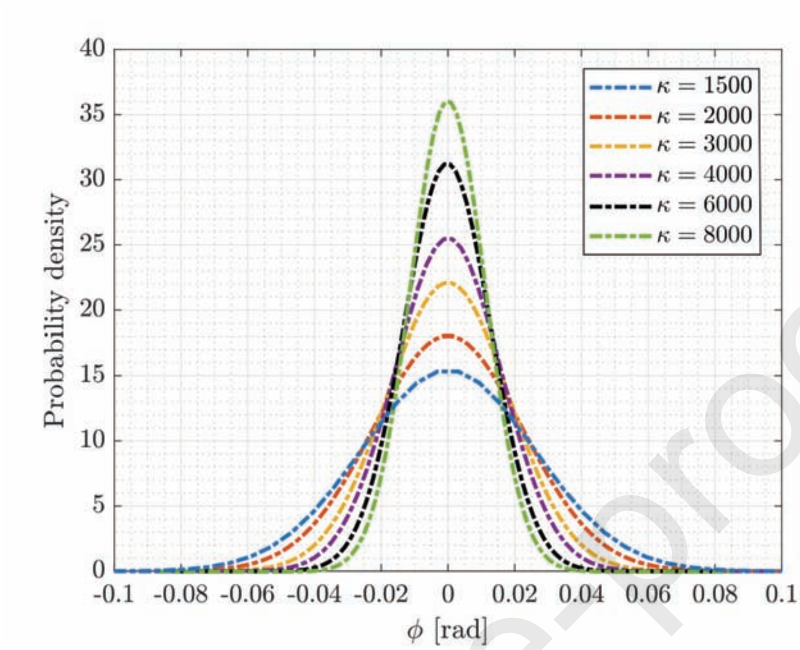

Figure 8: Distribution of the misalignment angles for each κ considered in this section.

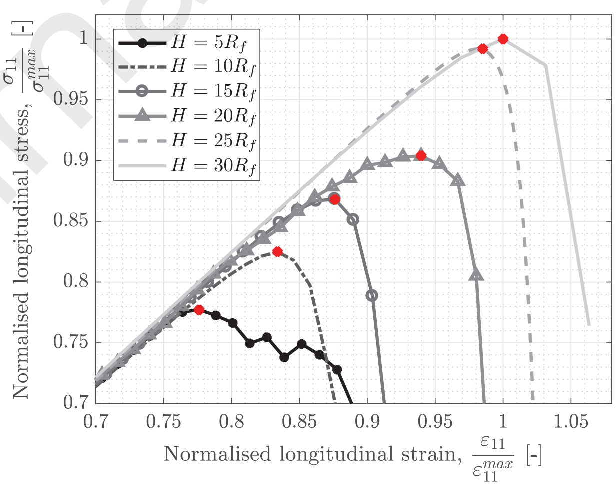

Figure 9: Representative normalised longitudinal compression stress-strain curves for different in-plane dimensions of the RVE, having a constant aspect ratio of $A_r = 4$. The red points indicate the corresponding normalised peak stress.

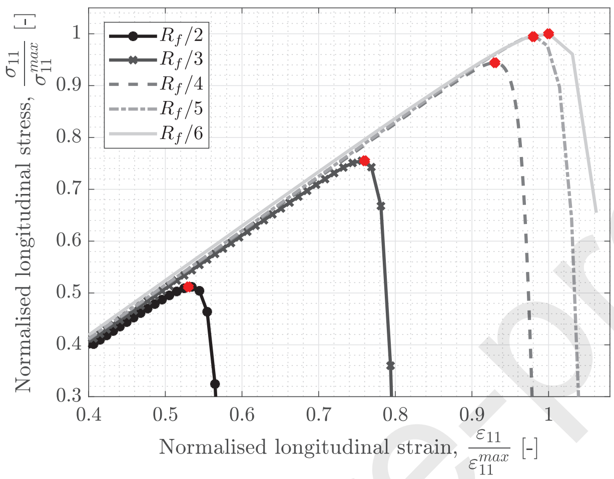

(a) Normalised compressive stress-strain curves for different average mesh densities. The red points indicate the corresponding normalised peak stress.

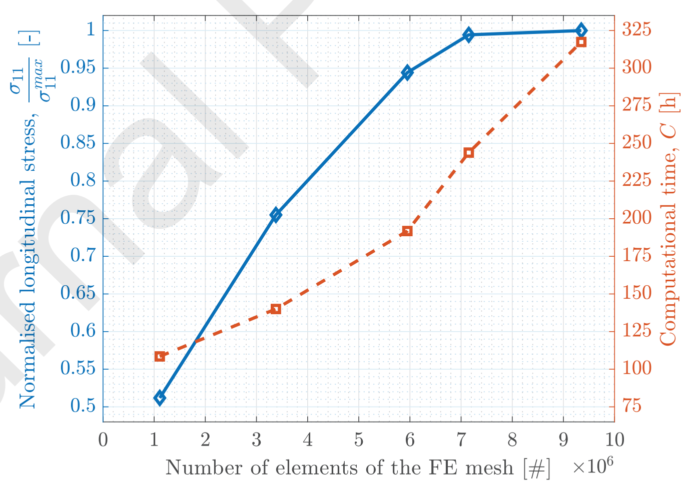

(b) Normalised compressive peak stress and corresponding computational cost vs. mesh density.

Figure 10: Preliminary results to assess the effect of mesh density on the quantitative results ($\kappa = 4000$).

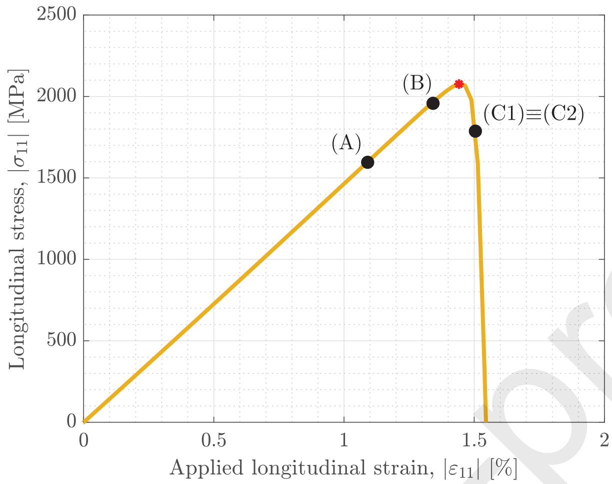

(a) Representative stress-strain curve. The red point indicates the peak stress.

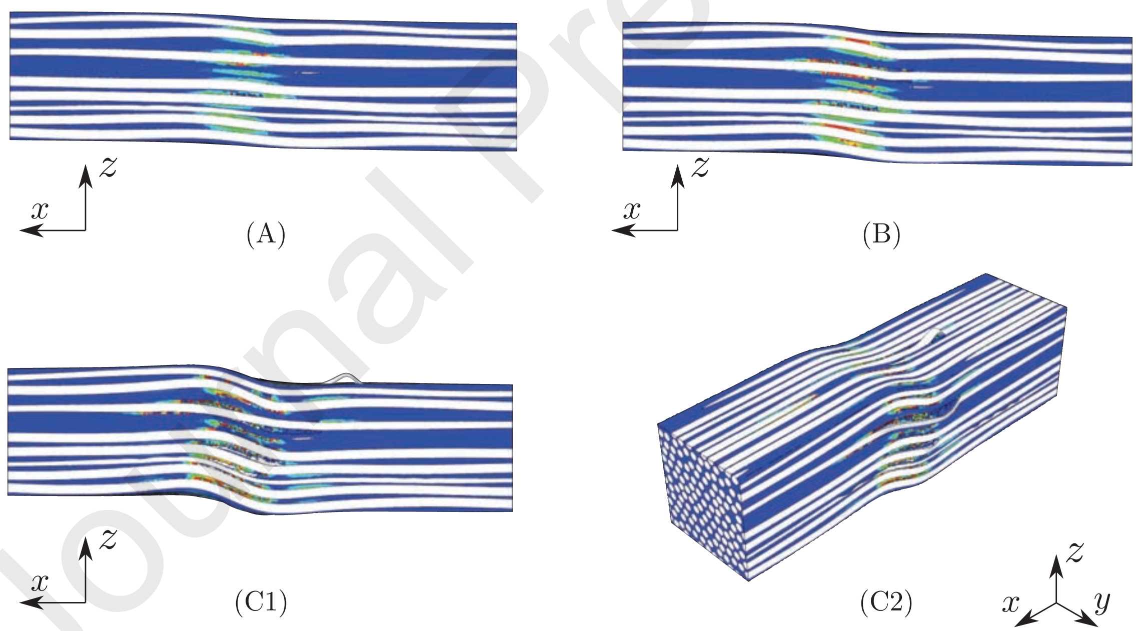

(b) Contour plots of the equivalent plastic strain of the epoxy matrix, at different stages of the damage process (blue - 0.0; yellow - 0.19; red - 0.25).

Figure 11: Numerical results associated with an RVE with $\kappa = 3000$, in longitudinal compression.

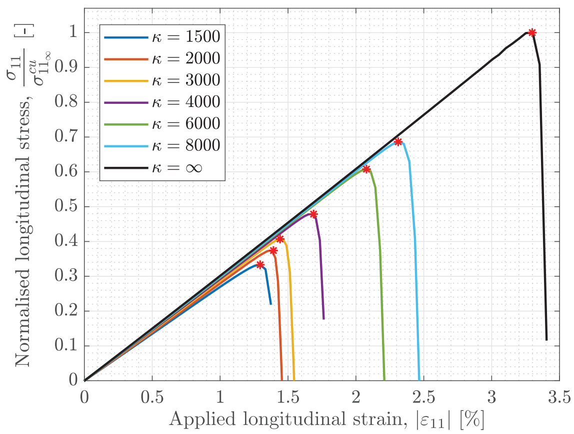

(a) Normalised representative stress-strain curves. The red points indicate the associated normalised peak stress.

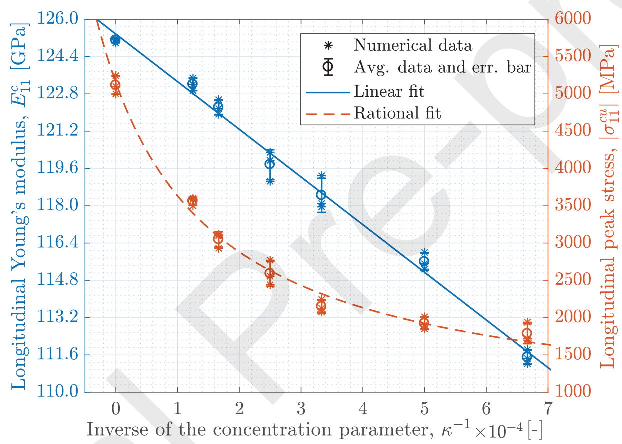

(b) Sensitivity results for the compressive Young's modulus and strength. Both individual numerical results and corresponding mean and standard deviation values are respectively shown, as well as the associated linear ($R^2_{\text{lin}} = 0.994$) and rational ($R^2_{\text{rat}} = 0.991$) fits.

Figure 12: Numerical results showing the effect of the initial fibre misalignment on the longitudinal compressive response.

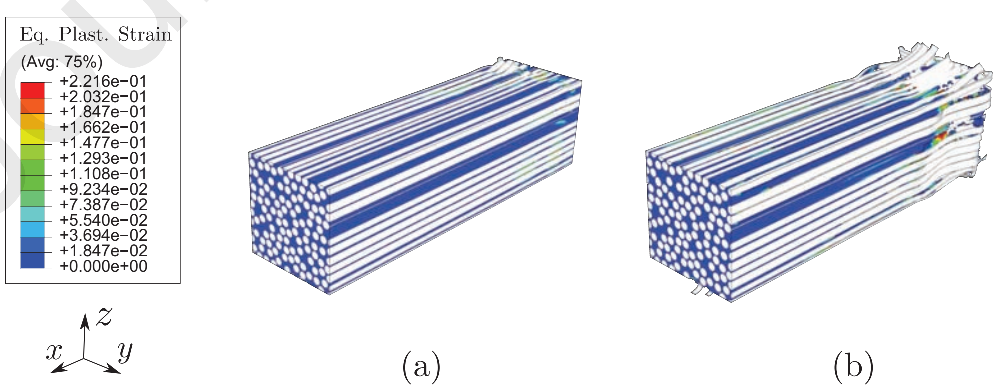

Figure 13: Contour plots of the equivalent plastic strain of an RVE with $\kappa = \infty$, showing the localisation of damage at one of the boundaries of the RVE, when submitted to longitudinal compression, just (a) before and (b) after peak load.

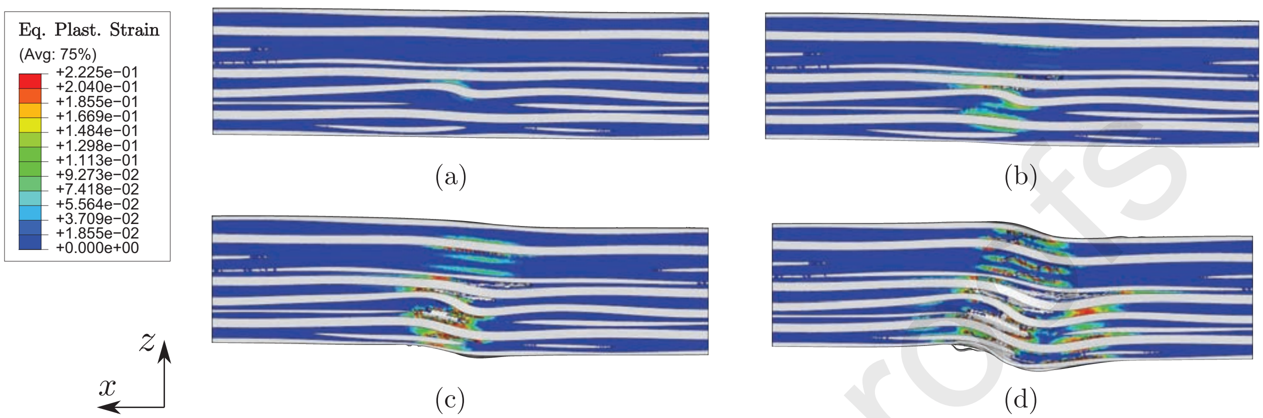

Figure 14: Deformed configuration of an RVE with $\kappa = 1500$, highlighting the contour plots of the equivalent plastic strain at different stages of the damage process in longitudinal compression: (a) non-linearities in the most misaligned region; (b) damage propagation along this region; (c) severe damage propagation along the height of the RVE before peak load; (d) fracture of the material after peak load.

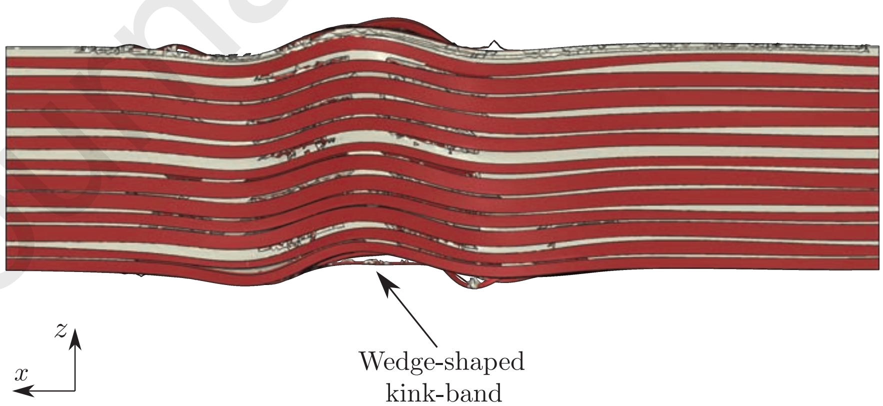

Figure 15: Deformed configuration of an RVE with $\kappa = 8000$, just after peak load, exhibiting a wedge-shaped kink-band.

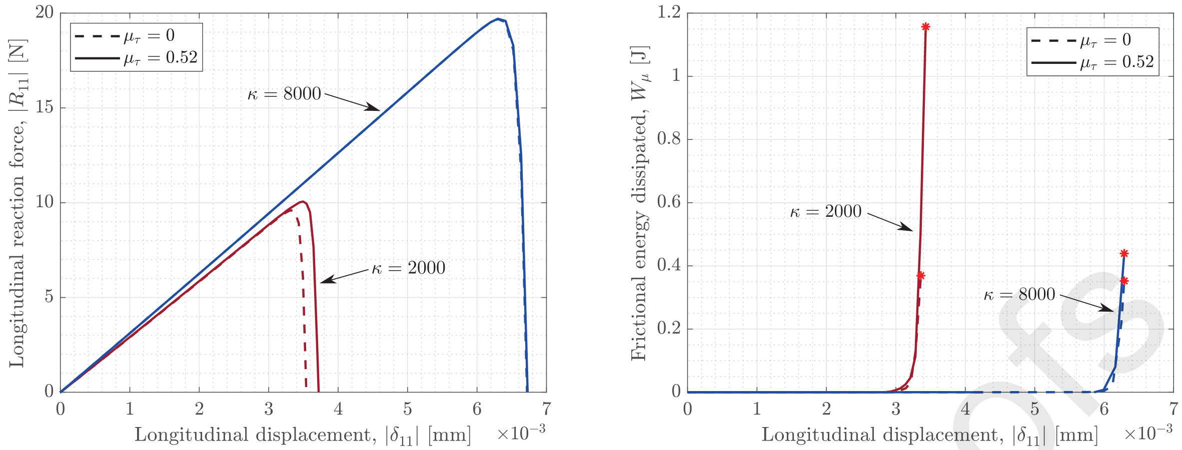

(a) Reaction force vs. displacement.

(b) Frictional energy dissipated vs. displacement.

Figure 16: Numerical assessment of the influence of friction between constituents considering two degrees of misalignment in longitudinal compression. The red points indicate peak load.

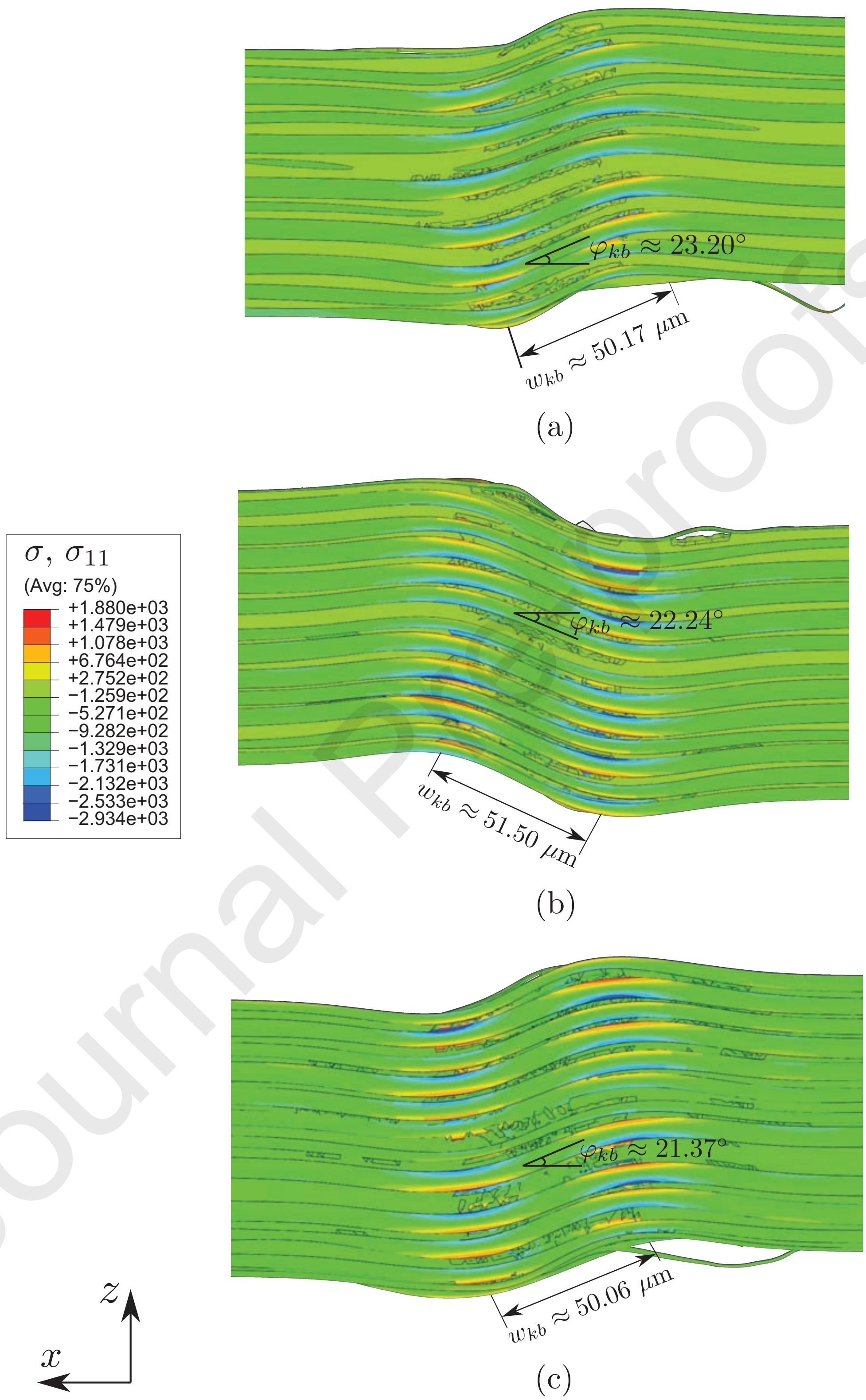

Figure 17: Contour plots of the local longitudinal stress along the kink-band, highlighting the fibre rotation angle of the fibres and kink-band width, associated with RVEs having: (a) $\kappa = 2000$; (b) $\kappa = 4000$; and (c) $\kappa = 6000$ (only the kink-band region is shown).

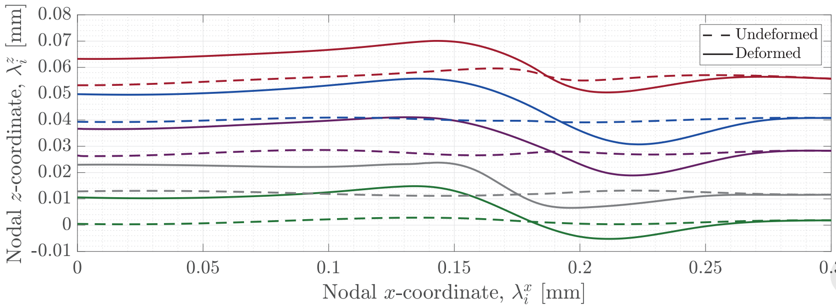

Figure 18: Bi-dimensional (x and z) central spatial coordinates of different fibres, with different degrees of misalignment, of the same RVE ($\kappa = 2000$), having an undeformed (dashed lines) and deformed (solid lines) configurations at peak load.

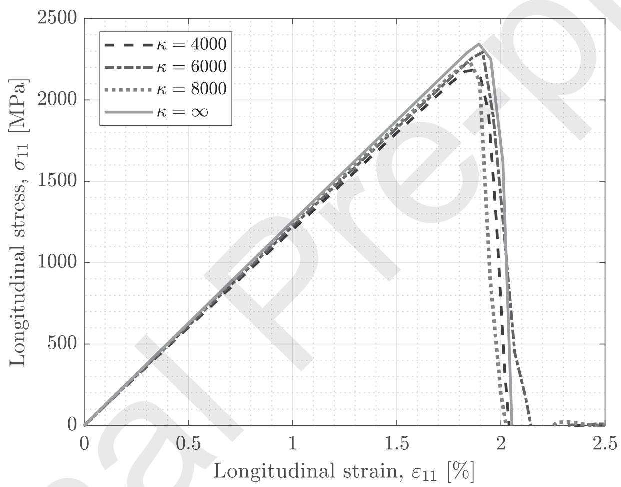

(a)

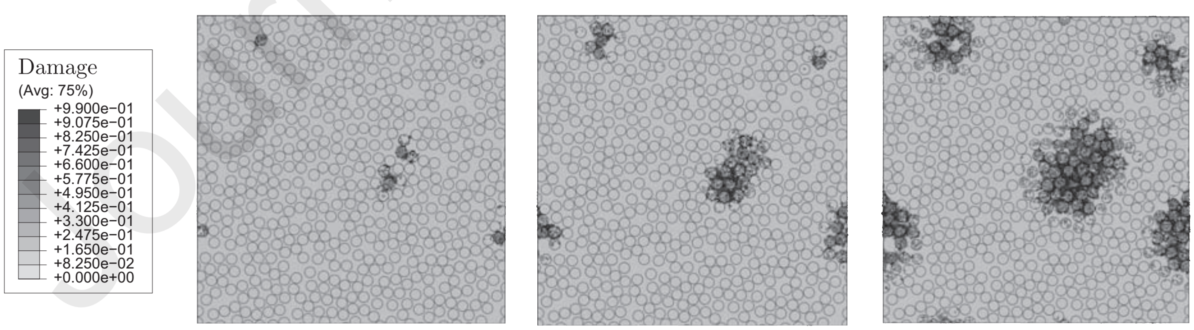

1) 2) 3)

(b)

Figure 19: (a) Longitudinal tensile stress-strain curves of four RVEs having different distributions of the initial fibre misalignment, κ; (b) corresponding contour plots of the matrix and fibres damage variable, at different stages of the damage process, for an RVE with $\kappa = 6000$.

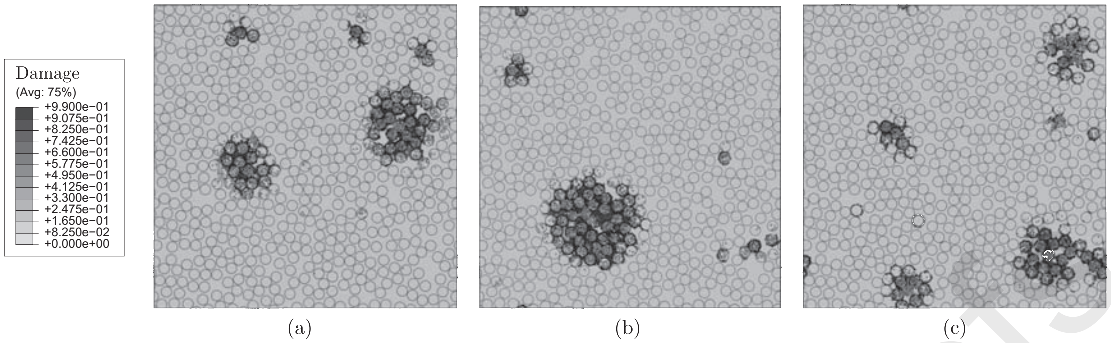

Figure 20: Contour plots of both matrix and fibres damage variable for an RVE with $\kappa = \infty$, at different longitudinal sections: (a) $\Delta_x/L_x = 0.31$; (b) $\Delta_x/L_x = 0.53$; and (c) $\Delta_x/L_x = 0.78$.

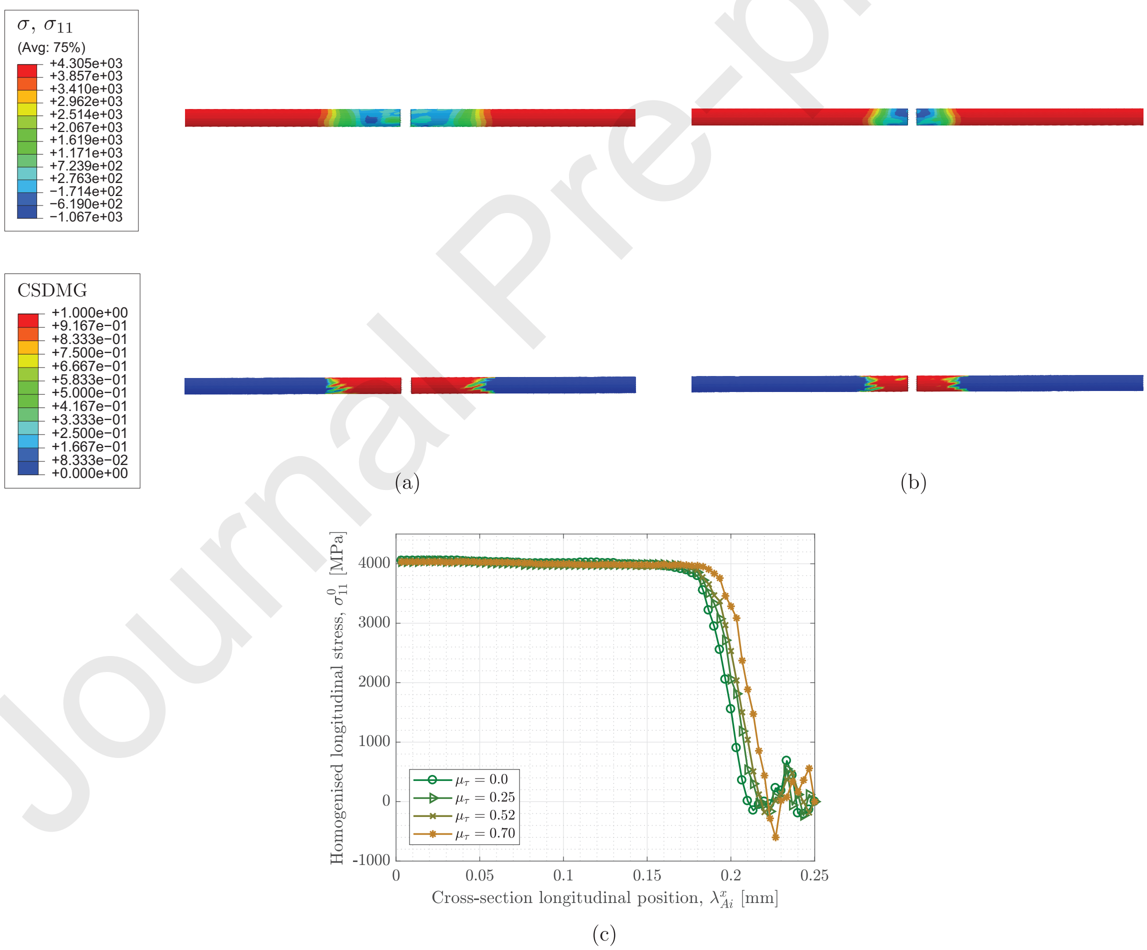

Figure 21: (a) and (b) Contour plots of the longitudinal stress (σ_{11}) and fibre-matrix interface damage (CSDMG) along a single fibre inside an RVE, considering $\mu_\tau = 0$ and $\mu_\tau = 0.70$, respectively; (c) numerical results of the distribution of the longitudinal stress along a single fibre inside an RVE with $\kappa = \infty$, for different μ_τ (the results associated with only half a fibre are shown).

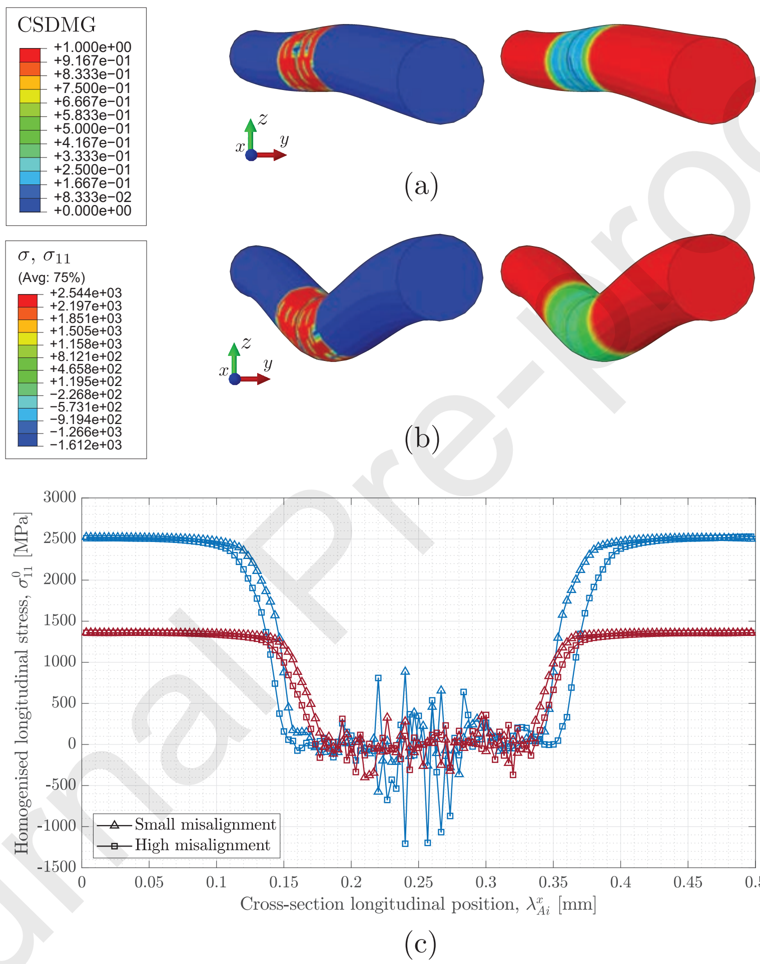

Figure 22: (a) and (b) Contour plots of the fibre-matrix interface damage (left - CSDMG) and longitudinal stress (right - σ_{11} in MPa), exhibiting the debond length, for a fibre having, qualitatively, a "Small" and a "High" degree of misalignment, respectively; (c) numerical predictions of the volumetrically homogenised longitudinal stress along each fibre having different degrees of misalignment (red lines - $\varepsilon_f^0 = 0.6\%$; blue lines - $\varepsilon_f^0 = 1.1\%$).

Table 1: AS4 carbon fibre material properties (Soden et al., 1998, Bai et al., 2015, Herráez et al., 2016, Tavares et al., 2016).

Material property	Value
Fibre diameter	
$2R_f$ [mm]	0.006
Fibre volume fraction	
ω_f [%]	55.9
Young's moduli	
E_{11}^f [MPa]	225000
E_{22}^f [MPa]	15000
Poisson's ratio	
ν_{12}^f [-]	0.2
Shear moduli	
G_{12}^f [MPa]	15000
G_{23}^f [MPa]	7000
Mode I fracture toughness	
$\mathcal{G}_{Ic}^f$ [N/mm]	0.05
Weibull parameters	
σ_0 [MPa]	4275
m_0 [-]	10.7
L_0 [mm]	12.7
Density	
ρ_f [kg/mm^3]	1.78×10^{-6}

Table 2: Matrix material properties (Melro et al., 2013b, Arteiro et al., 2014, 2015).

Material property	Value
Young's modulus	
E_m [MPa]	3760
Poisson's ratio	
ν_m [-]	0.39
Plastic Poisson's ratio	
ν_m^p [-]	0.3
Tensile strength	
X_m^t [MPa]	93
Compressive strength	
X_m^c [MPa]	180
Mode I fracture toughness	
$\mathcal{G}_{Ic}^m$ [N/mm]	0.277
Density	
ρ_m [kg/mm^3]	1.3×10^{-6}

Table 3: Fibre-matrix interface properties (Melro et al., 2013b, Arteiro et al., 2014, 2015).

Material property	Value
Interface stiffness	
K [N/mm^3]	10^8
Interface strengths	
τ_1^0 [MPa]	75
τ_2^0 [MPa]	75
τ_3^0 [MPa]	50
Interface fracture toughnesses	
$\mathcal{G}_{Ic}$ [N/mm]	0.002
$\mathcal{G}_{IIc}$ [N/mm]	0.006
$\mathcal{G}_{IIIc}$ [N/mm]	0.006
Mixed-mode interaction parameter	
η_{BK} [-]	1.45
Friction coefficient	
μ_τ [-]	0.52

Table 4: Size of the RVE vs. normalised numerical predictions of the peak stress.

In-plane dimension, H [μm]	Number of fibres, n_f [#]	Normalised peak stress, $\frac{\sigma_{11}^{cu}}{\sigma_{11}^{max}}$ [%]
$5R_f = 15$	4	77.7
$10R_f = 30$	16	82.5
$15R_f = 45$	36	86.8
$20R_f = 60$	64	90.4
$25R_f = 75$	120	99.2
$30R_f = 90$	168	100.0

Table 5: Quantitative results for different mesh densities.

Element size [μm]	N. of elements [#M]	Normalised peak stress, $\frac{\sigma_{11}^{cu}}{\sigma_{11}^{max}}$ [%]	Computational time, C [h]
$\approx R_f/2$	≈ 1.1	51.2	108.5
$\approx R_f/3$	≈ 3.4	75.5	140.0
$\approx R_f/4$	≈ 6.0	94.4	191.8
$\approx R_f/5$	≈ 7.2	99.4	243.9
$\approx R_f/6$	≈ 9.4	100.0	317.4

Table 6: Numerical predictions of the mean compressive Young's modulus, E_{11}^c, mean peak stresses, σ_{11}^{cu}, and their corresponding standard deviations, for different von Mises concentration parameters, κ.

	$\kappa = 1500$	$\kappa = 2000$	$\kappa = 3000$	$\kappa = 4000$	$\kappa = 6000$	$\kappa = 8000$	$\kappa = \infty$
E_{11}^c [GPa]	$111.5^{\pm 0.3}$	$115.6^{\pm 0.3}$	$118.4^{\pm 0.7}$	$119.8^{\pm 0.6}$	$122.2^{\pm 0.3}$	$123.2^{\pm 0.2}$	$125.1^{\pm 0.1}$
σ_{11}^{cu} [MPa]	$1785^{\pm 133.38}$	$1907^{\pm 120.19}$	$2148^{\pm 86.5}$	$2589^{\pm 167.6}$	$3048^{\pm 103.0}$	$3561^{\pm 53.3}$	$5114^{\pm 122.7}$

Table 7: Mean estimated results associated with the kink-band width, w_{kb}, fibre rotation angle, φ_{kb}, and their corresponding standard deviations, for different von Mises concentration parameters, κ.

	$\kappa = 1500$	$\kappa = 2000$	$\kappa = 3000$	$\kappa = 4000$	$\kappa = 6000$	$\kappa = 8000$
w_{kb} [μm]	$50.17^{\pm 0.88}$	$50.69^{\pm 1.62}$	$49.43^{\pm 1.11}$	$52.77^{\pm 3.47}$	$49.88^{\pm 2.83}$	$51.89^{\pm 3.31}$
φ_{kb} [°]	$23.87^{\pm 0.49}$	$23.44^{\pm 0.57}$	$23.19^{\pm 0.50}$	$22.44^{\pm 0.47}$	$21.91^{\pm 0.31}$	$20.73^{\pm 0.18}$

Micromechanical modelling of the longitudinal compressive and tensile failure of unidirectional composites: The effect of fibre misalignment introduced via a stochastic process

L.F. Varandas[a], G. Catalanotti[a,*], A.R. Melro[b], R.P. Tavares[c,d], B.G. Falzon[a]

[a]Advanced Composites Research Group (ACRG), School of Mechanical and Aerospace Engineering, Queen's University Belfast, Belfast BT9 5AH, UK
[b]Bristol Composites Institute (ACCIS), University of Bristol, Bristol BS8 1TR, UK
[c]DEMec, Faculdade de Engenharia, Universidade do Porto, Rua Dr. Roberto Frias, 4200-465, Porto, Portugal
[d]INEGI, Rua Dr. Roberto Frias, 400, 4200-465 Porto, Portugal

Abstract

Initial fibre misalignment is recognised to be one of the precursors leading to longitudinal compressive failure in fibre-reinforced composites. Thus, to properly model their mechanical behaviour, an accurate spatial representation of the fibrous reinforcements must be assured. This work presents a three-dimensional micromechanical framework that is capable of analysing in detail the longitudinal tensile and compressive failure mechanisms which are inherent in unidirectional composites. This is achieved through the incorporation of initial fibre waviness via a combination of a stochastic process and an optimisation procedure. A robust micro-scale framework is developed by assigning, to both constituents and their interface, proper thermodynamically consistent damage models. Several microstructures having different degrees of misalignment are modelled and a clear trend is observed for the longitudinal compressive load case, i.e. by increasing initial fibre misalignment, the overall performance of the material decreases. In contrast, the models subjected to longitudinal tension exhibit a similar overall response, despite the misalignment. However, local mechanisms seem to change with the degree of friction and fibre misalignment, but these smaller-scale mechanisms do not play a decisive role on the overall longitudinal tensile performance of the material.

Keywords: Composite materials, Fibre misalignment, Fracture, Micromechanics, Stochastic

1. Introduction

As a direct consequence of increasing computational power, in the last decade, computational micromechanics has emerged as an accurate and reliable numerical tool to evaluate both linear and non-linear geometrical and material behaviour of heterogenous materials. Unlike analytical/semi-analytical methods, the several complex dissipative phenomena, including local plastic deformation and degradation of the matrix constituent, fibre-matrix interface debonding, and fibre fracture, are accounted for and their interaction can be evaluated.

*Corresponding author
Email address: G.Catalanotti@qub.ac.uk (G. Catalanotti)

Compressive failure of composite materials caused by fibre kinking is classified as a complex, multi-staged phenomenon, due to the interacting mechanisms and instabilities present at peak load, which span over several length-scales of the material (Argon, 1972, Budiansky, 1983, Budiansky, Fleck, 1993, 1994, Moran et al., 1995, Jumahat et al., 2010, Costa et al., 2020). There is compelling evidence that this mode of failure is mostly driven by not only the initial misalignment of the fibres, but also by the shear yield strength of the matrix (Moran et al., 1995, Bažant et al., 1999, Vogler et al., 2001, Gutkin et al., 2010b, Pinho et al., 2012). The material is loaded elastically until the first appearance of non-linearity, which is due to the initial rotation of the fibres, permitted by the plastic response of the matrix. This is also known as "incipient kinking" (Moran et al., 1995). Due to this rotation and to the formation of microcracks in the resin, the peak load (instability) is reached, forming an initial kink-band. The progressive shearing/bending stresses in the material causes its continuous degradation, until this fibre rotation is halted, through a process referred as fibre lock-up, which eventually leads to the steady-state broadening of the kink-band, causing a constant stress plateau under compression, referred as the residual compressive strength of the material (Moran et al., 1995, Zobeiry et al., 2015, Dalli et al., 2020). Kink-bands are characterised by an angle, β_{kb}, with respect to the through-thickness direction (normal to the load), a certain width, w_{kb}, having the fibres rotated from an angle, φ_{kb}, to the global longitudinal direction. Figure 1 shows a micrograph of a formed kink-band in an UD cross-ply laminate, as well as a schematic representation of a longitudinal compressive stress-strain curve, highlighting the main load level stages.

[Figure 1 about here.]

Several computational micromechanical models have been reported, in an attempt to model longitudinal compressive failure in UD composite materials by fibre kinking. Initial insights were provided using two-dimensional (2D) models, namely on the types of failure mechanisms associated with compressive failure (Gutkin et al., 2010a), the interaction between fibre kinking and fibre-matrix interface debonding (Prabhakar, Waas, 2013), and on the estimation of the kink-band angle and compressive strength of the material (Kyriakides et al., 1995, Vogler et al., 2001). The limitations of 2D models were addressed by Hsu et al. (1998), where a bigger degree of discrepancy between 2D and three-dimensional (3D) models was observed in the post-peak regime. Fortunately, modern computational resources have enabled the generation of 3D high-fidelity numerical models. Yerramalli, Waas (2004) conducted 3D Finite Element (FE) analyses to show the importance of fibre bending stiffness on the overall compressive strength of the material, as well as the presence of a complex triaxial stress state in the matrix region. Later, Bai et al. (2015), incorporating a more robust elasto-plastic damage model for the resin (Melro et al., 2013a), subjected different Representative Volume Elements (RVEs) to several loading conditions, i.e. transverse on- and off-axis compression, and pure longitudinal compression. They were able to obtain some preliminary results concerning kink-band widths and fibre rotation angles, concluding that the interplay between the shear stresses, presented in the matrix material, and microbuckling, caused by the initial, idealised fibre misalignment, provides a sound explanation to the fibre kinking failure mode. Bishara et al. (2017) conducted simpler micromechanical simulations, considering a single array of fibres, in order to assess the influence of the artificial imperfection type on the resulting kinking mechanism, the effective determination of the kink-band angle, and the effect of different fibre strengths on the kink-band angle. Recent studies using a sinusoidal swept single fibre model, subjected to Periodic Boundary Conditions (PBCs), were undertaken (Naya et al., 2017, Herráez et al., 2018, 2020) to give more insight into the effect of the initial fibre misalignment angle on the kink-band width and fibre rotation angles, by comparing the results with well known analytical models. As remarked by Hill (1963), an RVE is a medium which characterises the microstructure of the material, being statistically representative of the mixture of constituents. It has a dimension that contains a sufficient number of inclusions/reinforcements, making a single fibre model non-representative of the actual material. Moreover, the application of such PBCs force the kink-band angle to be zero, i.e. $\beta_{kb} = 0$. Finally, the use of the maximum homogenised stress, obtained by using First Order Homogenisation Techniques (FOHT), may not be a proper way to measure the actual strength of the material, since, as strain localisation occurs, the separation of scales (Hashin, 1983) is intrinsically violated, making the solution dependent on both BCs applied and size of the considered medium. For a concise review on the analytical, semi-analytical, and numerical methodologies which treat longitudinal compressive failure in fibre-reinforced composites, addressing both phenomenology and failure mechanisms involved, the reader is referred to Daum et al. (2019).

Modelling fibre-dominated damage, in UD composites, is a complex task due to the acting damage mechanisms which arise when submitted to a longitudinal tensile loading scenario. There are several important factors when modelling the longitudinal tensile behaviour of a composite, namely: i) capture the formation of fibre break clusters, which later leads to the unstable final failure of the material (Scott et al., 2011, 2012, Thionnet et al., 2014); ii) capture the stochastic nature of the tensile strength of carbon fibres (Lamon, 2007, Tanaka et al., 2014, Torres et al., 2017); iii) capture the complete ineffective and debond length of a broken fibre; and iv) treat fibre fracture as a dynamic event, where the internal strain energy released by the reinforcements is converted into kinetic energy (Swolfs et al., 2015a, Tavares et al., 2019b). Figure 2 shows a computed tomography (CT) image of a cross-ply laminate, which failed under longitudinal tension, highlighting the pulled-out 0° fibres and the corresponding perpendicular fracture plane (Laffan et al., 2010), and a synchrotron radiation computed tomography (SRCT) image of disperse and co-planar clusters of broken fibres (Swolfs et al., 2015a).

[Figure 2 about here.]

There are several models which are available in literature that are capable of estimating the longitudinal tensile strength of UD carbon fibre-reinforced composite materials, hybridised or not, being able to tackle most (if not all) of the aforementioned features governing longitudinal tensile failure (Swolfs et al., 2015c,b, 2016, Tavares et al., 2016, 2017, St-Pierre et al., 2017, Guerrero et al., 2018, Tavares et al., 2019b). These often rely on simpler micromechanical models, where fibre fracture is taken into account using maximum stress criteria. In contrast, the work of Tavares et al. (2016) reports the usage and implementation of thermodynamically consistent damage models, providing enough detail to capture the micro-scale failure mechanisms which govern longitudinal tensile failure.

Most of the aforementioned micromechanical models make reference to an implicitly assumed, constant in space, initial fibre misalignment, making such predictions unsuitable for real case scenarios, since to empirically quantify fibre misalignment, a statistically representative parameter is needed. Variable, spatially distributed fibre waviness, has long been recognised as an important consideration, and investigations into the stochastic properties of its magnitude and distribution have been reported (Hillig, 1994, Clarke et al., 1995, Creighton et al., 2001, Requena et al., 2009, Sutcliffe et al., 2012, Pain, Drinkwater, 2013, Mizukami et al., 2016, Wilhelmsson, Asp, 2018). Recently, Sebaey et al. (2019) developed an integrated approach to statistically represent fibre misalignment at the scale of the constituents, where the deviations in fibre angles and corresponding footprints are first determined using CT scans, and then the data is statistically fitted following a von Mises distribution, characterised by the corresponding concentration parameter. A post-study conducted by Catalanotti, Sebaey (2019) involved the proposal of a semi-stochastic algorithm where initial fibre misalignment is taken into account by combining the stochastic process and an optimisation procedure.

Here, a 3D FE micromechanical framework is built to analyse in detail, the longitudinal failure of composite materials. To describe the non-linear behaviour of the constituents and their interface, appropriate constitutive material models are implemented along with an algorithm for the generation of high-fidelity RVEs, accounting for a stochastic-based fibre misalignment. To the authors' knowledge, this is the first time that a numerical micromechanical framework is built together, to investigate the effect of a stochastic-based initial fibre waviness on the longitudinal failure of unidirectional carbon fibre-reinforced composite materials. Additional analyses are undertaken to investigate the effect of considering frictional cohesive surfaces on the damage tolerance of the composite.

2. Computational framework

The developed 3D FE micromechanical framework is composed of detailed micromechanical representations of the material, henceforth described as RVEs, having different degrees of fibre misalignment and the same fibre volume fraction, ω_f. For brevity, only pertinent aspects of the RVE generation and the constitutive material models used, are presented, where several important considerations are discussed.

2.1. Generation of the RVEs

The generation of the RVEs involves the measurement of the angle between the projection of the tangent vector of the fibres and a given direction (Catalanotti, Sebaey, 2019). Figure 3 shows the three spatial descriptors, which the algorithm makes use of, that characterise fibre misalignment, where x, y, and z represent the longitudinal, transverse, and through-thickness directions of a typical UD lamina, respectively, and $\vec{i}$, $\vec{j}$, and $\vec{k}$ the unit vectors in each corresponding direction.

[Figure 3 about here.]

The three spatial descriptors, shown in Figure 3, are the three misalignment angles, which are defined as: ϕ_{yx}, the angle between $\vec{i}$ and the projection of the tangent vector to the fibre, $\vec{\nu}$, onto the O_{xz} plane; ϕ_{zx}, the angle between $\vec{i}$ and the projection of the tangent vector to the fibre, $\vec{\nu}$, onto the O_{xy} plane; and α_{xy}, the angle between $\vec{j}$ and the the projection of the tangent vector to the fibre, $\vec{\nu}$, onto the O_{yz} plane (Catalanotti, Sebaey, 2019). Both in-plane and out-of-plane misalignment angles, ϕ_{yx} and ϕ_{zx}, respectively, are of importance when conducting RVE-based numerical simulations, and may be experimentally characterised using appropriate experimental techniques (Sutcliffe et al., 2012, Sebaey et al., 2019). However, there is no relevance on characterising the remaining misalignment angle, α_{xy}, since, in principle, it does not have any practical importance when submitting the RVEs to the stress states mentioned in this work.

For introducing the waviness of the fibres via a stochastic process, the fibres are modelled as Bézier curves, whose initial control points are determined by using a 2D fibre distribution algorithm (Catalanotti, 2016). These control points can then be moved in a random fashion, for a desired number of times, in a plane perpendicular to $\vec{i}$, creating the 3D geometrical variability, i.e. fibre waviness. Periodicity of the virtual microstructure is also achieved by computing the proper distance between the control points of different fibres and assuring continuity between the first and last control point of the same fibre, when translated in the longitudinal direction by the length of the RVE (Catalanotti, Sebaey, 2019). The radial coordinates are chosen in order to ensure that the distribution of the misalignment angles match the empirical/theoretical ones (Sebaey et al., 2019). It was assumed the distribution follows the general von Mises distribution, whose probability density function (pdf) reads:

$$\mathrm{g}(\phi, \mu, \kappa) = \frac{1}{2\pi I_0(\kappa)} \mathrm{e}^{\kappa \cos(\phi) - \mu}, \tag{1}$$

where ϕ is equal either to the in-plane or out-of-plane misalignment angle, μ is the mean direction, κ is the concentration parameter, and I_0 is the modified Bessel function of the first kind and order 0. Since the mean direction represents the longitudinal (x-direction) direction of the composite, μ is assumed to be equal to 0, and therefore the concentration parameter, κ, is the only variable which characterises the distribution. By minimising the standard errors (likelihood and probability), it is possible to achieve a remarkable match between the experimental/theoretical and numerical distributions. Figure 4 shows an example of the pdf of theoretical and numerical distributions, the Q-Q plot, and the associated front and isometric views of a generated RVE with $\kappa = 2000$.

[Figure 4 about here.]

For modelling perfectly aligned fibres, κ is equal to ∞, and for modelling very wavy fibres, κ takes a small value, e.g. $\kappa = 500$. For a complete description of the algorithm used to generate 3D RVEs incorporating fibre waviness, the reader is referred to Catalanotti, Sebaey (2019).

2.2. Constitutive material models

2.2.1. Carbon fibres

The carbon fibres are modelled as transversely isotropic and considered to behave linear-elastically up to failure. Degradation of the stiffnesses of the material is defined by implementing a thermodynamically consistent isotropic damage model, which is only activated by the longitudinal stress component. The damage activation function is given as:

$$F_f^d = \phi_f^d - r_f = \frac{\tilde{\sigma}_{11}}{X_f^t} - r_f, \tag{2}$$

where ϕ_f^d is the loading function, $\tilde{\sigma}_{11}$ is the undamaged longitudinal applied stress, X_f^t is the longitudinal tensile strength of the fibre, and r_f is an internal variable related to the damage evolution law of the fibre, d_f. As discussed by several authors (Swolfs et al., 2015c,b, Tavares et al., 2016, Swolfs et al., 2016, Tavares et al., 2017), the tensile strength of the carbon fibres has an intrinsic stochastic nature, mostly due to the flaws which are present on the surface of the fibres (Lamon, 2007, Tanaka et al., 2014, Torres et al., 2017), which needs to be taken into account. Here, these are accounted for through the Weibull distribution (Weibull, 1951):

$$P(\sigma) = 1 - \exp\left[-\left(\frac{L}{L_0}\right)\left(\frac{\sigma}{\sigma_0}\right)^{m_0}\right], \tag{3}$$

where P represents the failure probability at the applied stress σ, σ_0 and m_0 are the Weibull strength and parameter, respectively, and L_0 and L are the reference and gauge length, respectively. Modifying equation (3) and generating a random scalar in the interval $]0,1[$, $\mathscr{X}$, that represents the failure probability, the tensile strength can be estimated following:

$$X_f^t = \sigma_0 \left[-\frac{L_0}{L}\ln(1-\mathscr{X})\right]^{1/m_0}. \tag{4}$$

The Weibull distribution is probably the most used statistical distribution for fibre strength. However, it has been shown that it is not the best suited for carbon and glass fibres (Gulino, Phoenix, 1991, Beyerlein, Phoenix, 1996, Curtin, 2000), leading to an overprediction in both tensile strength and failure strain (Tavares et al., 2017). The correct definition of the proper fibre tensile strength distribution is out of the scope of the current work, thus the Weibull distribution is used due to its simplicity in implementation.

To avoid damage localisation and to control the energy dissipated in the fracture process, Bažant and Oh's *crack band model* (Bažant, Oh, 1983) is implemented to regularise the computed dissipated energy:

$$\Psi_f = \int_1^\infty \frac{\partial \mathscr{G}_f}{\partial d_f}\frac{\partial d_f}{\partial r_f}\mathrm{d}r_f = \frac{\mathcal{G}_{Ic}^f}{l_f^e}, \tag{5}$$

where $\mathscr{G}_f$ is the complementary free energy density of the fibrous material, $\mathcal{G}_{Ic}^f$ is the mode I fracture toughness of the fibres, and l_f^e represents the characteristic element length.

The damage evolution law for the fibres is given by:

$$d_f = 1 - \frac{e^{A_f(1-r_f)}}{r_f}, \tag{6}$$

where A_f is a mesh regularisation parameter which conveys the numerical model with mesh size independency (Bažant, Oh, 1983) and must be computed for each finite element by solving equation (5).

The mechanical properties of the AS4 fibres considered here are shown in Table 1 and were taken from Soden et al. (1998), Bai et al. (2015), Herráez et al. (2016), Tavares et al. (2016).

[Table 1 about here.]

For more details on the damage model, the reader is referred to Tavares et al. (2016).

2.2.2. Epoxy matrix

Previous studies (Ghorbel, 2008) have shown that both the Drucker-Prager and Mohr-Coulomb constitutive material models are not able to properly model the representative behaviour of an epoxy resin, namely under the presence of triaxial stress states. A more representative elasto-plastic material model, proposed by Melro et al. (2013a), is used here to simulate the behaviour of the matrix constituent.

The model assumes that the matrix behaves in a linear-elastic fashion until the following paraboloidal yield criterion, originally proposed by Tschoegl (1971), is met:

$$\Phi(\boldsymbol{\sigma}, \varepsilon_e^p) = 6J_2 + 2(\sigma_{Y_c}^m - \sigma_{Y_t}^m)I_1 - 2\sigma_{Y_c}^m \sigma_{Y_t}^m, \tag{7}$$

where $\sigma_{Y_t}^m$ and $\sigma_{Y_c}^m$ are the absolute values of the tensile and compressive yield strengths, $I_1 = \mathrm{tr}(\boldsymbol{\sigma})$ is the first invariant of the stress tensor and $J_2 = \frac{1}{2}\boldsymbol{s} : \boldsymbol{s}$ is the second deviatoric stress tensor ($\boldsymbol{s}$) invariant. In order to correctly define the plastic deformation under the presence of a hydrostatic pressure, a non-associative flow rule is defined. Both tensile and compressive yield strengths depend on the equivalent plastic strain, ε_e^p:

$$\varepsilon_e^p = \sqrt{\frac{1}{1 + 2{\nu_m^p}^2} \varepsilon^p : \varepsilon^p}, \tag{8}$$

where ν_m^p is the plastic Poisson's ratio of the matrix.

The yield surface presented in equation (7) depends only on the tensile ($\sigma_{Y_t}^m$) and compressive ($\sigma_{Y_c}^m$) yield strengths which are both affected by hardening:

$$\sigma_{Y_t}^m = \sigma_{Y_t}^m(\varepsilon_e^p), \qquad \sigma_{Y_c}^m = \sigma_{Y_c}^m(\varepsilon_e^p). \tag{9}$$

Figure 5 shows the hardening curves used in the plasticity model in both tension and compression.

[Figure 5 about here.]

Damage is defined by using a model developed within the framework of thermodynamically admissible processes. Initiation of damage is computed with the following failure criterion (Melro et al., 2013a):

$$F_m^d = \phi_m^d - r_m = \frac{3\tilde{J}_2}{X_m^c X_m^t} + \frac{\tilde{I}_1(X_m^c - X_m^t)}{X_m^c X_m^t} - r_m, \quad (10)$$

where ϕ_m^d is the loading function, X_m^c and X_m^t represent the compressive and tensile strengths of the material, respectively, and r_m is an internal variable related to the matrix damage variable. Both invariants ($\tilde{J}_2$ and $\tilde{I}_1$) are determined using the effective stress tensor, i.e. the stress tensor calculated using the undamaged stiffness tensor. The damage variable is given by:

$$d_m = 1 - \frac{e^{A_m(3-\sqrt{7+2r_m^2})}}{\sqrt{7+2r_m^2}-2}, \quad (11)$$

where A_m is a parameter that must be computed for each element of the finite element mesh of the matrix material. To avoid mesh size dependency problems, Bažant and Oh's *crack band model* (Bažant, Oh, 1983) was also implemented, making use of the mode I fracture toughness of the epoxy, $\mathcal{G}_{Ic}^m$ and corresponding characteristic element length, l_m^e, to regularise the computed dissipated energy (Bažant, Oh, 1983):

$$\Psi_m = \int_1^\infty \frac{\partial \mathscr{G}_m}{\partial d_m}\frac{\partial d_m}{\partial r_m}\mathrm{d}r_m = \frac{\mathcal{G}_{Ic}^m}{l_m^e}, \quad (12)$$

where $\mathscr{G}_m$ is the complementary free energy density of the matrix material.

Table 2 shows the mechanical properties used to model the epoxy. For more information regarding the constitutive material model, the reader is referred to Melro et al. (2013a).

[Table 2 about here.]

This material constitutive model has exhibited promising results when modelling the behaviour of epoxy resins under a variety of loading conditions (Melro et al., 2013b, Arteiro et al., 2014, 2015, Tavares et al., 2016, Varandas et al., 2017, 2019, Sun et al., 2019b, Arteiro et al., 2019, Chen et al., 2019, Meer van der et al., 2019, Dalli et al., 2019, Varandas et al., 2020a,b, Dalli et al., 2020).

2.2.3. Fibre-matrix interface

Due to the intricate mesh required for these RVEs, the interfaces between fibres and matrix were modelled using cohesive surfaces, rather than cohesive elements, as it does not require mesh compatibility between the two constituents. A Mohr-Coulomb friction condition has also been considered for post-failure of the cohesive bond between the two constituents. Once the cohesive stiffness starts degrading, friction starts contributing to the shear stresses. This feature will capture the pull-out resistance between fibre and matrix caused mostly by the rough failure surface on the fibre, after interfacial failure, and it is governed by the friction coefficient, μ_τ.

Initiation of fibre-matrix interface damage is predicted using a stress-based quadratic failure criterion (Lin Ye, 1988):

$$\phi_{int}^{d} = \left(\frac{\langle\tau_3\rangle}{\tau_3^0}\right)^2 + \left(\frac{\tau_2}{\tau_2^0}\right)^2 + \left(\frac{\tau_1}{\tau_1^0}\right)^2, \tag{13}$$

where τ_1, τ_2, and τ_3 represent the components of traction and τ_1^0, τ_2^0, and τ_3^0 are the corresponding interface strengths. A bi-linear traction-separation behaviour is assumed, and the fibre-matrix interface damage variable is computed as (Aba, 2018):

$$d_{int} = \frac{\delta_{int}^{f}(\delta_{int}^{\max} - \delta_{int}^{0})}{\delta_{int}^{\max}(\delta_{int}^{f} - \delta_{int}^{0})}, \tag{14}$$

where, $\delta_{int}^{f} = 2\mathcal{G}_c^{int}/\tau_{\text{eff}}^0$, with $\mathcal{G}_c^{int}$ as the mixed-mode fracture toughness (Benzeggagh, Kenane, 1996) and τ_{eff}^0 as the effective traction at damage initiation. $\delta_{int}^{\max}$ refers to the maximum value of the effective displacement attained during loading history and δ_{int}^{0} is the displacement at damage initiation. Table 3 shows the properties used to model the interfaces.

[Table 3 about here.]

2.3. Finite element modelling

Several RVEs having different concentration parameters, κ, are considered (see equation (1)). As remarked by Hill (1963), an important aspect in RVE-based modelling, is the size of the RVE and boundary conditions (BCs) imposed. The applied BCs should affect the overall mechanical performance of the material, namely during softening, existing an interplay between the BCs and size of the RVE (Triantafyllidis, Bardenhagen, 1996, Gitman et al., 2007, Galli et al., 2008). Since Periodic Boundary Conditions (PBCs) yield an enormous computational cost, as well as, in longitudinal compression, they constrain the kink-band angle *a priori* (Gutkin et al., 2010a), standard BCs are used, where direct constraints are applied to the boundaries of the RVEs. Moreover, by considering a sufficiently large FE model, edge and face effects can be neglected (Kanit et al., 2003, Stroeven et al., 2004, Gitman et al., 2006, Sun et al., 2019b). With reference to Figure 6, the following BCs are applied for each loading condition (Hsu et al., 1998, Vogler et al., 2001, Tavares et al., 2016, Bishara et al., 2017):

- Longitudinal compression - The longitudinal (x-direction) and through-thickness (z-direction) axial displacements of face 1 are fixed. *Tie Constraints* are applied between Face 3 and Face 4. A longitudinal (x-direction) compressive velocity-type BC is applied to face 2. Faces 5 and 6 are free to deform.
- Longitudinal tension - The longitudinal axial (x-direction) displacements are fixed on Face 1 and a longitudinal (x-direction) tensile velocity-type BC is applied to Face 2. All other faces are free to deform to account for Poisson's contraction.

The dimension of the RVEs in the longitudinal direction (x-direction) is denoted by L_x, and the in-plane dimensions (y- and z-directions) by H (see Figure 3).

[Figure 6 about here.]

The micromechanical simulations were conducted using the FE solver Abaqus®/Explicit (Aba, 2018). Damaged elements having $d_f > 0.9999 \vee d_m > 0.9999$ (see equations (6) and (11)) were removed throughout the numerical simulations to prevent excessive element distortion. The models ran on one node (20 CPUs @ 3.4 GHz of Intel® Haswell®) having 512 GB of RAM. The *Variable Mass Scaling* capability of Abaqus®/Explicit (Aba, 2018) was used in order to reduce computational cost, by scaling all masses of the elements, to ensure that they all have the same time increment. With that being said, due to the peak load instability and to its kinetic nature, load stages beyond peak load, such as kink-band broadening, could not be captured using the present framework.

Due to its complex geometry, the epoxy matrix material is modelled using C3D4, three-dimensional linear tetrahedrons. The fibres are modelled using C3D8R, reduced integration, linear hexahedrons, combined with C3D6R, reduced integration, linear triangular prisms. The orientation of each element is computed by: (i) obtaining the coordinates of the respective centroid of the ith element, $\boldsymbol{C}_i$=$\{x_i, y_i, z_i\}^T$; (ii) finding the nearest point of the middle line of the associated fibre, i.e. of the associated Bézier curve, to the centroid $\boldsymbol{C}_i$, with coordinates $\boldsymbol{C}_f$=$\{x_f, y_f, z_f\}^T$; and (iii) calculating the unit vector which is tangent to the curve in $\boldsymbol{C}_f$, i.e. $\hat{\boldsymbol{f}}$, and assign it to the orientation of the ith element. Figure 7 shows the longitudinal direction (1-direction) of each element, in a highly misaligned fibre.

[Figure 7 about here.]

3. Numerical results

3.1. Longitudinal compression

This section aims to evaluate the longitudinal compressive failure through fibre kinking. Different RVEs, having random microstructures with several degrees of misalignment were generated following equation (1), with $\kappa = 1500$, $\kappa = 2000$, $\kappa = 3000$, $\kappa = 4000$, $\kappa = 6000$, $\kappa = 8000$, and $\kappa = \infty$. Figure 8 shows the pdf distribution of the misalignment angles for each von Mises concentration parameter considered in this section. Certain outputs related to compressive failure are analysed in detail, making several quantitative and qualitative parallelisms with experimental observations. Moreover, the effect of fibre-matrix interfacial friction is also analysed. It must be noted that it is not feasible to compare these numerical results with analytical/semi-analytical models which estimate the compressive strength of the material, since most of these assume a constant in space initial fibre misalignment angle.

[Figure 8 about here.]

The following two sections present preliminary results assessing the influence of the RVE size and mesh density on the peak stress of the material, as well as global and local features exhibited on a material loaded in longitudinal compression.

3.1.1. Effect of RVE size

Several analyses were conducted to evaluate the influence of the size of the RVE and its mesh size on the overall mechanical performance of the material. Firstly, RVEs with a refined mesh and different dimensions were virtually tested. By considering a constant aspect ratio of the RVE (ratio between the length and in-plane dimensions of the RVE, $A_r = L_x/H$), i.e. $A_r = 4$, the in-plane dimensions considered were 5, 10, 15, 20, 25, and 30 times the radius of a single fibre. Figure 9 and Table 4 show the normalised numerical predictions, with respect to the peak stress associated with the largest RVE. Only one simulation was conducted per size, for $\kappa = 4000$.

[Figure 9 about here.]

[Table 4 about here.]

The results show that when increasing the size of the RVE, the peak load increases as well. Since the smallest RVEs could not accommodate the formation of a kink-band, the material failed prematurely mainly due to interfacial debonding. The results are considered geometrical independent for RVEs with $H \geqslant 25R_f$, where the peak load represented $\approx 99\%$ of the RVE having the largest dimensions. From the concluded above, in-plane dimensions and total length of the RVE of approximately $H = 75$ μm and $L_x = 300$ μm, respectively, are chosen for the forthcoming numerical simulations.

3.1.2. Influence of mesh density

To ensure mesh independent results, FE meshes of different densities were considered, for an FE model with $\kappa = 4000$, and pertinent results are presented in Figure 10 and Table 5.

[Figure 10 about here.]

[Table 5 about here.]

Mesh independence was achieved with models containing over 7 million elements. Therefore, a mesh density with an average value of $R_f/5$ was considered for the forthcoming simulations.

3.1.3. Global mechanical response

Figure 11 shows the numerical results associated with an RVE with $\kappa = 3000$, where a representative stress-strain curve is shown (see Figure 11a) and corresponding contour plots of the equivalent plastic strain of the epoxy matrix (see Figure 11b), associated with three different stages of the non-linear process: (A) initiation of plasticity; (B) just before peak load instability, where the kink-band is almost formed; and (C1) and (C2) complete formation of the kink-band and initiation of the dynamic process.

[Figure 11 about here.]

To assess the effect of the initial fibre misalignment on the longitudinal mechanical performance of the material, it is presented in Figure 12a the representative stress-strain curves for different concentration parameters, κ, all normalised with respect to the results associated with $\kappa = \infty$. Moreover, in Figure 12b and Table 6, the results associated with the effect of the initial fibre misalignment on both overall longitudinal compressive Young's modulus and strength of the material are shown.

[Figure 12 about here.]

[Table 6 about here.]

The normalised stress vs. applied strain curves are presented in Figure 12a (where σ_{11} and ε_{11} represent the longitudinal stress and strain, respectively, and $\sigma^{cu}_{11_\infty}$ represents the compressive peak stress associated with the RVE with $\kappa = \infty$), which shows that both compressive Young's modulus, E^c_{11}, and peak stress, σ^{cu}_{11}, depend on the initial fibre misalignment angle distribution, quantified by κ. As κ increases (less misalignment), both mechanical properties increase. The RVEs having the highest misalignment ($\kappa = 1500$) yielded a peak stress of $\approx 32\%$ that of the idealised RVE having perfectly aligned fibres ($\kappa = \infty$). The decrease in peak stress is explained by the higher initial micro-buckling introduced in several regions of the fibres along the length of the RVEs, causing an earlier degradation of the epoxy matrix and fibre-matrix interface, thus promoting an earlier kinking of the reinforcement. Moreover, for this material system, the quantitative results show that the variation in peak stress with the distribution of the misalignment angles fits better with a rational type of fit ($\sigma^{cu}_{11}(\kappa^{-1}) = (p_1\kappa^{-1} + p_2)/(\kappa^{-1} + q_1)$, where $p_1 = 667.30$, $p_2 = 1.00$ and $q_1 = 1.95 \times 10^{-4}$), and the corresponding coefficient of determination is approximately $R^2_{\text{rat}} = 0.991$. The compressive Young's modulus can be assumed to vary in a linear fashion ($E^c_{11}(\kappa^{-1}) = n_1\kappa^{-1} + n_2$, where $n_1 = -2.05 \times 10^4$ and $n_2 = 125.40$), where the corresponding coefficient of determination is approximately $R^2_{\text{lin}} = 0.994$, as shown in Figure 12b.

Comparing the results with the experimental values of the longitudinal compressive strength of several composite material systems, having similar fibre volume fractions, such as AS4/8552 ($X^c \approx 1530$ MPa), IM7/8552 ($X^c \approx 1689$ MPa), and IM10/8552 ($X^c \approx 1793$ MPa) (Hexcel, 2016a) or IMA/M21 ($X^c \approx 1500$ MPa), AS7/M21 ($X^c \approx 1560$ MPa), and IM7/M21 ($X^c \approx 1790$ MPa) (Hexcel, 2016b), it is evident that only the RVEs having fibres with a more realistic initial fibre misalignment angle distribution (Sebaey et al. (2019), found for an IM7/8552 and an IM7/PEEK UD material systems, a von Mises concentration parameter of $\kappa = 1582.91$ and $\kappa = 2069.72$, respectively) yielded reasonable longitudinal compressive strengths. In contrast, as shown in Figure 13, the idealised RVE incorporating perfectly aligned fibres ($\kappa = \infty$), did not form a kink-band, due to the unrealistic spatial representation of the fibres, but a sort of crushing scenario, in which the RVE failed at higher applied strains in a region near to the boundaries of the RVE, overpredicting the mechanical performance of the material.

[Figure 13 about here.]

By considering the non-uniform variation of the fibre waviness along the RVE, when this waviness was relatively high, a local failure in the highest misaligned region was observed prior to ultimate failure. Figure 14 shows the contour plots of the equivalent plastic strain (equation (8)), at different stages of the damage process, associated with an RVE with $\kappa = 1500$. The first appearance of non-linearity was in a region where the fibres were highly misaligned, leading to local damage propagation, and for a higher applied strain, catastrophic failure of the material.

[Figure 14 about here.]

Interestingly, some RVEs exhibited a wedge-shaped kink-band, as shown in Figure 15. This was also seen experimentally (Sun et al., 2019a, Wang et al., 2019), where, during compressive loading, localised areas of the material having smaller degrees of misalignment formed fibre kink-bands which act together to move a "wedge" of material upwards, thus leading to a different kink-band shape.

[Figure 15 about here.]

Even if fibre-matrix interfacial friction is expected to mostly affect the post-peak response, the effect of friction on the mechanical performance of the material, up to peak load, was studied. Two RVEs having different concentration parameters, i.e. $\kappa = 2000$ and $\kappa = 8000$ were analysed considering a frictionless ($\mu_\tau = 0$) interface. Figure 16a shows the longitudinal compressive reaction force vs. the applied displacement for the two RVEs having different interfacial friction coefficients. The difference in peak load is larger for the RVE having the highest degree of misalignment, exhibiting a difference in approximately 5%, where the less misaligned RVE did not show any substantial decrease in peak load, i.e. less than 0.01%. This is due to the amount of frictional energy that is dissipated during damage propagation (see Figure 16b). As shown, the amount of energy dissipated by friction is much greater for the case of the RVE with $\kappa = 2000$, in comparison to the RVE with $\kappa = 8000$. The RVEs with a frictionless interface still exhibit a level of energy dissipation, since the general contact algorithm implements friction with self-contact.

[Figure 16 about here.]

3.1.4. Kink-band width and fibre rotation angle

The developed kink-band is characterised by certain features, namely its width, angle, and fibre rotation within the kink-band. There is strong empirical evidence which shows that for most thermoset-based composites, when the kink-band is formed (before softening), the fibres within the band rotate by an angle of $15° \leqslant \varphi_{kb}^{\exp} \leqslant 30°$ (Soutis et al., 1993, Moran et al., 1995, Vogler, Kyriakides, 2001, Gutkin et al., 2010b). In contrast, the values measured for both kink-band angle and width have been more disperse, i.e. $5° \leqslant \beta_{kb}^{\exp} \leqslant 30°$ (Kyriakides et al., 1995, Vogler et al., 2001, Lee, Soutis, 2007) and $25\ \mu\text{m} \leqslant w_{kb}^{\exp} \leqslant 80\ \mu\text{m}$ (Jelf, Fleck, 1992, Jumahat et al., 2010, Laffan et al., 2012, Zobeiry et al., 2015), respectively. The kink-band width, w_{kb}, is shown to increase with increasing radii of the fibrous reinforcements, i.e. $w_{kb} \propto R_f$ (Fleck et al., 1995, Budiansky et al., 1998), being approximately equal to 20 times the fibre radii (Soutis et al., 1993). The kink-band angle, β_{kb}, is not explored in this work, since, even if the applied BCs allow for its qualitative representation (in Figure 14d: $\beta_{kb} \approx 13°$), for its proper evaluation, for different κ, a thicker RVE is needed.

The kink-band width, w_{kb}, was computed as the distance between the two extreme points of the kink-band, which have the highest stress, as soon as the kink-band is formed, as suggested by Pimenta et al. (2009). The fibre rotation angle, φ_{kb}, was measured as the angle that the kink-band forms with a horizontal line. Figure 17 shows the local longitudinal stress along the kink-band for three different RVEs, having different degrees of misalignment, where both the kink-band width and fibre rotation angle are highlighted. Table 7 shows the estimated quantitative results of the kink-band width and fibre rotation angle, for different concentration parameters, κ. Moreover, the evolution of both w_{kb} and φ_{kb} were quantified for the case presented in Figure 11 - (A): $w_{kb} \approx 36$ μm and $\varphi_{kb} \approx 6°$; (B): $w_{kb} \approx 40$ μm and $\varphi_{kb} \approx 12°$; and (C1 $\equiv$C2): $w_{kb} \approx 49$ μm and $\varphi_{kb} \approx 23°$.

[Figure 17 about here.]

[Table 7 about here.]

From the aforementioned results, the kink-band width was found to be independent of the initial fibre misalignment distribution. Looking at different fibre radii, a previous preliminary study conducted by the authors, presented by Catalanotti et al. (2020), showed that, for larger fibre radii and same material system, larger kink-band widths were estimated, i.e. $w_{kb} \approx 80$ μm. The fibre rotation angles seem to gradually decrease with κ, where smaller degrees of misalignment, at peak load, promote slightly smaller overall fibre rotation angles.

Despite the initial individual misalignment that each fibre presents when the kink-band is developed, all tend to have the same orientation inside the kink-band. This can be verified in Figure 18, where different fibres within the same RVE, having different initial misalignment distributions, just after peak load, exhibit similar orientation angles in the kink-band.

[Figure 18 about here.]

3.2. Longitudinal tension

To accurately capture the behaviour of composite materials in longitudinal tension, the RVEs must be large enough to capture both co-planar and disperse fibre break clusters. RVEs having an in-plane dimension of $H \approx 175$ μm and a longitudinal dimension of $L_x \approx 500$ μm, were generated. Due to the high computational cost that these FE models yield, and based on previous micromechanical simulations (Tavares et al., 2016, 2017), the aforementioned dimensions were deemed sufficient. These RVEs encompass approximately 600 fibres. For this stress state, RVEs having four different degrees of misalignment were considered: $\kappa = 4000$, $\kappa = 6000$, $\kappa = 8000$, and $\kappa = \infty$ (see equation (1) and Figure 8) and only one simulation was performed per configuration. The in-plane dimensions of each finite element are approximately 0.8 μm, whereas their longitudinal dimension is approximately $l_x^e = L_x/150 = 4$ μm. As mentioned by several authors (Watson, Smith, 1985, Gulino, Phoenix, 1991, Tavares et al., 2017), the Weibull distribution may lead to overestimations of the fibre strength at short gauge lengths, however, a refined discretisation of the microstructure for such long RVEs is needed. Since the objective of this work is to analyse the effect of fibre misalignment on the behaviour of the material, a Weibull distribution was deemed to be sufficiently accurate to represent the stochastic distribution of the tensile strength of the fibres. Moreover, even if there are several methods to determine clusters of broken fibres (Sibson, 1973, Murtagh, Contreras, 2012), here it is chosen to evaluate the formation of fibre break clusters in a qualitative way.

3.2.1. Global response and formation of fibre break clusters

The longitudinal stress-strain curves for the four different RVEs are shown in Figure 19. For a better understanding of the in-plane fibre break clustering process, three different points (associated with $\kappa = \infty$), corresponding to different applied strains, are highlighted, as well as the corresponding contour plots of the fibre (equation (6)) and matrix (equation (11)) damage, in the critical section of the RVE: 1) initial broken fibres, as well as damage in the surrounding matrix; 2) development of a critical cluster, causing; 3) the catastrophic failure of the material.

[Figure 19 about here.]

The overall longitudinal tensile mechanical response of the material is not substantially affected by the initial fibre misalignment. Even if the Young's modulus slightly decreases with decreasing κ (from $E_{11} \approx 125$ GPa to $E_{11} \approx 121$ GPa), the peak stresses are all very similar. With increasing strain, the number of broken fibres increase, leading to the formation of small clusters of broken fibres. Despite the misalignment, the same cluster-type formation was observed for all RVEs, where the maximum number of fibre fractures was qualitatively the same.

The majority of fibres did not fail in the same plane, leading to the formation of disperse clusters, where the locations of fibre breaks are observed in multiple locations along the length of the RVE (see Figure 20).

[Figure 20 about here.]

3.2.2. Local damage mechanisms

Certain local mechanisms such as the ineffective length, debond length, stress profile along a fibre, and the effect of fibre-matrix interfacial friction and misalignment, are analysed in this section. These local mechanisms are assessed with no *prior* cracks in the matrix, since they play an important role in the stress recovery of the broken fibre and consequently in the debond length (Swolfs et al., 2015b). Moreover, there are several parameters which locally affect the tensile damage process, such as, distribution of the microstructure, material properties of the matrix constituent, and strain-rate (Zeng et al., 1997, Heuvel van den et al., 2000, Zhao, Takeda, 2000, Hobbiebrunken et al., 2007, Foreman et al., 2009, Swolfs et al., 2015b, Tavares et al., 2017), where most of which were analysed by Tavares et al. (2019a) using the Spring Element Model (SEM).

The ineffective length is a measure of the stress recovery length of the fibre and can be defined as twice the length at which the broken fibre is able to carry 90% of the applied stress (Rosen, 1964). To analyse this effect, fibres which were far from the boundaries of the RVEs were chosen to give a more detailed evaluation of the local damage mechanisms. Figures 21a and Figures 21b show the contour plots of the longitudinal stress and cohesive interfacial damage along the length of a single fibre inside an RVE with $\kappa = \infty$, for different friction coefficients and same applied strain, just after fibre breakage. Fibre breakage was promoted at its centre, by artificially decreasing the local tensile strength of the central elements to 4050 MPa.

[Figure 21 about here.]

By increasing the friction coefficient, both ineffective and debond length are reduced, leading to a higher stress recovery profile of the fibre, slowing down the damage process. Moreover, Figure 21c shows the numerical predictions of the volumetrically homogenised longitudinal stress along the single fibre, for different friction coefficients. After fibre fracture, different interfacial friction coefficients lead to slightly different stress profiles, where for the same longitudinal position, a greater homogenised stress can be observed, leading to an ineffective length of ≈ 68 μm and ≈ 55 μm, for a frictionless interface and for one considering $\mu_\tau = 0.70$, respectively.

To locally assess the effect of fibre waviness, two different fibres positioned far from the boundaries of the RVE, having qualitatively a different degree of misalignment, were chosen inside an RVE with $\kappa = 4000$. In Figures 22a and 22b, the contour plots of the fibre-matrix interface damage and longitudinal stress, for the two different fibres are shown, and Figure 22c shows the volumetrically homogenised longitudinal stress of each cross-section, along each fibre, having qualitatively different degrees of misalignment for central elements having two different failure strains ($\varepsilon_f^0 = 0.6\%$ in red and $\varepsilon_f^0 = 1.1\%$ in blue). The friction coefficient was kept constant and equal to $\mu_\tau = 0.52$.

[Figure 22 about here.]

For both analysed failure strains, the ineffective length increases with initial fibre misalignment. The difference between the ineffective length of a fibre having a small and a high degree of misalignment, was approximately 10 μm, for both failure strains. Additionally, it was noted that the debonded length increases with increasing failure strain. The changes in the local damage mechanisms, due to initial fibre waviness, may alter the development of fibre break clustering, as they change the local stress redistribution to neighbouring fibres, after fibre breakage. However, the overall behaviour of the composite is not directly connected to the local effects acting on a single fibre, but a bigger collection of fibres, possibly making these individual damage mechanisms, which act in a particular region of a single fibre, negligible when comparing to the longitudinal tensile strength distribution.

4. Conclusions

The importance of representing the realistic 3D microstructure of UD composite materials was addressed in this work, namely when the material is submitted to a longitudinal (fibre-direction) stress state. A computational finite element micromechanics framework was built, using a recent methodology to generate the initial fibre misalignment via a combination of a stochastic process and an optimisation procedure (Catalanotti, Sebaey, 2019). RVEs having different degrees of misalignment were then generated to simulate the longitudinal compressive and tensile failure, and analyse the associated intrinsic damage mechanisms.

Different results associated with the compressive failure of the material by fibre kinking were obtained using the present framework. It was observed that by decreasing the degree of misalignment of the RVEs (increasing κ), both Young's modulus and peak stress increased, where these results have shown to have a best fit using linear and rational functions, respectively. The RVEs having a more realistic κ (experimentally obtained by Sebaey et al. (2019)), yielded peak stresses comparable to empirical compressive strengths of different material systems (Hexcel, 2016a,b). Moreover, the present framework enabled the analysis of the kink-band width and of the fibre rotation inside the kink-band. The kink-band width was found to be independent of initial fibre waviness, in contrast, the fibre rotation angle was sensitive to it, where bigger degrees of initial misalignment lead to higher fibre rotation angles. Additionally, despite having different initial misalignment, after peak load, fibres which belong to the same RVE, exhibited similar orientation angles, in the kink-band region. Finally, friction seems to play a role for lower concentration parameters (higher misalignment), in which the energy dissipated by friction was higher.

The failure mechanisms associated with a longitudinal tensile loading were also evaluated. By generating RVEs with different fibre misalignments, the overall performance of the material remained unaltered, i.e. the peak stress remained the same and the Young's modulus changed slightly. Moreover, the RVEs exhibited similar damage patterns, leading to a similar type of fibre break clustering. More detailed analyses were undertaken to assess the effect of friction and degree of misalignment on the local load carrying capacity of the broken fibres. Friction was shown to decrease the ineffective length of the fibres, whereas misalignment increased the ineffective length, possibly leading to a faster progression of damage, changing the stress redistribution to neighbouring fibres. However, these local phenomena do not seem to dictate the final failure of the material, making the variation of the longitudinal tensile strength of the reinforcements the most influential parameter on the final failure of the material.

Idealised representations of the microstructure cannot properly represent fibre kinking. In contrast, a more realistic spatial distribution (Catalanotti, Sebaey, 2019) guarantees a correct representation of the damage mechanisms associated with longitudinal compressive failure of UD materials. Despite the magnitude of the initial fibre misalignment, the longitudinal tensile behaviour and failure mechanisms were all very similar. There are certain limitations which were not assessed here. Fibre compressive and/or shear failure was not considered, due to a lack of strength characterisation testing of neat fibres, which can lead to an overestimation of the local and overall performance of the material for small degrees of fibre misalignment. Finally, there is a need for developing analytical/semi-analytical models which are able to take into account the stochastic variability of the initial waviness of the reinforcements, thus yielding representative estimations of the parameters associated with compressive failure by fibre kinking.

This study has shown that micromechanics can be treated as a reliable computational tool to analyse certain geometric and material variabilities which cannot be assessed using ply- or laminate-level analyses. Further studies can encompass the investigation of the effect of initial fibre waviness on the transverse tensile and compressive response, in- and out-of-plane shear loading scenarios, as well as other biaxial and triaxial loading conditions.

Data availability

Datasets related to this article can be found at http://dx.doi.org/10.17632/4kbd2fr4yf.2, an open-source online data repository hosted at Mendeley Data.

Acknowledgements

The authors gratefully acknowledge the financial support of the project ICONIC – Improving the crashworthiness of composite transportation structures. ICONIC has received funding from the European Union's Horizon 2020 research and innovation programme under the Marie Skłodowska-Curie grant agreement No 721256. The content reflects only the author's view and the Agency is not responsible for any use that may be made of the information it contains.

References

Abaqus Documentation. Providence, RI, USA, 2018.

Argon A.S. Fracture of Composites // Treatise on Materials Science & Technology. 1972. 79–114.

Arteiro A., Catalanotti G., Melro A. R., Linde P., Camanho P. P. Micro-mechanical analysis of the in situ effect in polymer composite laminates // Composite Structures. 2014. 116, 1. 827–840.

Arteiro A., Catalanotti G., Melro A. R., Linde P., Camanho P. P. Micro-mechanical analysis of the effect of ply thickness on the transverse compressive strength of polymer composites // Composites Part A: Applied Science and Manufacturing. 2015. 79. 127–137.

Arteiro Albertino, Catalanotti Giuseppe, Reinoso José, Linde Peter, Camanho Pedro P. Simulation of the Mechanical Response of Thin-Ply Composites: From Computational Micro-Mechanics to Structural Analysis // Archives of Computational Methods in Engineering. nov 2019. 26, 5. 1445–1487.

Bai Xiaoming, Bessa Miguel A., Melro António R., Camanho Pedro P., Guo Licheng, Liu Wing K. High-fidelity micro-scale modeling of the thermo-visco-plastic behavior of carbon fiber polymer matrix composites // Composite Structures. 2015. 134. 132–141.

Bažant Z. P., Kim Jang-jay H., Daniel Isaac M., Becq-Giraudon Emilie, Zi G. Size effect on compression strength of fiber composites failing by kink band propagation // International Journal of Fracture. 1999. 07, 1984. 103–141.

Bažant Z. P., Oh B. H. Crack band theory for fracture of concrete // Materials and Structures. 1983. 16. 155–177.

Benzeggagh M. L., Kenane M. Measurement of mixed-mode delamination fracture toughness of unidirectional glass/epoxy composites with mixed-mode bending apparatus // Composites Science and Technology. 1996. 56, 4. 439–449.

Beyerlein Irene J., Phoenix S.Leigh. Statistics for the strength and size effects of microcomposites with four carbon fibers in epoxy resin // Composites Science and Technology. jan 1996. 56, 1. 75–92.

Bishara M., Rolfes R., Allix O. Revealing complex aspects of compressive failure of polymer composites Part I: Fiber kinking at microscale // Composite Structures. jun 2017. 169. 105–115.

Budiansky B., Fleck N.A. Compressive failure of fibre composites // Journal of the Mechanics and Physics of Solids. jan 1993. 41, 1. 183–211.

Budiansky B., Fleck N.A., Amazigo J.C. On kink-band propagation in fiber composites // Journal of the Mechanics and Physics of Solids. sep 1998. 46, 9. 1637–1653.

Budiansky Bernard. Micromechanics // Computers & Structures. jan 1983. 16, 1-4. 3–12.

Budiansky Bernard, Fleck Norman A. Compressive Kinking of Fiber Composites: A Topical Review // Applied Mechanics Reviews. jun 1994. 47, 6S. S246–S250.

Catalanotti G. On the generation of RVE-based models of composites reinforced with long fibres or spherical particles // Composite Structures. 2016. 138. 84–95.

Catalanotti G., Sebaey T.A. An algorithm for the generation of three-dimensional statistically Representative Volume Elements of unidirectional fibre-reinforced plastics: Focusing on the fibres waviness // Composite Structures. nov 2019. 227. 111272.

Catalanotti G., Varandas L.F., Melro A.R., Sebaey T.A., Bessa M.A., Falzon B.G. Modelling the longitudinal failure of fibre-reinforced composites at micro-scale // Multi-Scale Continuum Mechanics Modelling of Fibre-Reinforced Polymer Composites. 2020. Chapter 12. Submitted.

Chen Zhangxing, Tang Haibin, Shao Yimin, Sun Qingping, Zhou Guowei, Li Yang, Xu Hongyi, Zeng Danielle, Su Xuming. Failure of chopped carbon fiber Sheet Molding Compound (SMC) composites under uniaxial tensile loading: Computational prediction and experimental analysis // Composites Part A: Applied Science and Manufacturing. mar 2019. 118. 117–130.

Clarke A.R., Archenhold G., Davidson N.C. A novel technique for determining the 3D spatial distribution of glass fibres in polymer composites // Composites Science and Technology. jan 1995. 55, 1. 75–91.

Costa Sérgio, Fagerström Martin, Olsson Robin. Development and validation of a finite deformation fibre kinking model for crushing of composites // Composites Science and Technology. may 2020. 108236.

Creighton C.J, Sutcliffe M.P.F, Clyne T.W. A multiple field image analysis procedure for characterisation of fibre alignment in composites // Composites Part A: Applied Science and Manufacturing. feb 2001. 32, 2. 221–229.

Curtin W. A. Tensile Strength of Fiber-Reinforced Composites: III. Beyond the Traditional Weibull Model for Fiber Strengths // Journal of Composite Materials. aug 2000. 34, 15. 1301–1332.

Dalli D., Catalanotti G., Varandas L.F., Falzon B.G., Foster S. Mode I intralaminar fracture toughness of 2D woven carbon fibre reinforced composites: A comparison of stable and unstable crack propagation techniques // Engineering Fracture Mechanics. jun 2019. 214. 427–448.

Dalli D., Catalanotti G., Varandas L.F., Falzon B.G., Foster S. Compressive intralaminar fracture toughness and residual strength of 2D Woven carbon fibre reinforced composites: New developments on using the size effect method // Theoretical and Applied Fracture Mechanics. jan 2020. 102487.

Daum B., Feld N., Allix O., Rolfes R. A review of computational modelling approaches to compressive failure in laminates // Composites Science and Technology. sep 2019. 181. 107663.

Fleck N. A., Deng L., Budiansky B. Prediction of Kink Width in Compressed Fiber Composites // Journal of Applied Mechanics. jun 1995. 62, 2. 329–337.

Foreman J. P., Behzadi S., Tsampas S. A., Porter D., Curtis P. T., Jones F. R. Rate dependent multiscale modelling of fibre reinforced composites // Plastics, Rubber and Composites. may 2009. 38, 2-4. 67–71.

Galli M., Botsis J., Janczak-Rusch J. An elastoplastic three-dimensional homogenization model for particle reinforced composites // Computational Materials Science. 2008. 41, 3. 312–321.

Ghorbel Elhem. A viscoplastic constitutive model for polymeric materials // International Journal of Plasticity. nov 2008. 24, 11. 2032–2058.

Gitman I. M., Askes H., Sluys L. J. Representative volume: Existence and size determination // Engineering Fracture Mechanics. 2007. 74, 16. 2518–2534.

Gitman I. M., Gitman M. B., Askes H. Quantification of stochastically stable representative volumes for random heterogeneous materials // Archive of Applied Mechanics. jan 2006. 75, 2-3. 79–92.

Guerrero J.M., Mayugo J.A., Costa J., Turon A. A 3D Progressive Failure Model for predicting pseudo-ductility in hybrid unidirectional composite materials under fibre tensile loading // Composites Part A: Applied Science and Manufacturing. apr 2018. 107. 579–591.

Gulino R., Phoenix S. L. Weibull strength statistics for graphite fibres measured from the break progression in a model graphite/glass/epoxy microcomposite // Journal of Materials Science. 1991. 26, 11. 3107–3118.

Gutkin R., Pinho S. T., Robinson P., Curtis P. T. Micro-mechanical modelling of shear-driven fibre compressive failure and of fibre kinking for failure envelope generation in CFRP laminates // Composites Science and Technology. 2010a. 70, 8. 1214–1222.

Gutkin R., Pinho S. T., Robinson P., Curtis P. T. On the transition from shear-driven fibre compressive failure to fibre kinking in notched CFRP laminates under longitudinal compression // Composites Science and Technology. 2010b. 70, 8. 1223–1231.

Hashin Z. Analysis of Composite Materials - A Survey // Journal of Applied Mechanics. sep 1983. 50, 3. 481–505.

Herráez M., Bergan A.C., Lopes C.S., González C. Computational micromechanics model for the analysis of fiber kinking in unidirectional fiber-reinforced polymers // Mechanics of Materials. mar 2020. 142. 103299.

Herráez M., Fernández A., Lopes C. S., González C. Strength and toughness of structural fibres for composite material reinforcement // Philosophical Transactions of the Royal Society A: Mathematical, Physical and Engineering Sciences. 2016. 374, 2071.

Herráez Miguel, Bergan Andrew C., González Carlos. Modeling fiber kinking at the microscale and mesoscale. // Technical report, NASA/TP2018220105. 2018. October.

Heuvel P. W. J. van den, Peijs T., Young R. J. Failure phenomena in two-dimensional multi-fibre micro-composites. Part 4: a Raman spectroscopic study on the influence of the matrix yield stress on stress concentrations // Composites Part A: Applied Science and Manufacturing. feb 2000. 31, 2. 165–171.

Hexcel . HexPly® 8552 Matrix, Epoxy matrix (180° C/356° F curing) // https://www.hexcel.com/user_area/content_media/raw/HexPly_8552_eu_DataSheet.pdf. 2016a.

Hexcel . HexPly® M21 Matrix, Epoxy matrix (180° C/356° F curing) // https://www.hexcel.com/user_area/content_media/raw/HexPly_M21_global_DataSheet.pdf. 2016b.

Hill R. Elastic properties of reinforced solids: Some theoretical principles // Journal of the Mechanics and Physics of Solids. sep 1963. 11, 5. 357–372.

Hillig W. B. Effect of fibre misalignment on the fracture behaviour of fibre-reinforced composites // Journal of Materials Science. 1994. 29, 2. 419–423.

Hobbiebrunken Thomas, Fiedler Bodo, Hojo Masaki, Tanaka Mototsugu. Experimental determination of the true epoxy resin strength using micro-scaled specimens // Composites Part A: Applied Science and Manufacturing. mar 2007. 38, 3. 814–818.

Hsu S.-Y., Vogler T. J., Kyriakides S. Compressive Strength Predictions for Fiber Composites // Journal of Applied Mechanics. mar 1998. 65, 1. 7–16.

Jelf P.M., Fleck N.A. Compression Failure Mechanisms in Unidirectional Composites // Journal of Composite Materials. dec 1992. 26, 18. 2706–2726.

Jumahat A., Soutis C., Jones F. R., Hodzic A. Fracture mechanisms and failure analysis of carbon fibre / toughened epoxy composites subjected to compressive loading // Composite Structures. 2010. 92, 2. 295–305.

Kanit T., Forest S., Galliet I., Mounoury V., Jeulin D. Determination of the size of the representative volume element for random composites: statistical and numerical approach // International Journal of Solids and Structures. jun 2003. 40, 13-14. 3647–3679.

Kyriakides S., Arseculeratne R., Perry E.J., Liechti K.M. On the compressive failure of fiber reinforced composites // International Journal of Solids and Structures. mar 1995. 32, 6-7. 689–738.

Laffan M.J., Pinho S.T., Robinson P., Iannucci L. Measurement of the in situ ply fracture toughness associated with mode I fibre tensile failure in FRP. Part II: Size and lay-up effects // Composites Science and Technology. apr 2010. 70, 4. 614–621.

Laffan M.J., Pinho S.T., Robinson P., Iannucci L., McMillan A.J. Measurement of the fracture toughness associated with the longitudinal fibre compressive failure mode of laminated composites // Composites Part A: Applied Science and Manufacturing. nov 2012. 43, 11. 1930–1938.

Lamon Jacques. Mécanique de la rupture fragile et de l'endommagement : Approches statistiques et probabilistes. Paris: Hermès Science Publications, 2007. Hermes-Lav.

Lee J., Soutis C. A study on the compressive strength of thick carbon fibreepoxy laminates // Composites Science and Technology. aug 2007. 67, 10. 2015–2026.

Lin Ye . Role of matrix resin in delamination onset and growth in composite laminates // Composites Science and Technology. 1988. 33, 4. 257–277.

Meer Frans P. van der, Raijmaekers Sibrand, Rocha Iuri B.C.M. Interpreting the single fiber fragmentation test with numerical simulations // Composites Part A: Applied Science and Manufacturing. mar 2019. 118. 259–266.

Melro A. R., Camanho P. P., Andrade Pires F. M., Pinho S. T. Micromechanical analysis of polymer composites reinforced by unidirectional fibres: Part I-Constitutive modelling // International Journal of Solids and Structures. 2013a. 50, 11-12. 1897–1905.

Melro A. R., Camanho P. P., Andrade Pires F. M., Pinho S. T. Micromechanical analysis of polymer composites reinforced by unidirectional fibres: Part II-Micromechanical analyses // International Journal of Solids and Structures. 2013b. 50, 11-12. 1906–1915.

Mizukami Koichi, Mizutani Yoshihiro, Todoroki Akira, Suzuki Yoshiro. Detection of in-plane and out-of-plane fiber waviness in unidirectional carbon fiber reinforced composites using eddy current testing // Composites Part B: Engineering. feb 2016. 86. 84–94.

Moran P. M., Liu X. H., Shih C. F. Kink band formation and band broadening in fiber composites under compressive loading // Acta Metallurgica et Materialia. 1995. 43, 8. 2943–2958.

Murtagh Fionn, Contreras Pedro. Algorithms for hierarchical clustering: an overview // Wiley Interdisciplinary Reviews: Data Mining and Knowledge Discovery. jan 2012. 2, 1. 86–97.

Naya F., Herráez M., Lopes C. S., González C., Van der Veen S., Pons F. Computational micromechanics of fiber kinking in unidirectional FRP under different environmental conditions // Composites Science and Technology. 2017. 144. 26–35.

Pain Damien, Drinkwater Bruce W. Detection of Fibre Waviness Using Ultrasonic Array Scattering Data // Journal of Nondestructive Evaluation. sep 2013. 32, 3. 215–227.

Pimenta S., Gutkin R., Pinho S.T., Robinson P. A micromechanical model for kink-band formation: Part IIAnalytical modelling // Composites Science and Technology. jun 2009. 69, 7-8. 956–964.

Pinho S. T., Gutkin R., Pimenta S., De Carvalho N. V., Robinson P. On longitudinal compressive failure of carbon-fibre-reinforced polymer: from unidirectional to woven, and from virgin to recycled // Philosophical Transactions of the Royal Society A: Mathematical, Physical and Engineering Sciences. apr 2012. 370, 1965. 1871–1895.

Prabhakar Pavana, Waas Anthony M. Interaction between kinking and splitting in the compressive failure of unidirectional fiber reinforced laminated composites // Composite Structures. 2013. 98. 85–92.

Requena Guillermo, Fiedler Georg, Seiser Bernhard, Degischer Peter, Di Michiel Marco, Buslaps Thomas. 3D-Quantification of the distribution of continuous fibres in unidirectionally reinforced composites // Composites Part A: Applied Science and Manufacturing. feb 2009. 40, 2. 152–163.

Rosen B. W. Tensile failure of fibrous composites // AIAA Journal. nov 1964. 2, 11. 1985–1991.

Scott A. E., Mavrogordato M., Wright P., Sinclair I., Spearing S. M. In situ fibre fracture measurement in carbonepoxy laminates using high resolution computed tomography // Composites Science and Technology. aug 2011. 71, 12. 1471–1477.

Scott A. E., Sinclair I., Spearing S. M., Thionnet A., Bunsell A. R. Damage accumulation in a carbon/epoxy composite: Comparison between a multiscale model and computed tomography experimental results // Composites Part A: Applied Science and Manufacturing. sep 2012. 43, 9. 1514–1522.

Sebaey T. A., Catalanotti G., Dowd N. P. O. A microscale integrated approach to measure and model fi bre misalignment in fi bre-reinforced composites // Composites Science and Technology. 2019. 183, June. 107793.

Sibson R. SLINK: An optimally efficient algorithm for the single-link cluster method // The Computer Journal. jan 1973. 16, 1. 30–34.

Soden P., Hinton M. J., Kaddour A. S. Lamina properties, lay-up configurations and loading conditions for a range of fibre-reinforced composite laminates // Composites Science and Technology. jul 1998. 58, 7. 1011–1022.

Soutis C., Curtis P. T., Fleck N. A. Compressive Failure of Notched Carbon Fibre Composites // Proceedings of the Royal Society A: Mathematical, Physical and Engineering Sciences. feb 1993. 440, 1909. 241–256.

St-Pierre Luc, Martorell Ned J., Pinho Silvestre T. Stress redistribution around clusters of broken fibres in a composite // Composite Structures. may 2017. 168. 226–233.

Stroeven M., Askes H., Sluys L.J. Numerical determination of representative volumes for granular materials // Computer Methods in Applied Mechanics and Engineering. jul 2004. 193, 30-32. 3221–3238.

Sun Qingping, Zhou Guowei, Guo Haiding, Meng Zhaoxu, Chen Zhangxing, Liu Haolong, Kang Hongtae, Su Xuming. Failure mechanisms of cross-ply carbon fiber reinforced polymer laminates under longitudinal compression with experimental and computational analyses // Composites Part B: Engineering. jun 2019a. 167. 147–160.

Sun Qingping, Zhou Guowei, Meng Zhaoxu, Guo Haiding, Chen Zhangxing, Liu Haolong, Kang Hongtae, Keten Sinan, Su Xuming. Failure criteria of unidirectional carbon fiber reinforced polymer composites informed by a computational micromechanics model // Composites Science and Technology. mar 2019b. 172. 81–95.

Sutcliffe M. P. F., Lemanski S. L., Scott A. E. Measurement of fibre waviness in industrial composite components // Composites Science and Technology. 2012. 72, 16. 2016–2023.

Swolfs Y., Morton H., Scott A. E., Gorbatikh L., Reed P. A. S., Sinclair I., Spearing S. M., Verpoest I. Synchrotron radiation computed tomography for experimental validation of a tensile strength model for unidirectional fibre-reinforced composites // Composites Part A: Applied Science and Manufacturing. oct 2015a. 77. 106–113.

Swolfs Yentl, McMeeking Robert M., Verpoest Ignaas, Gorbatikh Larissa. Matrix cracks around fibre breaks and their effect on stress redistribution and failure development in unidirectional composites // Composites Science and Technology. 2015b. 108. 16–22.

Swolfs Yentl, McMeeking Robert M., Verpoest Ignaas, Gorbatikh Larissa. The effect of fibre dispersion on initial failure strain and cluster development in unidirectional carbon/glass hybrid composites // Composites Part A: Applied Science and Manufacturing. 2015c. 69. 279–287.

Swolfs Yentl, Verpoest Ignaas, Gorbatikh Larissa. Maximising the hybrid effect in unidirectional hybrid composites // Materials & Design. mar 2016. 93. 39–45.

Tanaka Fumihiko, Okabe Tomonaga, Okuda Haruki, Kinloch Ian A., Young Robert J. Factors controlling the strength of carbon fibres in tension // Composites Part A: Applied Science and Manufacturing. 2014. 57. 88–94.

Tavares Rodrigo P., Guerrero Jose M., Otero Fermin, Turon Albert, Mayugo Joan A., Costa Josep, Camanho Pedro P. Effects of local stress fields around broken fibres on the longitudinal failure of composite materials // International Journal of Solids and Structures. jan 2019a. 156-157. 294–305.

Tavares Rodrigo P., Melro António R., Bessa Miguel A., Turon Albert, Liu Wing K., Camanho Pedro P. Mechanics of hybrid polymer composites: analytical and computational study // Computational Mechanics. 2016. 57, 3. 405–421.

Tavares Rodrigo P., Otero Fermin, Baiges Joan, Turon Albert, Camanho Pedro P. A dynamic spring element model for the prediction of longitudinal failure of polymer composites // Computational Materials Science. 2019b. 160, January. 42–52.

Tavares Rodrigo P., Otero Fermin, Turon Albert, Camanho Pedro P. Effective simulation of the mechanics of longitudinal tensile failure of unidirectional polymer composites // International Journal of Fracture. 2017. 208, 1. 269–285.

Thionnet A., Chou H.Y., Bunsell A. Fibre break processes in unidirectional composites // Composites Part A: Applied Science and Manufacturing. oct 2014. 65. 148–160.

Torres J. P., Vandi L. J., Veidt M., Heitzmann M. T. The mechanical properties of natural fibre composite laminates: A statistical study // Composites Part A: Applied Science and Manufacturing. 2017. 98, March. 99–104.

Triantafyllidis N., Bardenhagen S. The influence of scale size on the stability of periodic solids and the role of associated higher order gradient continuum models // Journal of the Mechanics and Physics of Solids. nov 1996. 44, 11. 1891–1928.

Tschoegl N. W. Failure surfaces in principal stress space // Journal of polymer science Part C: Polymer symposia. 1971. 32, 1. 239–267.

Varandas L.F., Arteiro A., Bessa M.A., Melro A.R., Catalanotti G. The effect of through-thickness compressive stress on mode II interlaminar crack propagation: A computational micromechanics approach // Composite Structures. 2017. 182, September. 326–334.

Varandas L.F., Arteiro A., Catalanotti G., Falzon B.G. Micromechanical analysis of interlaminar crack propagation between angled plies in mode I tests // Composite Structures. 2019. 220, December 2018. 827–841.

Varandas L.F., Catalanotti G., Arteiro A., Melro A.R., Falzon B.G. Micromechanical modelling of interlaminar damage propagation and migration // Multi-Scale Continuum Mechanics Modelling of Fibre-Reinforced Polymer Composites. 2020a. Chapter 11. Submitted.

Varandas Luís F., Catalanotti Giuseppe, Melro António R., Falzon Brian G. On the importance of nesting considerations for accurate computational damage modelling in 2D woven composite materials // Computational Materials Science. feb 2020b. 172. 109323.

Vogler T. J., Hsu S. Y., Kyriakides S. On the initiation and growth of kink bands in fiber composites. Part II: Analysis // International Journal of Solids and Structures. 2001. 38, 15. 2653–2682.

Vogler T. J., Kyriakides S. On the initiation and growth of kink bands in fiber composites: Part I. experiments // International Journal of Solids and Structures. 2001. 38, 15. 2639–2651.

Wang Ying, Chai Yuan, Soutis Costas, Withers Philip J. Evolution of kink bands in a notched unidirectional carbon fibre-epoxy composite under four-point bending // Composites Science and Technology. mar 2019. 172. 143–152.

Watson A. S., Smith R. L. An examination of statistical theories for fibrous materials in the light of experimental data // Journal of Materials Science. sep 1985. 20, 9. 3260–3270.

Weibull Waloddi. A statistical distribution function of wide applicability // Journal of applied mechanics. 1951. 103. 293–297.

Wilhelmsson D., Asp L.E. A high resolution method for characterisation of fibre misalignment angles in composites // Composites Science and Technology. sep 2018. 165. 214–221.

Yerramalli Chandra S., Waas Anthony M. The effect of fiber diameter on the compressive strength of composites - A 3D finite element based study // CMES - Computer Modeling in Engineering and Sciences. 2004. 6, 1. 1–16.

Zeng Qing-Dun, Wang Zhi-Li, Ling Ling. A study of the influence of interfacial damage on stress concentrations in unidirectional composites // Composites Science and Technology. jan 1997. 57, 1. 129–135.

Zhao F.M, Takeda N. Effect of interfacial adhesion and statistical fiber strength on tensile strength of unidirectional glass fiber/epoxy composites. Part I: experiment results // Composites Part A: Applied Science and Manufacturing. nov 2000. 31, 11. 1203–1214.

Zobeiry N., Vaziri R., Poursartip A. Characterization of strain-softening behavior and failure mechanisms of composites under tension and compression // Composites Part A: Applied Science and Manufacturing. 2015. 68. 29–41.

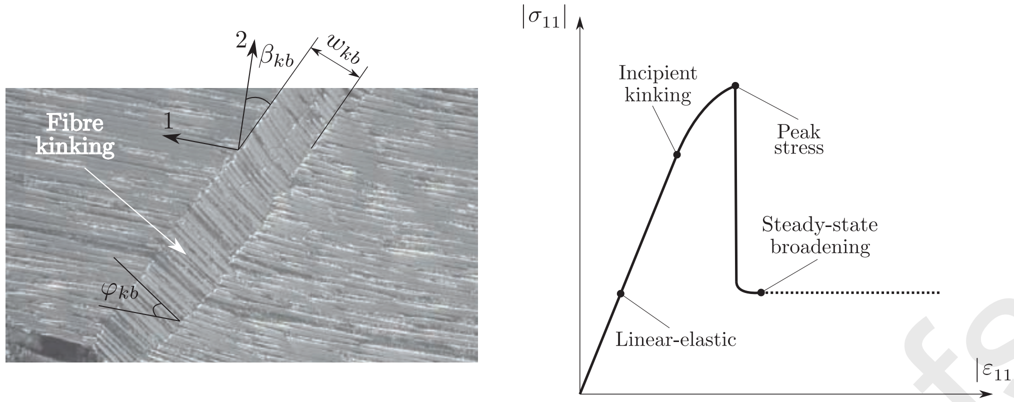

(a) (b)

Figure 1: (a) Micrograph of a developed kink-band, highlighting its width, w_{kb}, angle, β_{kb}, and the fibre rotation angle, φ_{kb}, from Jumahat et al. (2010) (with permission); (b) schematic representation of the longitudinal compressive response of an UD composite material, highlighting the different loading stages.

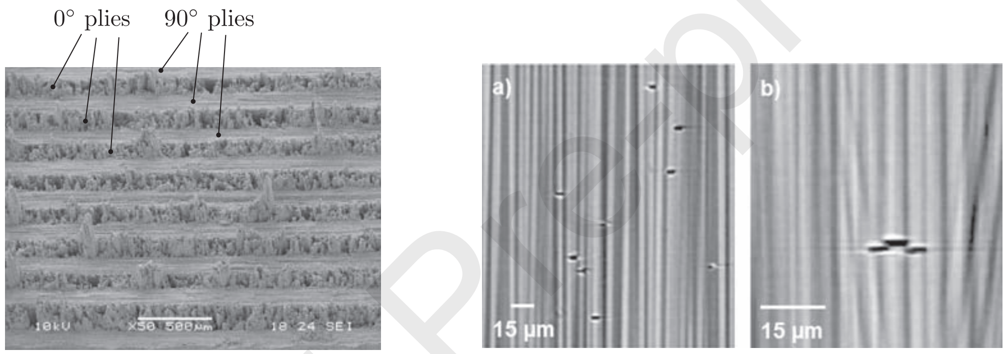

(a) (b)

Figure 2: (a) CT image of a fracture surface of a cross-ply laminate, from Laffan et al. (2010) (with permission) and (b) SRCT image of disperse (left) and co-planar (right) fibre break clusters, from Swolfs et al. (2015a) (with permission).

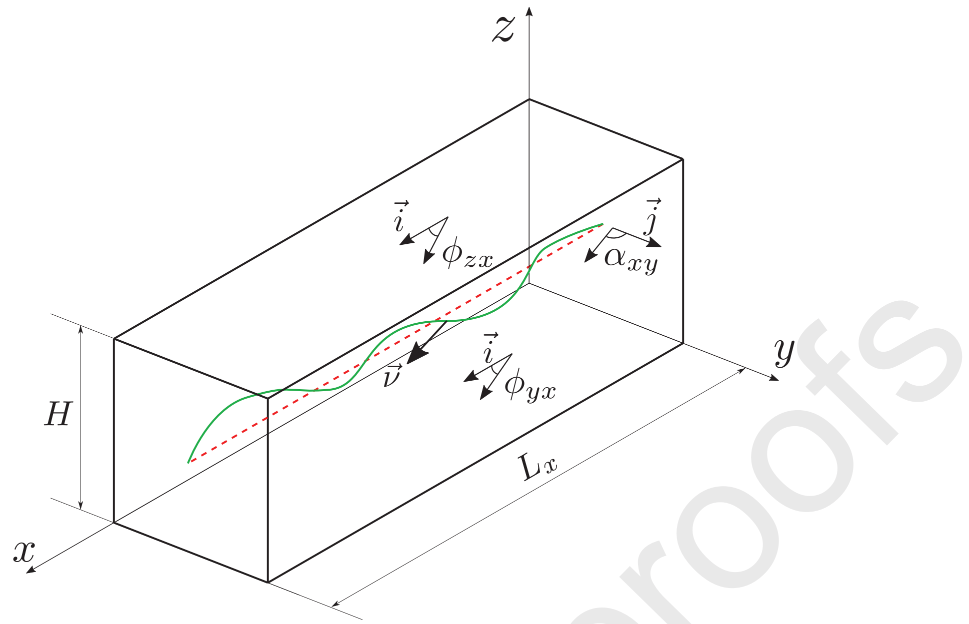

Figure 3: Spatial descriptors that characterise 3D fibre waviness (the green line portraits a representative fibre).

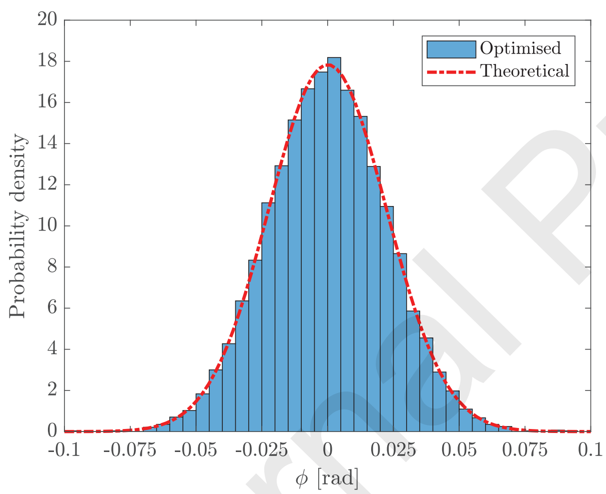

(a) pdf of the distribution.

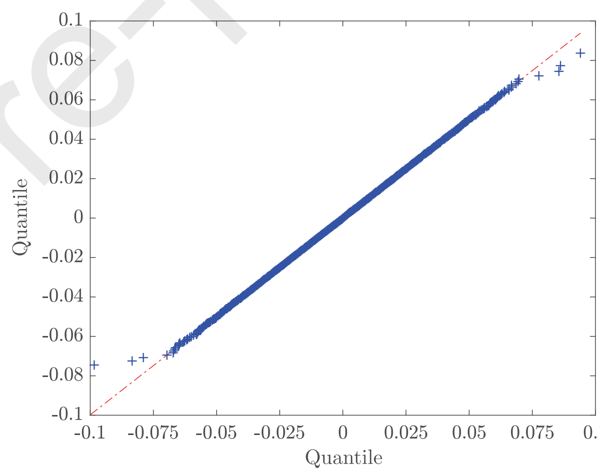

(b) Q-Q plot.

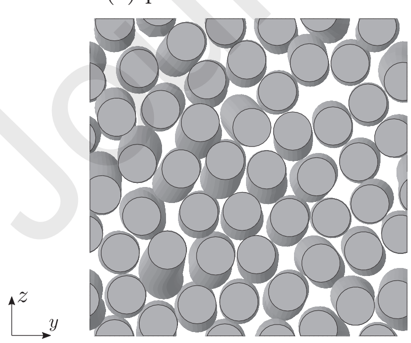

(c) Front view of the fibres.

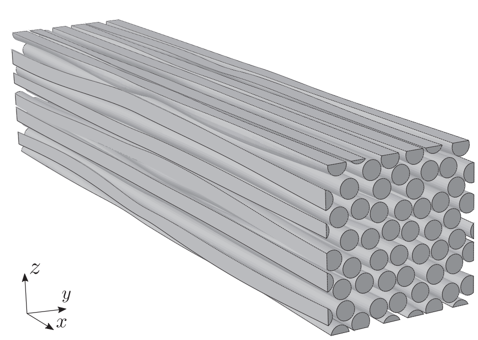

(d) Isometric view of the fibres.

Figure 4: Results associated with a 3D fibre distribution with $\kappa = 2000$.

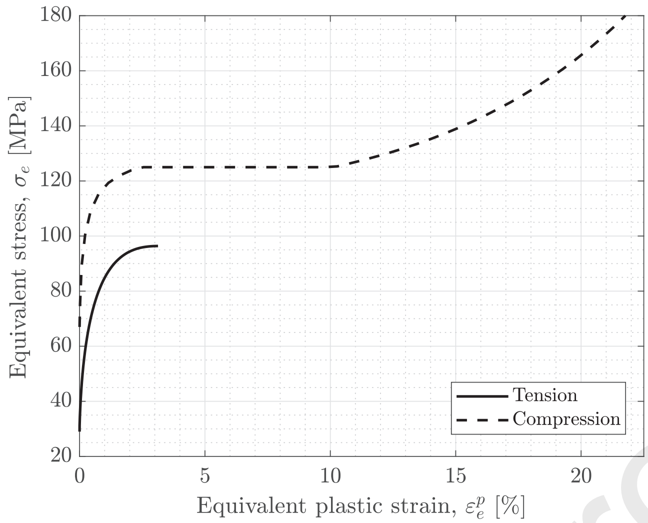

Figure 5: Hardening curves used in the epoxy matrix plasticity model (Melro et al., 2013b, Arteiro et al., 2014, 2015).

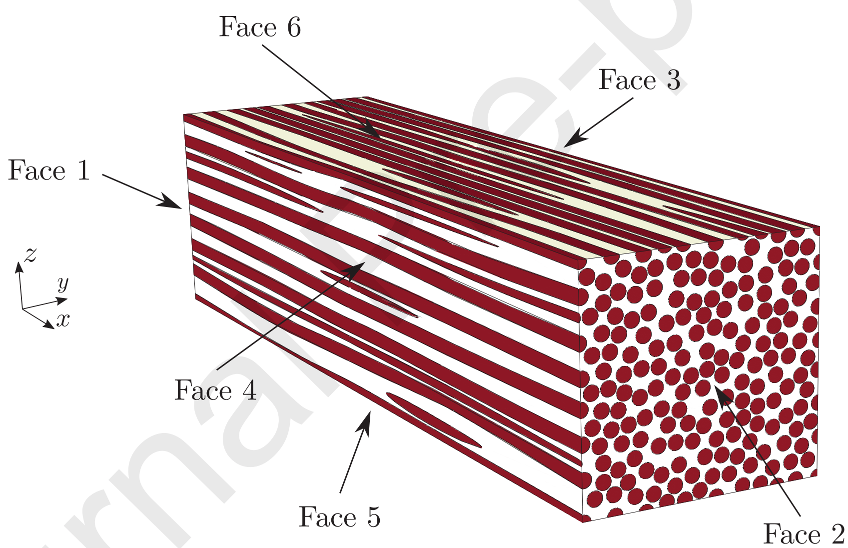

Figure 6: Representation of a misaligned micromechanical RVE, highlighting its different faces. White - epoxy matrix; red - carbon fibres.

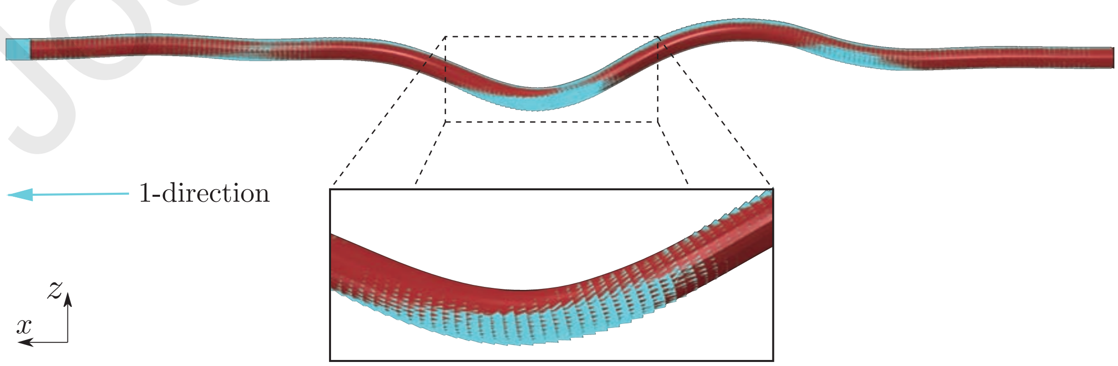

Figure 7: Representation of the main, 1-direction, of each element of a highly misaligned fibre.

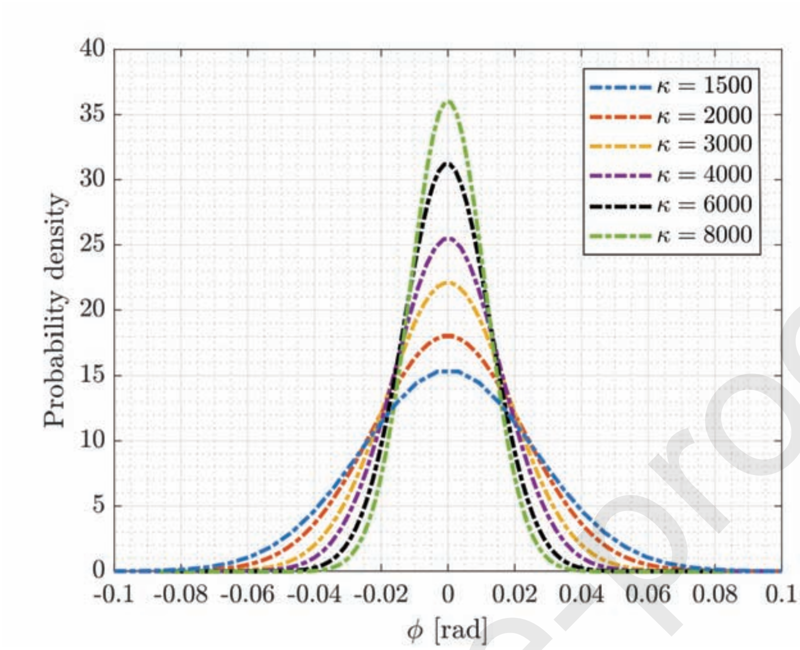

Figure 8: Distribution of the misalignment angles for each κ considered in this section.

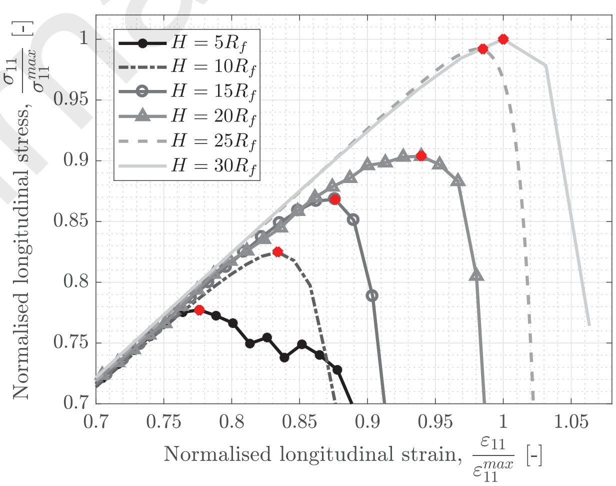

Figure 9: Representative normalised longitudinal compression stress-strain curves for different in-plane dimensions of the RVE, having a constant aspect ratio of $A_r = 4$. The red points indicate the corresponding normalised peak stress.

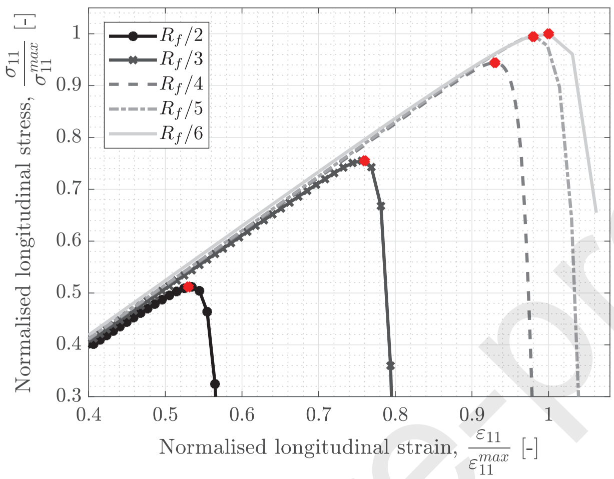

(a) Normalised compressive stress-strain curves for different average mesh densities. The red points indicate the corresponding normalised peak stress.

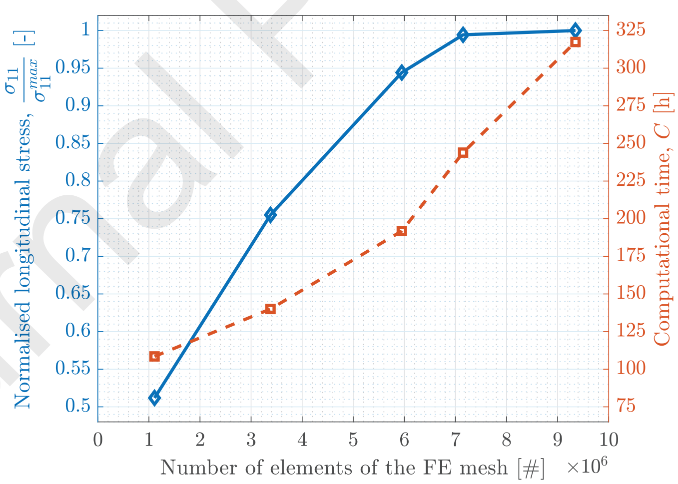

(b) Normalised compressive peak stress and corresponding computational cost vs. mesh density.

Figure 10: Preliminary results to assess the effect of mesh density on the quantitative results ($\kappa = 4000$).

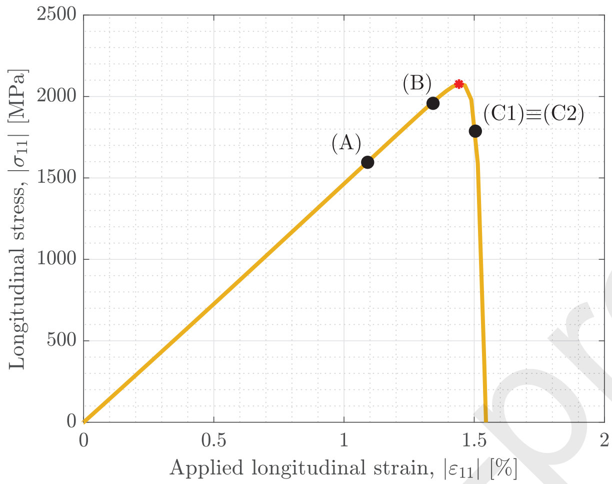

(a) Representative stress-strain curve. The red point indicates the peak stress.

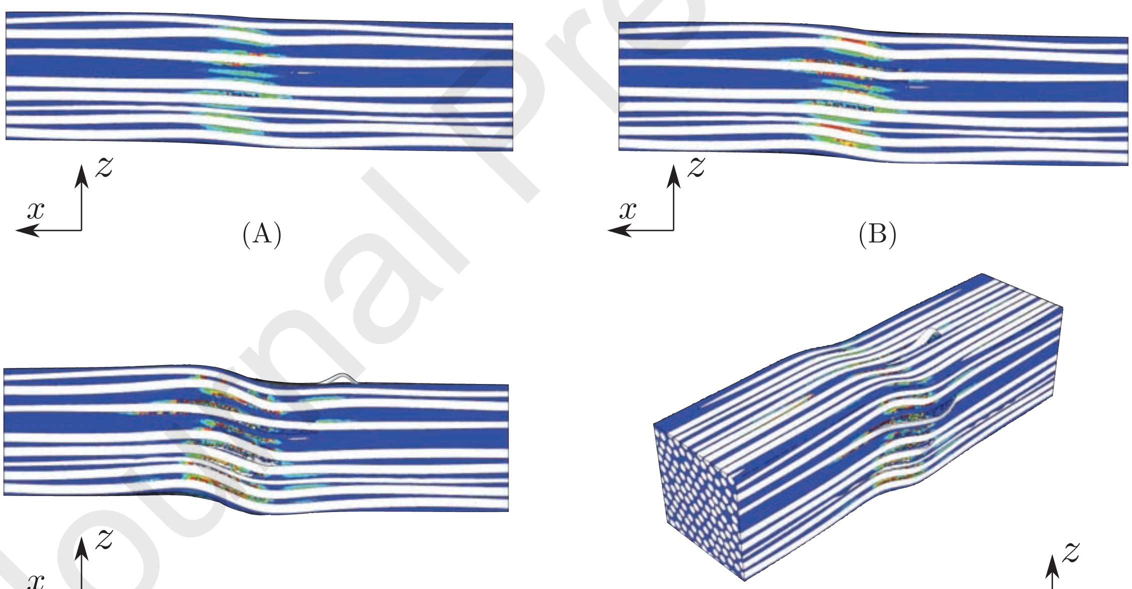

(b) Contour plots of the equivalent plastic strain of the epoxy matrix, at different stages of the damage process (blue - 0.0; yellow - 0.19; red - 0.25).

Figure 11: Numerical results associated with an RVE with $\kappa = 3000$, in longitudinal compression.

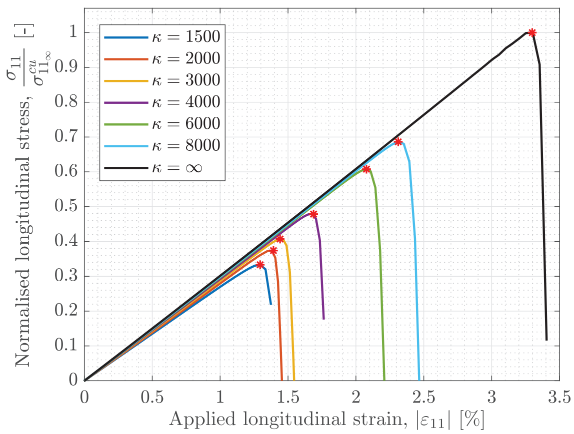

(a) Normalised representative stress-strain curves. The red points indicate the associated normalised peak stress.

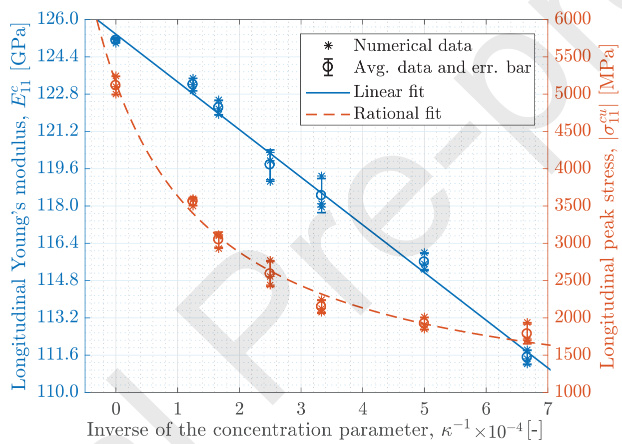

(b) Sensitivity results for the compressive Young's modulus and strength. Both individual numerical results and corresponding mean and standard deviation values are respectively shown, as well as the associated linear ($R^2_{\mathrm{lin}} = 0.994$) and rational ($R^2_{\mathrm{rat}} = 0.991$) fits.

Figure 12: Numerical results showing the effect of the initial fibre misalignment on the longitudinal compressive response.

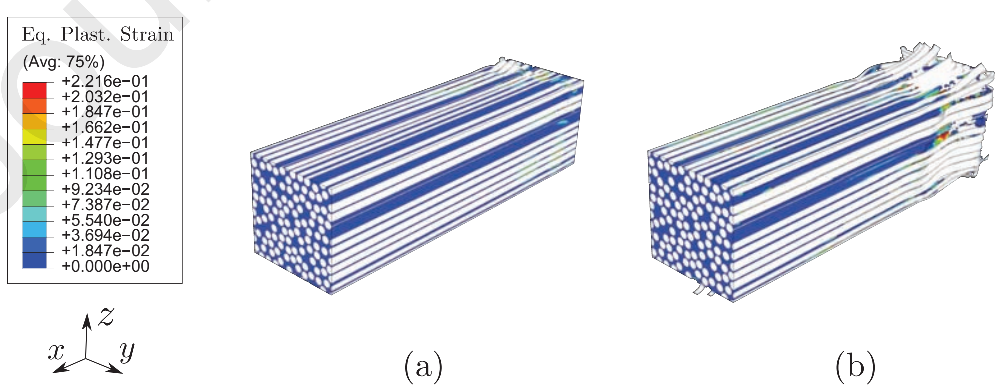

Figure 13: Contour plots of the equivalent plastic strain of an RVE with $\kappa = \infty$, showing the localisation of damage at one of the boundaries of the RVE, when submitted to longitudinal compression, just (a) before and (b) after peak load.

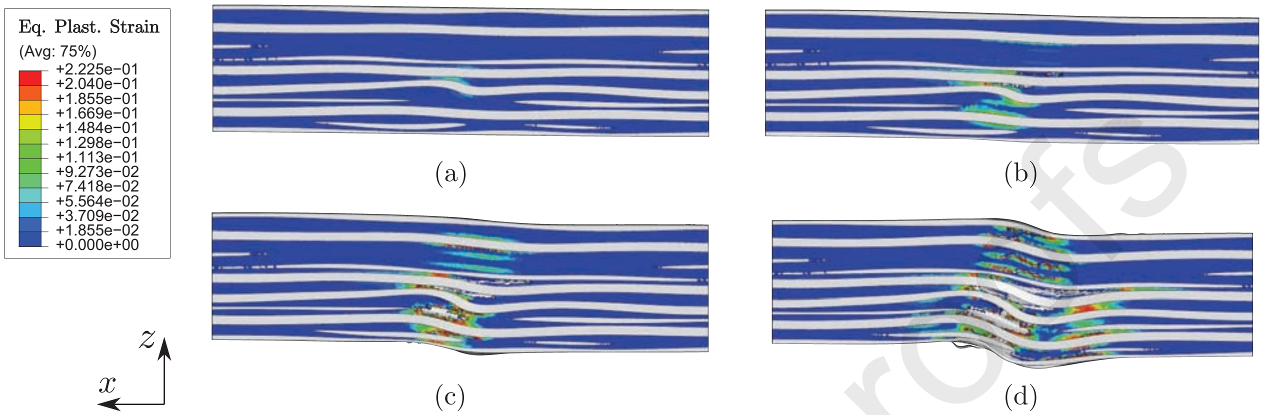

Figure 14: Deformed configuration of an RVE with $\kappa = 1500$, highlighting the contour plots of the equivalent plastic strain at different stages of the damage process in longitudinal compression: (a) non-linearities in the most misaligned region; (b) damage propagation along this region; (c) severe damage propagation along the height of the RVE before peak load; (d) fracture of the material after peak load.

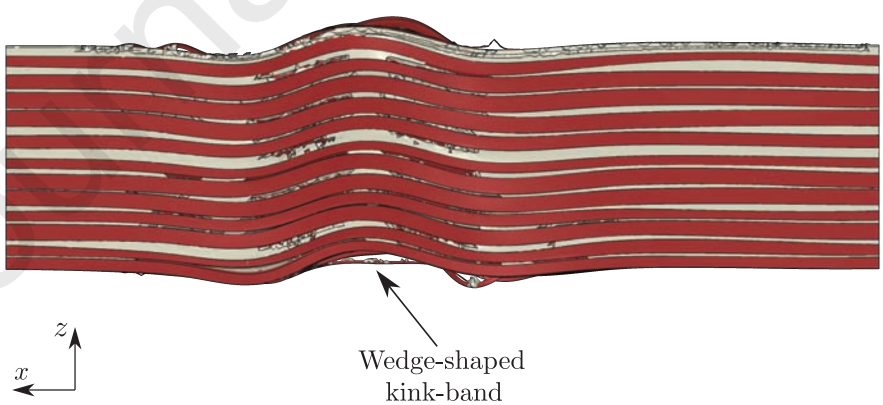

Figure 15: Deformed configuration of an RVE with $\kappa = 8000$, just after peak load, exhibiting a wedge-shaped kink-band.

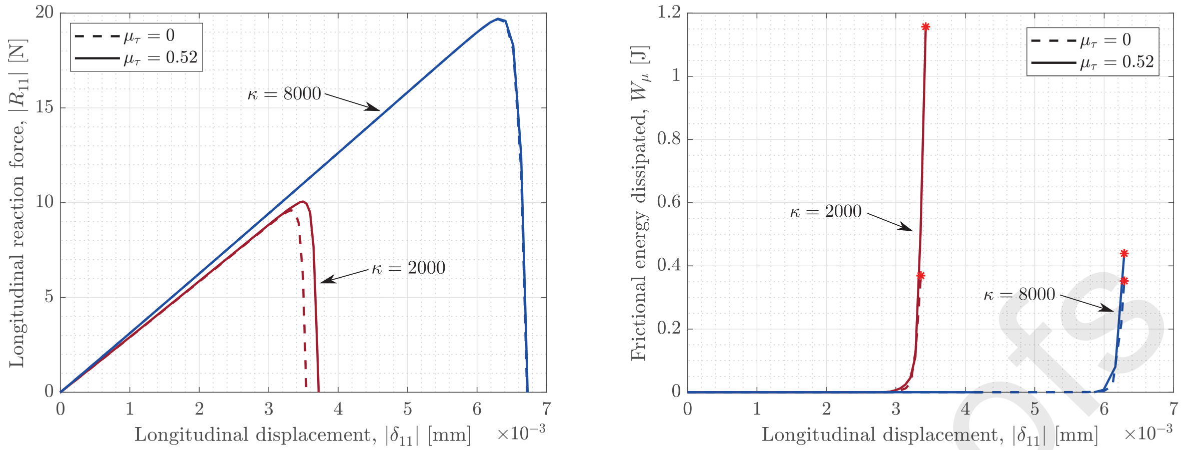

(a) Reaction force vs. displacement.

(b) Frictional energy dissipated vs. displacement.

Figure 16: Numerical assessment of the influence of friction between constituents considering two degrees of misalignment in longitudinal compression. The red points indicate peak load.

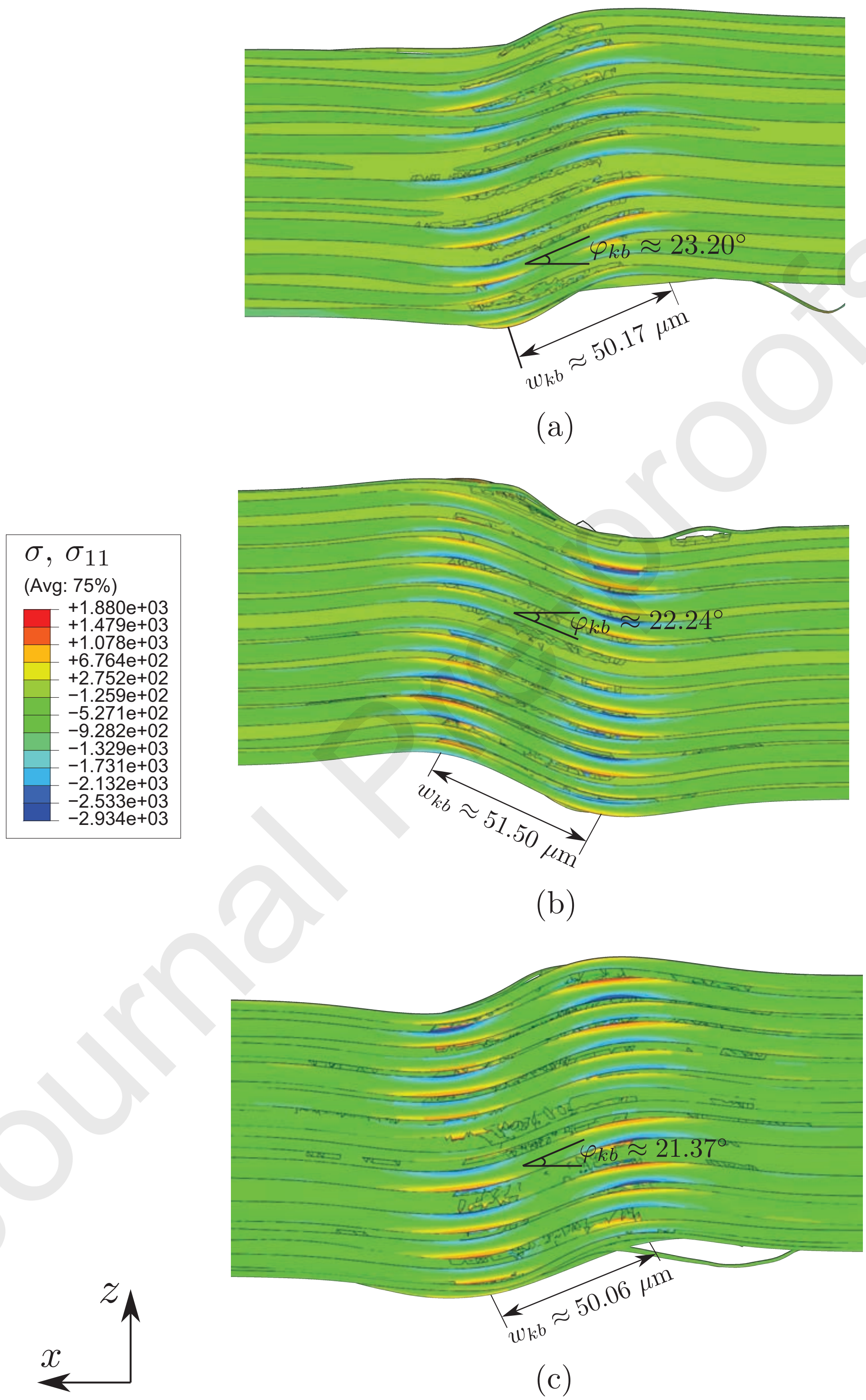

Figure 17: Contour plots of the local longitudinal stress along the kink-band, highlighting the fibre rotation angle of the fibres and kink-band width, associated with RVEs having: (a) $\kappa = 2000$; (b) $\kappa = 4000$; and (c) $\kappa = 6000$ (only the kink-band region is shown).

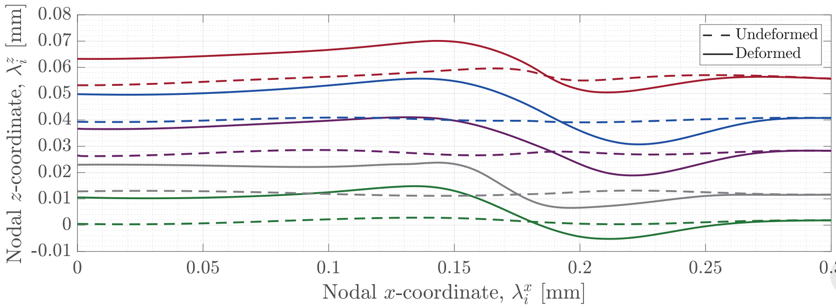

Figure 18: Bi-dimensional (x and z) central spatial coordinates of different fibres, with different degrees of misalignment, of the same RVE ($\kappa = 2000$), having an undeformed (dashed lines) and deformed (solid lines) configurations at peak load.

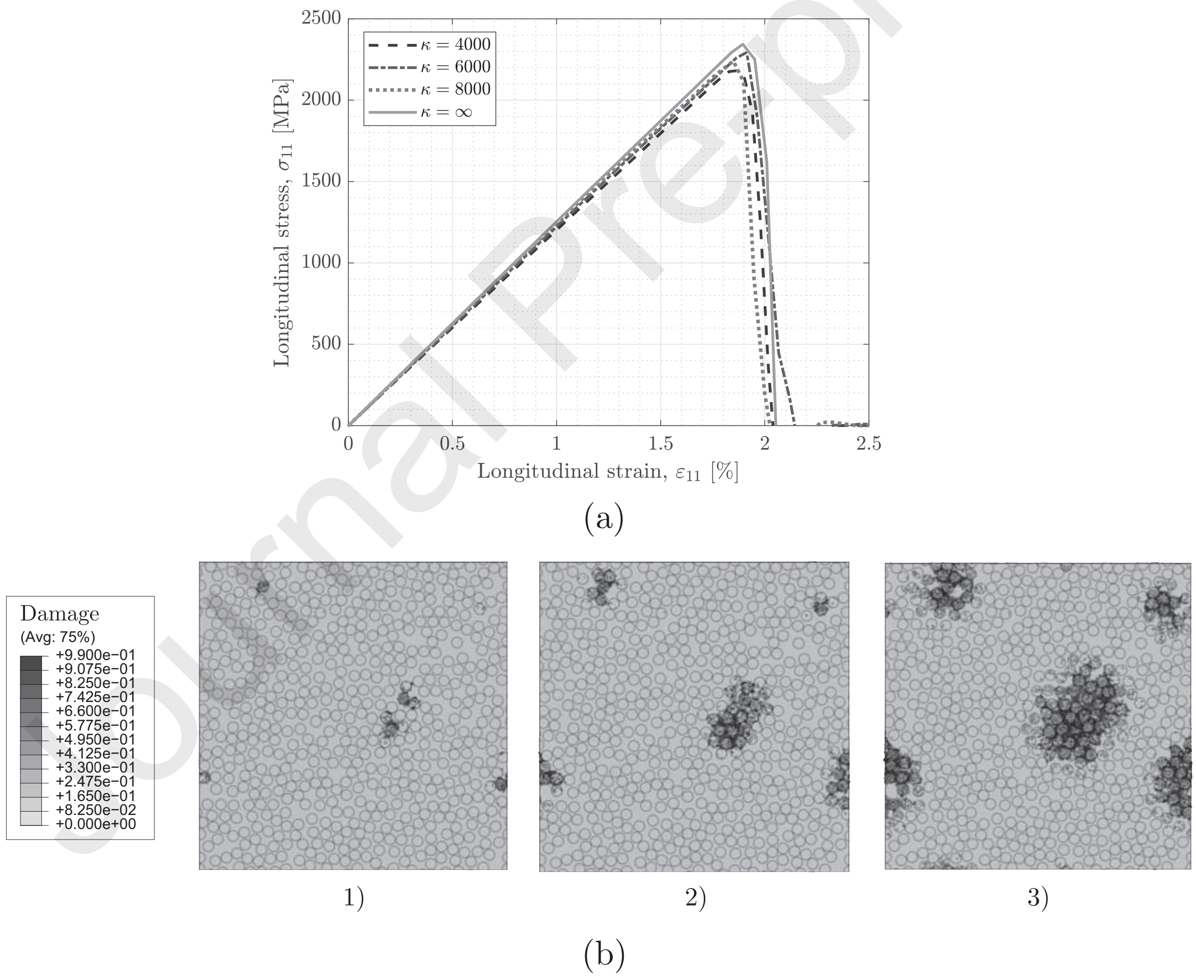

Figure 19: (a) Longitudinal tensile stress-strain curves of four RVEs having different distributions of the initial fibre misalignment, κ; (b) corresponding contour plots of the matrix and fibres damage variable, at different stages of the damage process, for an RVE with $\kappa = 6000$.

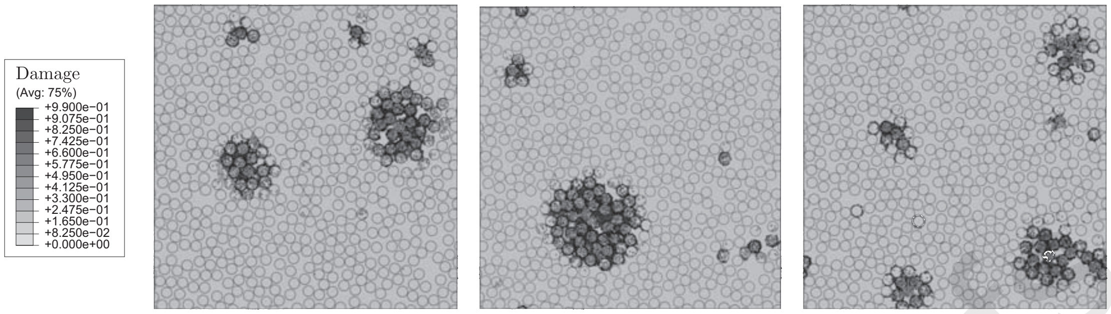

(a) (b) (c)

Figure 20: Contour plots of both matrix and fibres damage variable for an RVE with $\kappa = \infty$, at different longitudinal sections: (a) $\Delta_x/L_x = 0.31$; (b) $\Delta_x/L_x = 0.53$; and (c) $\Delta_x/L_x = 0.78$.

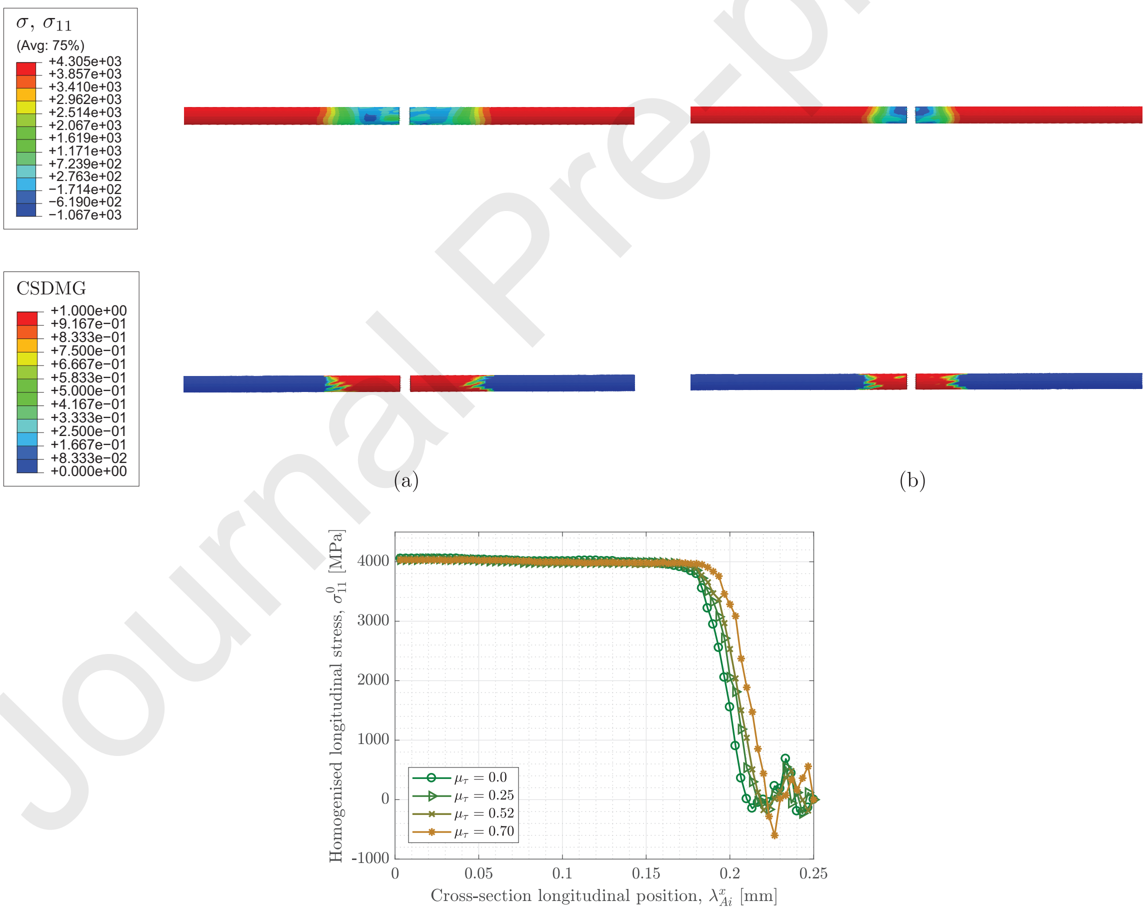

(c)

Figure 21: (a) and (b) Contour plots of the longitudinal stress (σ_{11}) and fibre-matrix interface damage (CSDMG) along a single fibre inside an RVE, considering $\mu_\tau = 0$ and $\mu_\tau = 0.70$, respectively; (c) numerical results of the distribution of the longitudinal stress along a single fibre inside an RVE with $\kappa = \infty$, for different μ_τ (the results associated with only half a fibre are shown).

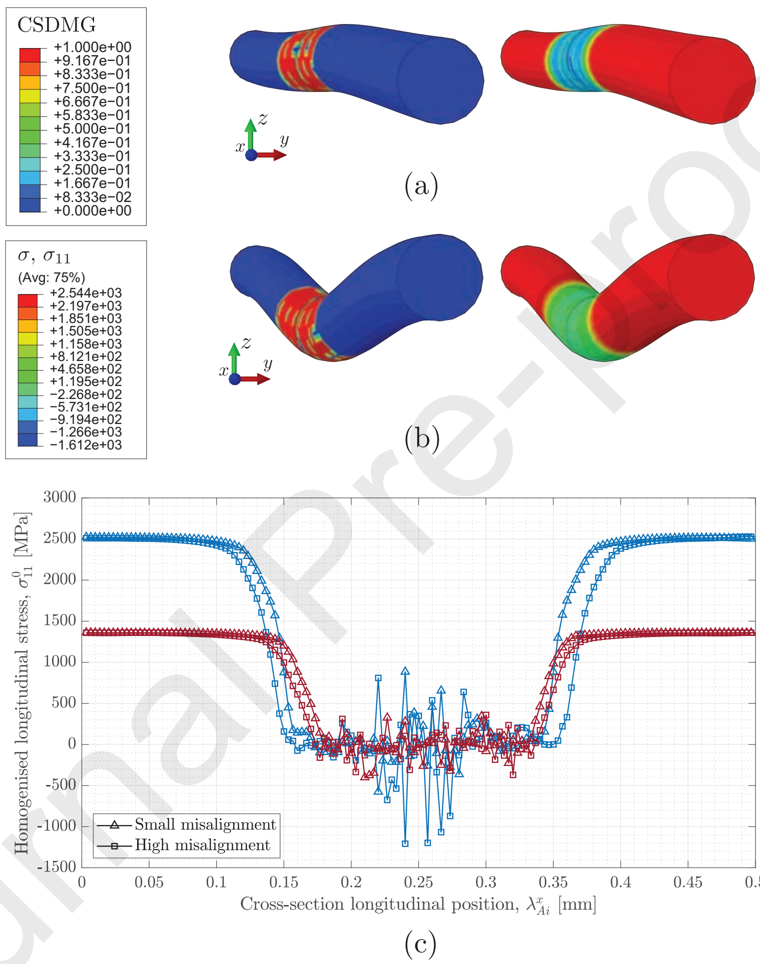

Figure 22: (a) and (b) Contour plots of the fibre-matrix interface damage (left - CSDMG) and longitudinal stress (right - σ_{11} in MPa), exhibiting the debond length, for a fibre having, qualitatively, a “Small” and a “High” degree of misalignment, respectively; (c) numerical predictions of the volumetrically homogenised longitudinal stress along each fibre having different degrees of misalignment (red lines - $\varepsilon_f^0 = 0.6\%$; blue lines - $\varepsilon_f^0 = 1.1\%$).

Table 1: AS4 carbon fibre material properties (Soden et al., 1998, Bai et al., 2015, Herráez et al., 2016, Tavares et al., 2016).

Material property	Value
Fibre diameter	
$2R_f$ [mm]	0.006
Fibre volume fraction	
ω_f [%]	55.9
Young's moduli	
E_{11}^f [MPa]	225000
E_{22}^f [MPa]	15000
Poisson's ratio	
ν_{12}^f [-]	0.2
Shear moduli	
G_{12}^f [MPa]	15000
G_{23}^f [MPa]	7000
Mode I fracture toughness	
$\mathcal{G}_{Ic}^f$ [N/mm]	0.05
Weibull parameters	
σ_0 [MPa]	4275
m_0 [-]	10.7
L_0 [mm]	12.7
Density	
ρ_f [kg/mm^3]	1.78×10^{-6}

Table 2: Matrix material properties (Melro et al., 2013b, Arteiro et al., 2014, 2015).

Material property	Value
Young's modulus	
E_m [MPa]	3760
Poisson's ratio	
ν_m [-]	0.39
Plastic Poisson's ratio	
ν_m^p [-]	0.3
Tensile strength	
X_m^t [MPa]	93
Compressive strength	
X_m^c [MPa]	180
Mode I fracture toughness	
$\mathcal{G}_{Ic}^m$ [N/mm]	0.277
Density	
ρ_m [kg/mm^3]	1.3×10^{-6}

Table 3: Fibre-matrix interface properties (Melro et al., 2013b, Arteiro et al., 2014, 2015).

Material property	Value
Interface stiffness	
K [N/mm^3]	10^8
Interface strengths	
τ_1^0 [MPa]	75
τ_2^0 [MPa]	75
τ_3^0 [MPa]	50
Interface fracture toughnesses	
$\mathcal{G}_{Ic}$ [N/mm]	0.002
$\mathcal{G}_{IIc}$ [N/mm]	0.006
$\mathcal{G}_{IIIc}$ [N/mm]	0.006
Mixed-mode interaction parameter	
η_{BK} [-]	1.45
Friction coefficient	
μ_τ [-]	0.52

Table 4: Size of the RVE vs. normalised numerical predictions of the peak stress.

In-plane dimension, H [μm]	Number of fibres, n_f [#]	Normalised peak stress, $\frac{\sigma_{11}^{cu}}{\sigma_{11}^{max}}$ [%]
$5R_f = 15$	4	77.7
$10R_f = 30$	16	82.5
$15R_f = 45$	36	86.8
$20R_f = 60$	64	90.4
$25R_f = 75$	120	99.2
$30R_f = 90$	168	100.0

Table 5: Quantitative results for different mesh densities.

Element size [μm]	N. of elements [#M]	Normalised peak stress, $\frac{\sigma_{11}^{cu}}{\sigma_{11}^{max}}$ [%]	Computational time, C [h]
$\approx R_f/2$	≈ 1.1	51.2	108.5
$\approx R_f/3$	≈ 3.4	75.5	140.0
$\approx R_f/4$	≈ 6.0	94.4	191.8
$\approx R_f/5$	≈ 7.2	99.4	243.9
$\approx R_f/6$	≈ 9.4	100.0	317.4

Table 6: Numerical predictions of the mean compressive Young's modulus, E_{11}^c, mean peak stresses, σ_{11}^{cu}, and their corresponding standard deviations, for different von Mises concentration parameters, κ.

	$\kappa = 1500$	$\kappa = 2000$	$\kappa = 3000$	$\kappa = 4000$	$\kappa = 6000$	$\kappa = 8000$	$\kappa = \infty$
E_{11}^c [GPa]	$111.5^{\pm 0.3}$	$115.6^{\pm 0.3}$	$118.4^{\pm 0.7}$	$119.8^{\pm 0.6}$	$122.2^{\pm 0.3}$	$123.2^{\pm 0.2}$	$125.1^{\pm 0.1}$
σ_{11}^{cu} [MPa]	$1785^{\pm 133.38}$	$1907^{\pm 120.19}$	$2148^{\pm 86.5}$	$2589^{\pm 167.6}$	$3048^{\pm 103.0}$	$3561^{\pm 53.3}$	$5114^{\pm 122.7}$

Table 7: Mean estimated results associated with the kink-band width, w_{kb}, fibre rotation angle, φ_{kb}, and their corresponding standard deviations, for different von Mises concentration parameters, κ.

	$\kappa = 1500$	$\kappa = 2000$	$\kappa = 3000$	$\kappa = 4000$	$\kappa = 6000$	$\kappa = 8000$
w_{kb} [μm]	$50.17^{\pm 0.88}$	$50.69^{\pm 1.62}$	$49.43^{\pm 1.11}$	$52.77^{\pm 3.47}$	$49.88^{\pm 2.83}$	$51.89^{\pm 3.31}$
φ_{kb} [°]	$23.87^{\pm 0.49}$	$23.44^{\pm 0.57}$	$23.19^{\pm 0.50}$	$22.44^{\pm 0.47}$	$21.91^{\pm 0.31}$	$20.73^{\pm 0.18}$

Declaration of interests

☒ The authors declare that they have no known competing financial interests or personal relationships that could have appeared to influence the work reported in this paper.

☐The authors declare the following financial interests/personal relationships which may be considered as potential competing interests: